5-2011

Thermal Feasibility and Performance Characteristics of an Air-Cooled Axial Flow Cylindrical Power Inverter by Finite Element Analysis

Jonathan Atef Tawfik
University of Tennessee - Knoxville, jtawfik@utk.edu

To the Graduate Council:

I am submitting herewith a thesis written by Jonathan Atef Tawfik entitled "Thermal Feasibility and Performance Characteristics of an Air-Cooled Axial Flow Cylindrical Power Inverter by Finite Element Analysis." I have examined the final electronic copy of this thesis for form and content and recommend that it be accepted in partial fulfillment of the requirements for the degree of Master of Science, with a major in Mechanical Engineering.

Rao V. Arimilli, Major Professor

We have read this thesis and recommend its acceptance:

Jay Frankel, Majid Keyhani, Rao V. Arimilli

Accepted for the Council:
Dixie L. Thompson

Vice Provost and Dean of the Graduate School

(Original signatures are on file with official student records.)

To the Graduate Council:

I am submitting herewith a thesis written by Jonathan Atef Tawfik entitled "Thermal Feasibility and Performance of an Air-Cooled Axial Flow Cylindrical Power Inverter by Finite Element Analysis." I have examined the final electronic copy of this thesis for form and content and recommend that it be accepted in partial fulfillment of the requirements for the degree of Master of Science, with a major in Mechanical Engineering.

                                                    Rao V. Arimilli, Major Professor

We have read this thesis
and recommend its acceptance:

Majid Keyhani

Jay Frankel

Rao Arimilli

                                                Accepted for the Council:

                                                Carolyn R. Hodges
                                                Vice Provost and Dean of the Graduate School

(Original signatures are on file with official student records.)

Thermal Feasibility and Performance Characteristics of an
Air-Cooled Axial Flow Cylindrical Power Inverter by Finite
Element Analysis

A Thesis Presented for the

Master of Science Degree

The University of Tennessee, Knoxville

Jonathan Atef Tawfik

May 2011

Dedication

To my parents, Atef & Soheir Tawfik,

for their continual love, support, and wisdom in my life.

They have taught me to work at everything

with all my heart as unto the LORD,

and not for human masters.

Colossians 3:23

Acknowledgements

Abstract

The purpose of the present study is to determine the thermal feasibility of an air-cooled power inverter. The inverter circuitry layout is designed in tandem with the thermal management of the devices. The cylindrical configuration of the air-cooled inverter concept accommodates a collinear axial air blower and a cylindrical capacitor with inverter cards oriented radially between them. Cooling air flows from the axial fan around the inverter cards and through the center hole of the cylindrical capacitor. The present study is a continuation of the thermal feasibility study conducted in fiscal year 2009 for the Oak Ridge National Laboratory to design a power inverter with a radial inflow cylindrical configuration. Results in the present study are obtained by modeling the inverter concept in computer simulations using the finite element method. Air flow rate, ambient air temperature, voltage, and device switching frequency are studied parametrically. Inlet air temperature was 50°C for all the results reported. Transient and steady-state simulations are based on inverter current that represents the US06 supplemental federal test procedure from the US EPA. The source of heat to the system comes from the power dissipated in the form of heat from the switches and diodes and is modeled as a function of the voltage, switching frequency, current, and device temperature. Since the device temperature is a result as well as an input variable, the steady-state and transient solution are iterative on this parameter. The results demonstrate the thermal feasibility of using air to cool an axial-flow power inverter. This axial inflow configuration decreases the pressure drop through the system by 63% over the radial inflow configuration, and the ideal blower power input for an inlet air flow rate of 540 cfm is reduced from 936 W to 312 W for the whole inverter. When the model is subject to one or multiple current cycles, the maximum device temperature does not exceed 164°F (327°F) for an inlet flow rate of 270 cfm, ambient temperature of 120°C, voltage of 650 V, and switching frequency of 20 kHz. Although the maximum temperature in one cycle is most sensitive to ambient temperature, the ambient temperature affect decays after approximately half the duration of one cycle. Of the parametric variables considered in the transient simulations, the system is most sensitive to inlet air flow rate.

Table of Contents

List of Figures

List of Tables

Nomenclature

$\frac{D}{Dt}$	Total derivative with respect to time
$\frac{\partial}{\partial x_i}$	Partial derivative with respect to x_i
$\frac{\partial}{\partial x_i}$	Partial derivative with respect to x_i
2D	Two-dimensional
3D	Three-dimensional
abs.	Absolute value, $|x|$
AC	Alternating current, A
A_c	Cross-sectional flow area, m^2
A_{ch}	Channel cross-sectional area. mm^2
a_i	MOSFET conduction losses polynomial coefficient, $\Omega/°C$ and Ω
A_{in}	Inlet area, m^2
AlN	Aluminum nitride
A_{out}	Outlet cross-sectional area, mm^2
AR	Outlet to inlet area ratio, %
b_i	MOSFET switching losses polynomial coefficient, J/°C
c_i	Diode conduction losses polynomial coefficient, $\Omega/°C^2$, $\Omega/°C$, and Ω
c_p	Specific heat capacity, J/K
CTE	Coefficient of thermal expansion
$C_{\epsilon i}$	Dimensionless closure coefficients for the standard k-ϵ model
DBA	Direct-bonded aluminum
DBC	Direct-bonded copper

DC	Direct current, A
D_h	Hydraulic diameter, $\frac{4A_c}{\wp}$, m
Di	Diode i
d_i	Diode conduction losses polynomial coefficient, V/°C and V
E	Energy loss, J
e	Energy balance error, %
ECU	Engine control unit
e_i	Diode switching losses polynomial coefficient, J/°C
EPA	Environmental Protection Agency
f	Force, N; dimensionless friction factor
FEM	Finite element method
f_{sw}	Switching frequency, kHz
FTP	Vehicle emissions federal test procedure
FY	Fiscal year
$\mathbf{g,}\, g$	Gravity, m/s^2
h	Heat transfer coefficient, W/(m^{2}K)
h_f	Height related to friction factor, m
HEV	Hybrid electric vehicle
HTRB	High temperature reverse bias
I	Current, A
ICE	Internal combustion engine
I_{diode}	Current to each diode, A
IGBT	insulated-gate bipolar transistor

I_{MOS}	Current to each MOSFET, A
I_{scale}	Dimensionless current scaling factor
I_T	Turbulence intensity, %
$I_{US06}(t)$	US06 electric current to power inverter, A
JBS	Junction barrier Shottky
JFET	Junction gate field-effect transistors
k	Turbulent kinetic energy, J; thermal conductivity, W/(m·K)
k_T	Turbulent thermal conductivity, W/(m·K)
l_T	Turbulent length scale, m
MEMS	Microelectromechanical systems
Mi	MOSFET power switch i
MOSFET	Metal oxide semiconductor field-effect transistor
n	Normal direction vector
N	Number of inverter cards
N_{fins}	Number of fins
ORNL	Oak Ridge National Laboratory
OTAQ	The United States Office of Transportation and Air Quality
p	Pressure, Pa (in. H_2O)
$\wp$	Wetted perimeter, m
PCU	Process control unit
Pr	Prandtl number
Pr_T	Turbulent Prandtl number
Q	Air flow rate per unit cell, m^3/s (cfm)
$\dot{q}$	Heat generation, W

q''	Heat flux per unit area, W/m^2
$\dot{q}_{cond}$	Conduction losses, W
q_i	Energy at surface i, W
q_{in}	Energy at inlet boundary, W
q_{out}	Energy at outlet boundary, W
$\dot{q}_{sw}$	Switching losses, W
R	Resistance, Ω
Re_{Dh}	Reynolds number based on hydraulic diameter
Re_x	Flow direction Reynolds number
SFTP	Supplemental federal test procedure
Si	Silicon
SiC	Silicon carbide
S_{ij}	Mean strain rate tensor
SiN	Silicon nitride
t	Time, seconds
T	Temperature, °C (°F)
T_{amb}	Ambient temperature, °C (°F)
T_{in}	Inlet temperature, °C (°F)
T_j	Junction temperature, °C (°F)
U	Mean velocity, m/s (mph)
$\mathbf{u}$	Flow velocity vector
U^+	Dimensionless mean velocity
u_i	Velocity in coordinate direction i
U_{in}	Inlet mean velocity, m/s

U_{mid}	Mid-section velocity, m/s
US06	EPA Supplemental federal test procedure for light-duty trucks and light-duty vehicles
u_τ	Friction velocity, m/s
V	Voltage, V
V_{scale}	Dimensionless voltage scaling factor
W	Card width, m
x	Flow coordinate direction
x_1	Fin height perpendicular to the card, m
y	Coordinate direction perpendicular to a wall boundary
y^+	Dimensionless, sublayer-scaled, distance, $u_\tau y / \nu$

Greek symbols

δ	Velocity boundary layer thickness
∇	Divergence
∇^2	Laplacian operator
Δ	Change
δ_{ij}	Kronecker delta
δ_T	Thermal boundary layer thickness
ϵ	Specific dissipation
κ	Von Kármán constant
μ	Dynamic viscosity
μ_T	Turbulent dynamic viscosity
ν	Kinematic viscosity
ν_T	Turbulent kinematic viscosity

ρ	Density
τ_w	Shear stress on the wall
τ_{ij}	Specific Reynolds stress tensor, $-\overline{u_i' u_j'}$
Φ	Dissipation
Ω	Ohms
ω	Specific dissipation rate

Units

°C	Degrees Celsius
°F	Degrees Fahrenheit
A	Amperes
cfm	Cubic feet per minute
hp	Horsepower
in.	Inches
in. H_2O	Height of a water column
J	Joules
K	Kelvin
kHz	Kilohertz
L	Liters
mm	Millimeters
mph	Miles per hour
W	Watts
Ω	Ohms

Chapter 1. Introduction

1.1 Background & Motivation

Research in the transportation industry has recently been motivated by improving fuel economy of personal transportation vehicles. Automakers have been faced with demanding CO_2 emissions constraints and other environmental considerations in recent years prompting the research and development efforts of hybrid gas-electric vehicles (HEVs).   Following the introduction of HEVs to the market, ongoing research is focused on improved reliability and performance, specifically in terms of power consumption and efficiency. Since HEVs operate much differently than traditional vehicles with internal combustion engines (ICEs), improving reliability and performance is an ongoing important area of research.

One of the fundamental differences between HEVs and traditional vehicles apart from the increased complexity of the power flow is simply the amount of onboard electronic components. As a result, HEVs will typically weigh more than a traditional vehicle which will in turn increase the power train requirements although one of the important purposes of replacing traditional vehicles with HEVs is decreased power consumption. For example, Toyota specifies the curb weight of the traditional and hybrid 2011 Camry as 3,307 lbs and 3,680 lbs for two comparable models, respectively [1], [2]. The hybrid version of the Camry weighs approximately 11% more in this case.

Of the major electronic components added to a HEV that contributes to this increased weight are the batteries, power inverter, and electric motor, and each component will require auxiliary support systems for reliable operation and safety. The power stored in the batteries is used to drive the vehicle when a direct current (DC) signal from the batteries is converted to an alternating current (AC) signal supplied to the motor via the power inverter. The typical current output of power invert-

ers in HEVs is three-phase AC. Figure 1.1 shows the electrical schematic of a three-phase power inverter. The three-phase power inverter consists of a DC power supply, capacitor, and three "legs" in which each half-leg consists of a diode and a relay switch.

The power inverter accomplishes the conversion from DC to AC via a modulated sequence of opening and closing of the switches by an external source. The alternation of current flow between phase legs is instantaneous in an ideal power inverter. When the inverter efficiency is less than 100%, the power lost through switching operations is dissipated as heat which must then be removed from the inverter components by an external auxiliary system in order to maintain reliable performance. This heat generated is internally stored and the components of the inverter will exceed the maximum operating temperature in the event that a sufficient cooling system is not present.

The power inverter in a current HEV is typically kept below the maximum operating temperature by utilizing a dedicated cooling system that circulates radiator fluid to remove the heat from the devices. This circulating fluid is a source of weight that increases the demands of the power train to drive the vehicle. The weight of the cooling system is a function of the bulk amount of fluid stored onboard the vehicle which is related to the properties and the efficient use of the coolant. Reducing the amount of fluid stored onboard a HEV can be accomplished by changing the manner in which this fluid is utilized to cool the switches and diodes and by changing the coolant fluid itself.
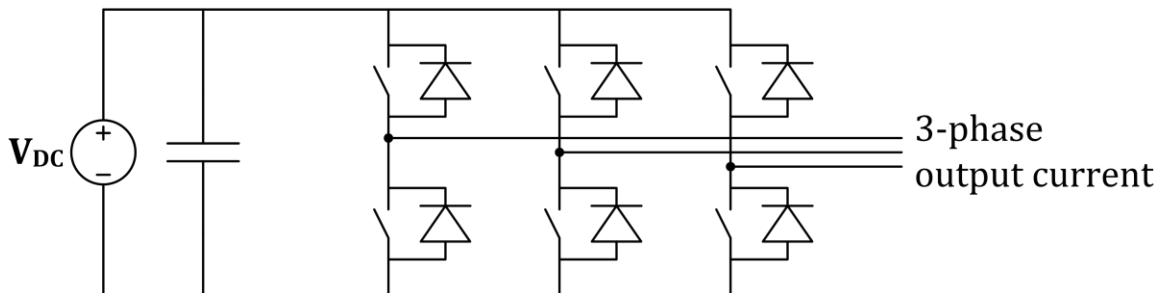
Figure 1.1. Three-Phase Power Inverter Electrical Schematic

2

1.2 Objective

The purpose of this study is to determine the thermal feasibility of using air to cool an axial flow cylindrical electronic power inverter. Thermal feasibility is to be demonstrated with respect to electrical and mechanical constraints and input parameters chosen to represent competitive conditions encountered in the automotive industry. The problem is approached using numerical computations conducted using the finite element method. A design process will involve both electrical and thermal feasibility in an integrated approach. That is, thermal feasibility is not determined independent of electrical circuitry layout and considerations.

The capacitor in Figure 1.1 is also a source of dissipative heat and will be the largest object in the inverter. As a result, design considerations and overall configuration decisions begin in light of the shape of the capacitor. In previous years, inverters with cylindrical capacitor designs have been investigated utilizing the capacitor's radial symmetry in the feasibility studies. A *radial inflow* inverter was designed by Lowe et al. [3] in the Oak Ridge National Laboratory (ORNL) Fiscal Year (FY) 2009 and the present *axial inflow* concept is a continuation of this work through FY 2010. The objective of this study is to design a new axial inflow configuration incorporating the lessons learned from the previous study and add more features to it as outlined in this section. The thermal plot of the final radial inflow design concept is given in Figure 1.2 followed by a descriptive schematic of the differences between the previous and present investigations in Figure 1.3. Figure 1.2 is duplicated 9 times about the centerline to represent the entire radial inflow inverter. In Figure 1.3, inverter cards are placed in the open space above the circular capacitor.

In the present work, we begin by reconfiguring the air flow field around the inverter electronics that are to be placed in the open space above the cylindrical capacitor in Figure 1.3, which is a cross-sectional view of the inverter. Initial studies will compare the radial inflow configuration with the axial inflow configuration now being considered.
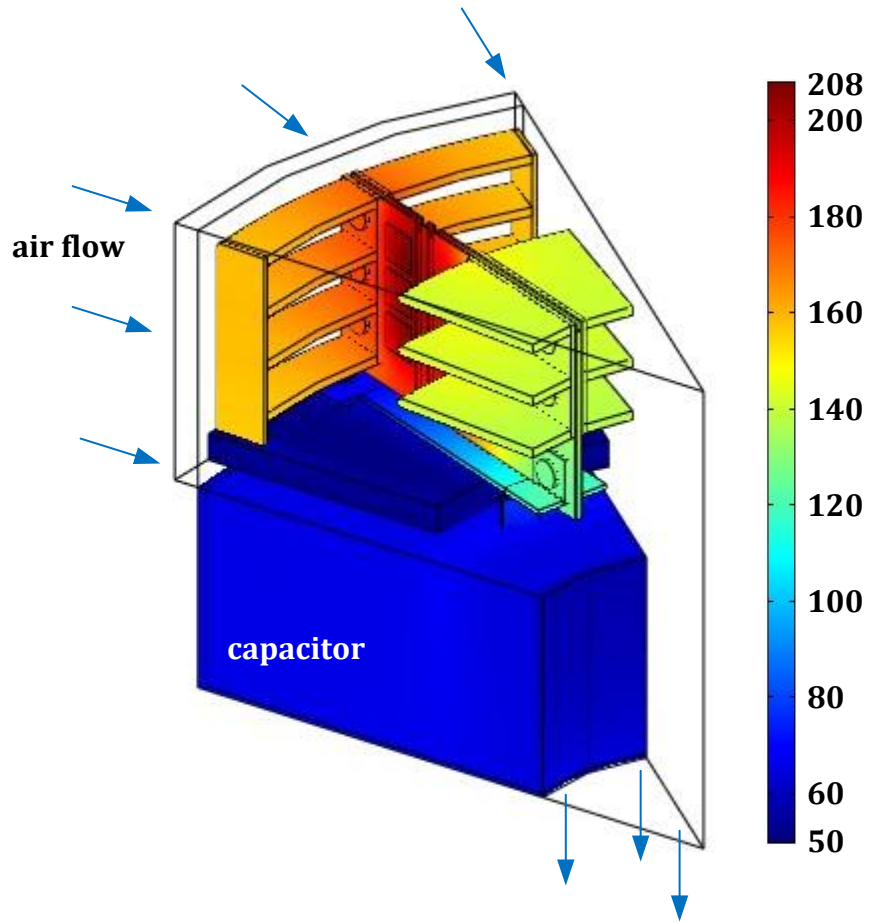
Figure 1.2 One of one of nine identical sections of the radial inflow inverter concept temperature plot (°C) [3]
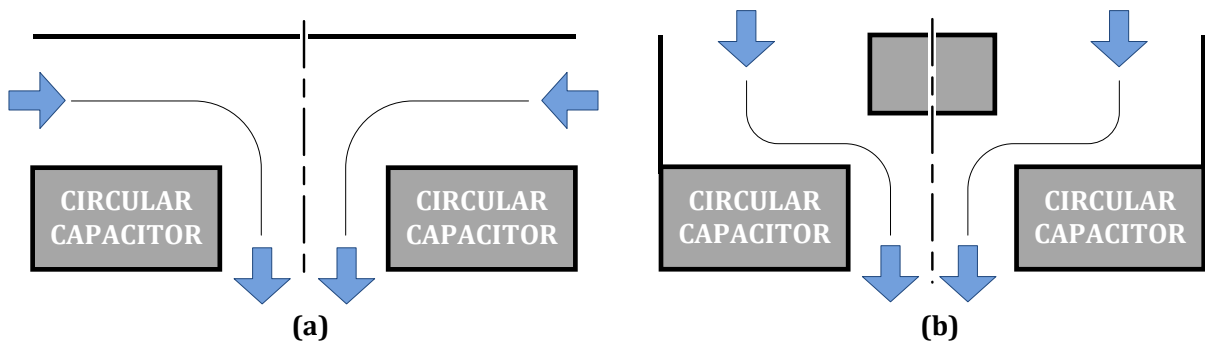
Figure 1.3 (a) Radial inflow inverter design of FY 2009 and (b) Axial inflow inverter Design of FY 2010

4

Keeping in mind the main objective is to design the inverter such as can be cooled by air, ideal blower power input requirements must be kept as a key consideration in the design process. Both the radial and axial inflow concepts are sufficient configurations for air to cool the inverter electronics as well as the capacitor at the cost of a high pressure drop through the device. That the design process started with that of Figure 1.3 (a) and continues to that of Figure 1.3 (b) is expected since the first apparent advantage of the radial inflow inverter is that air flow *appears* to bend less than the axial inflow inverter. However, the flow scenario is hard to implement when revolved 360°. An axial flow air mover can easily be placed above the axial inflow inverter, and the flow pattern is in fact less drastic. A large pressure drop across the device is required to accomplish the cooling in the radial inflow inverter configuration because the outlet to inlet area ratio of the concept is approximately 10%. Additionally, the area ratio can be reduced in the axial inflow configuration by placing a center hub at the inlet as shown in the Figure 1.3 (b).

In summary, the specific objectives of this study are:

(1) To continue the work of FY 2009 and demonstrate the benefit of introducing air flow axially instead of radially to reduce the blower power requirements.

(2) To determine the thermal feasibility of cooling an electronic power inverter with air that will meet the demands of the automotive industry.

(3) To understand how the design behaves in different scenarios by varying the electrical and air flow parameters in both steady-state and transient simulations.

Chapter 2.   Literature Review

Power electronics have been studied for the automotive industry with many objectives in mind including cost, weight reduction, volume reduction, and thermal fatigue life. Though these challenges have traditionally been addressed from an electrical, mechanical, or materials selection point of view, many authors have been taking an integrated approach in recent years. The literature presented herein discusses the past and present research concerning advancements in power electronics technology. A path forward consistent with the objective of the present study is chosen in light of the work presented herein.

2.1 Electronics Packaging

The need to integrate the designs of the components in HEVs has led some researchers to investigate the possibility of merging the power electronics coolant loop with the engine coolant loop. This change would cause the power electronics to be in a 105°C cooling environment instead of a 70°C cooling environment [4], [5] and thus many more considerations must be brought into the scope of power electronics design than the traditional approach because of the new high-temperature challenges. Among the reliability issues to be faced in light of high temperature applications are substrate material, conductor stability, die bonding material, wire bonds, bond metallurgy reliability, and encapsulation materials [4]. A number of technologies have been introduced to address how power electronics behave in high temperature environments, especially when there is a mismatch in the coefficient of thermal expansion (CTE) of interacting materials. Some of the developed technologies to address reliability are silicon nitride materials (SiN), flip-chip assembly methods, and the elimination of base plates. Although eliminating the base plate will improve the thermal cycling characteristics, the thermal capacitance is reduced and thus the devices will have inferior thermal impedance [6].

6

More generally, removing layers in a thermal stack can open up options in package design and material choice and can be accomplished also by reducing the thermal resistance of each layer [7].

Kubota et al. [8] summarized the weight and volume reduction techniques for power electronics outfitted for Honda® HEVs by comparing the latest model with previous models. Integrating the design of the engine control unit (ECU), DC-DC converter, and inverter eliminated the need for separate metal cases and cooling systems and reduced the combined weight and volume of the units by 31% and 10%, respectively. More compact designs of this nature can exhibit very little conducted and radiated heat losses [6]. This change had also increased the cooling efficiency because the cooling air flow velocity was increased and the cooling air flow path takes several more turns than in previous Honda® models. Increasing the overvoltage-detection speed and decreasing the time between overvoltage detection and current interruption reduced the capacitance of the inverter capacitor by 50%.

Similarly, Nozawa et al. [9] summarized the weight and volume reduction techniques for power electronics outfitted for Toyota® vehicles, also comparing previous with current models. He additionally described how these techniques also improved mass production assembly of the vehicles. Size and weight was reduced by increasing the efficiency and output of the devices as well as greatly improving the cooling efficiency. A newly-developed process control unit (PCU) contributes to increasing the maximum system voltage from 500V to 650V, while yet decreasing the size of the motor. The PCU utilizes a direct cooling structure with an increased cooling efficiency, decreasing the weight and volume of the unit by 36% and 37%, respectively. Similar to Kubota et al. [8], size and weight reduction was achieved by reducing the number of parts and integrating the function of similar parts. The total amount of components, bolts, and spreading grease has been reduced by 23%, 34%, and 66%, respectively. The capacitor module uses thinner film and a new motor control scheme, effectively reducing the capacitance by 30%, weight by 40%, and the volume by 33%. Other changes

were also made to the inverter wiring, reactor core, and insulated-gate bipolar transistor (IGBT) devices.

Size and weight reduction in HEVs has also been addressed in the design of the transmission. Mizuno et al. [10] described these changes for Toyota® vehicles. Following the work presented by Nozawa et al. [9], they showed that the boost converter output voltage from 500V to 650V required a change to be made in the motor insulation and the coil winding for distribution voltage. The coil end length was shortened by 20% through active compression molding to reduce the motor size. Further weight reductions of 20% were achieved by redesigning the motor speed reduction device, a compound gear, and a compact high-output motor [10].

The experiments performed by Chinthavali et al. [5] are motivated by the fact that silicon-based technology would need to be replaced by technology utilizing silicon carbide (SiC) materials for power electronics in order to meet this new high-temperature demand, and this result is also noted by Scofield et al. [11]. In fact, the research objective of the present study stems from Chinthavali's recognition of the specific need to replace liquid-cooled systems with air-cooled ones and integrate inverter circuitry with the high-temperature packaging.

> *"Another option is to replace the liquid cooled systems ... with air-cooled systems because this will reduce the complexity of system integration and reduce the cost by eliminating the additional cooling loop in the existing hybrid vehicles....High-temperature packaging was recognized as a necessary area to be developed in parallel with development of SiC technology, so that the benefits of the SiC devices can be more fully realized in many applications.* [Wide band gap] *research at Oak Ridge National Laboratory is focused on high temperature packaging (>200°C), high temperature gate drive electronics that can work at 200°C [12], inverter design and prototype development, efficiency estimation with device simulation, and experimental characterization"* [5]

8

Experiments were conducted on SiC junction gate field-effect transistors (JFET) which are attractive for high power applications because the technology has been developed for SiC [13]. Bondarenko et al. [13] characterized these devices to be operable from 25°C to +400°C. This is an important result considering the challenges of replacing liquid coolant with air in the cooling system. Their results concluded that hundreds of amperes are entirely feasible in power electronics using JFET technology [13].

In addition, Chinthavali et al. [14] also performed static and dynamic experiments on several other SiC devices to demonstrate their benefit over Si technology since previous authors demonstrated better system efficiency [15] and projected "significant reduction in weight and size of SiC power converters with an increase in the efficiency" [16], [17]. The unique aspect of the experiments is that a commercial gate driver chip was used. SiC Shottky diodes have lower switching losses than pn diodes which favor these devices for high frequency applications. The conduction losses increase with increasing temperature but the switching losses are nearly constant with increasing temperature. This is an advantage considering the temperature-dependent characteristics of Si diodes. In summary, SiC unipolar devices demonstrated operability in high temperature and high frequency applications, and Chinthavali et al. [14] concluded his work by recommending that packaging techniques utilize these high temperature properties.

Bondarenko et al. [13] also conclusively demonstrated aluminum nitride (AlN) to be the best substrate material because of the materials high thermal conductivity and excellent CTE match to SiC. However, Hornung and Scheuermann [18] concluded that the low peel strength of AlN makes the material less desirable for high temperature applications. Katsis and Zheng [19] followed this conclusion in their investigations for aeronautical applications. They suggested the use of spring pin interconnects that are applied under preloaded pressure in place of soldered connections to absorb the CTE mismatch when using materials such as alumina that do not have a comparable CTE match to SiC yet may have a higher peel strength.

Scofield et al. [11] addressed the aforementioned reliability issues by subjecting a SiC metal oxide semiconductor field-effect transistor junction barrier Shottky (MOSFET-JBS) diode power module to high temperature reverse bias (HTRB), power cycling, and ambient temperature cycling from -55°C to 200°C. One objective of the study was to determine the appropriate materials of construction of the power module. The base plate was completely removed in second generation module designs in order to address reliability of the electronics as was noted above and mentioned by Elshabini and Barlow [4]. CTE mismatch was found to be a major contributor to substrate cracking and direct bond copper (DBC) delamination in the thermal cycling experiments. Lower DBC delamination is achieved at the cost of more stress in the substrate as the thickness of the DBC material increases. Copper cooling fins are soldered directly to the DBC on the underside of the substrate in order to address thermal cycling challenges, and finite element analysis is performed in a parametric study to study the dimensions of the fins when the system is cooled by air. The results are representative of 100 W and 50 W heat generation per MOSFET and diode, respectively. Furthermore, peak MOSFET junction temperature is presented as a function of air flow rate, and a maximum MOSFET junction temperature of 300°C is reported for the worst case air flow velocity of 1000 ft/min.

Scofield et al. [11], [20] also investigated the difference between using SiC MOSFET and Si IGBT. At a junction temperature of 125°C, diode current of 100 A, and a switching frequency of 20 kHz, the SiC MOSFETs exhibited a significant efficiency advantage of 38-43% over the Si IGBT components. He reported a voltage drop and resistance through the devices as a function of temperature, which is consistent with the results obtained by Chinthavali et al. [5]. Selection of SiC MOSFET over Si IGBT technology "yielded a 14% weight reduction, superior CTE match for cycle-life reliability, and minimal thermal performance penalty" [20]. The combined conduction and switching losses are improved for junction temperatures of 25°C and 150°C by 30% and 54%, respectively.

10

The scope of power electronics research also extends towards broader industrial applications and microelectromechanical systems (MEMS). The interest of the military is for high-efficiency cooling MEMS with stringent fluid and thermal performance. High convective rates can be achieved when liquid coolant flows through micro-fabricated structures [21], [22]. Manifold microchannel cooling designs act as thermal fin structures but also distribute the fluid uniformly in a thermal stack. Large manifold channels transport fluid to and from the active cooling area, and fluid is forced through much smaller microchannels in parallel. The benefits of this design include uniform distribution of fluid reducing temperature non-uniformity, high fluid restriction only in channels where there is maximum thermal benefit, and a disturbed laminar flow profile at the heat source [7]. Among the disadvantages is the complexity of the fabrication process involved [23], [24].

2.2 Summary

Power electronics research is motivated by a reduction in cost, weight, and volume. Researchers have addressed these engineering constraints by a variety of methods, one of which involves the cooling mechanism of the systems. In order to reduce the weight of the coolant loop, more efficient cooling and design for high temperatures is imperative. SiC Shottky diodes and SiC metal oxide semiconductor field-effect transistors (MOSFET) have demonstrated high-temperature operability which allows for further research in reducing the weight of the coolant loop. The development of new technologies for the automotive industry may be applied to other industrial uses such as in the aerospace industry or for military applications.

The objective of lowering cost, weight, and volume was met by taking advantage of the high temperature properties demonstrated in SiC devices and by replacing a liquid coolant loop with one that utilizes ambient air. As was recognized by Chinthavali et al. [5], these challenges of the automotive industry can be addressed by replacing liquid-cooled systems with air-cooled ones when the thermal packaging is designed in tandem with the inverter circuitry layout in an integrated approach.

11

Chapter 3.   Problem Statement

The formal problem description can be described using Figure 3.1, representing a power inverter that is designed to accommodate an axial flow air mover and a capacitor that is in the shape of a circular ring of rectangular cross section. Mounting, electrical, heat removal, and flow guidance conceptual hardware are not shown in the figure for the sake of simplicity. However, electrical and mechanical feasibility are an integral part of the design goals.

The capacitor in the 2D figure is revolved around 360° about the centerline on the right side of the figure as shown, and the inverter card is repeated 9 times to define the basic shape of the power inverter. In other words, 9 inverter cards are arranged radially above a cylindrical capacitor (for a better view of the overall arrangement see Figure 4.2 on page 39). Air flows through the top at a temperature, T_{in}, and around the inverter card before turning and exiting at the bottom through the capacitor. A central inner hub is placed co-linear to the power inverter at the inlet in order to reduce the area ratio, $AR \equiv A_{out}/A_{in}$. Reducing this area ratio at the onset will yield lower pressure drop, ΔP, for a given fluid density, ρ, and inlet flow velocity, U_{in}, according to Bernoulli's principle which states

$$\Delta P = \frac{1}{2}\rho U_{in}^2 \left[1 - \left(\frac{1}{AR}\right)^2 \right] \qquad (3.1)$$

Heat is generated from the power switches and diodes, denoted $M_1 \ldots M_6$ and $D_1 \ldots D_6$, respectively, and in the capacitor. The heat is removed from the system via the cooling air flowing through the device from top to bottom at an inlet temperature, T_{in}. Two sets of switches and diodes are arranged in horizontal rows on opposite sides of a single inverter card. The entire inverter device is subject to an ambient temperature, T_{amb}, which represents the temperature of the surrounding systems that might typically be encountered in a crowded environment such as an HEV. The target maximum temperature of the capacitor is 100°C.
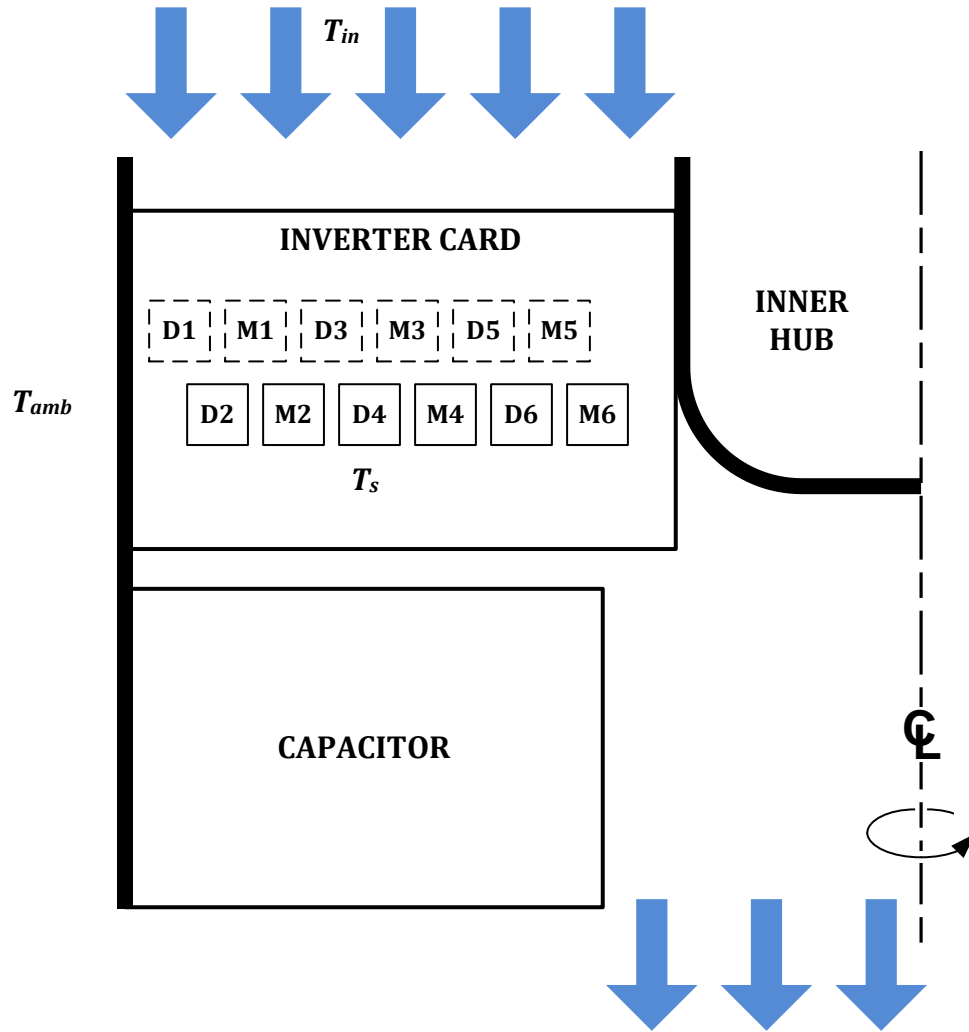
Figure 3.1 Axial inflow inverter descriptive schematic. Cross-sectional view facing one card

3.1 Heat Generation Model

This study is a continuation of the FY 2009 project which concluded with the radial inflow annular inverter design concept (see Figure 1.2 on page 4). In the aforementioned research, system behavior and maximum temperatures reported were determined based on a heat generation from the switches and diodes of 36 and 24 W, respectively. These values are typical for a 55-kW rated inverter [11]. In the present work, a more realistic heat generation model as a function of device junction temperature, T_j, is used. The heat generated from each device is to be determined from experiments performed on the benchmark devices at ORNL by Chinthavali et al. [14]. Since the device temperature is calculated is targeted in this study, an important emphasis is that the simulations will involve a feedback loop on T_j.

The experimental results are proportional to the conduction and switching heat losses, $\dot{q}_{cond}$ and $\dot{q}_{sw}$, respectively [25], where the measured dependent variables are expressed as a function of T_j. The proportionality relationships are

$$\dot{q}_{cond} \propto IR(T_j)^2 + V(T_j)I \tag{3.2}$$

$$\dot{q}_{sw} \propto f_{sw}E(T_j) \tag{3.3}$$

where:

E = Energy losses (J)

f_{sw} = Switching frequency (kHz)

I = Current (A)

R = Resistance (Ω)

T_j = Junction temperature (°C)

V = Voltage (V)

The dependency of R, V, and E on T_j are modeled as a polynomial with the coefficients determined from curve-fitting the experimental data obtained by Chinthavali et al. [14]. Although both

14

Si IGBT and SiC MOSFET switching technologies are examined in the experiments, only the SiC MOSFET technology power switches are modeled and are referred to as simply MOSFETs for short.

Note that the losses are proportional to the current through each device and that current is a fraction of the current supplied to the entire inverter. Additionally, the switching losses are scaled based on the current and voltage from which the experiments were performed. The final form of the heat generation model for both MOSFET power switches and Shottky diodes are

MOSFET heat generation [14]

$$\dot{q}_{cond,MOS} = 2I_{mos}^2\left(a_1 T_j + a_2\right) \tag{3.4}$$

$$a_1 = 2 \times 10^{-5} \frac{\Omega}{°C} \quad a_2 = 0.0132\ \Omega$$

$$\dot{q}_{sw,MOS} = \frac{1}{2} f_{sw}\left(b_1 T_j + b_2\right)\left(\frac{I_{mos}}{62.5\ A}\right)\left(\frac{V_{input}}{V_{scale}}\right) \tag{3.5}$$

$$b_1 = \begin{cases} 7 \times 10^{-7} \frac{J}{°C} & 300\ V \le V \le 500\ V \\ 4 \times 10^{-6} \frac{J}{°C} & 500\ V < V \le 700\ V \end{cases}$$

$$b_2 = \begin{cases} 0.0028\ J & 300\ V \le V \le 500\ V \\ 0.0038\ J & 500\ V < V \le 700\ V \end{cases}$$

$$V_{scale} = \begin{cases} 400\ V & 300\ V \le V \le 500\ V \\ 600\ V & 500\ V < V \le 700\ V \end{cases}$$

$$\dot{q}_{MOS} = \dot{q}_{cond,MOS} + \dot{q}_{sw,MOS} \tag{3.6}$$

Diode heat generation [14]

$$\dot{q}_{cond,diode} = 2I_{diode}^2\left(c_1 T_j^2 + c_2 T_j + c_3\right) + I_{diode}\left(d_1 T_j + d_2\right) \tag{3.7}$$

$$c_1 = 3 \times 10^{-7} \frac{\Omega}{°C^2} \quad c_2 = 2 \times 10^{-5} \frac{\Omega}{°C} \quad c_3 = 8.4 \times 10^{-3}\ \Omega$$

$$d_1 = -1.1 \times 10^{-3} \frac{V}{°C} \quad d_2 = 0.909\ V$$

$$\dot{q}_{sw,diode} = \frac{1}{2} f_{sw}\left(e_1 T_j + e_2\right)\left(\frac{I_{diode}}{62.5A}\right)\left(\frac{V_{input}}{V_{scale}}\right) \tag{3.8}$$

$$e_1 = \begin{cases} 4 \times 10^{-7} \frac{J}{°C} & 300 \text{ V} \leq V \leq 500 \text{ V} \\ 4 \times 10^{-5} \frac{J}{°C} & 500 \text{ V} < V \leq 700 \text{ V} \end{cases}$$

$$e_2 = \begin{cases} 8 \times 10^{-4} \text{ J} & 300 \text{ V} \leq V \leq 500 \text{ V} \\ 1.1 \times 10^{-3} \text{ J} & 500 \text{ V} < V \leq 700 \text{ V} \end{cases}$$

$$V_{scale} = \begin{cases} 400 \text{ V} & 300 \text{ V} \leq V \leq 500 \text{ V} \\ 600 \text{ V} & 500 \text{ V} < V \leq 700 \text{ V} \end{cases}$$

$$\dot{q}_{diode} = \dot{q}_{cond,diode} + \dot{q}_{sw,diode} \tag{3.9}$$

The heat generation model is plotted in Figure 3.2 for the parametric values of V and f_{sw} to be used in the computational simulations in this investigation.
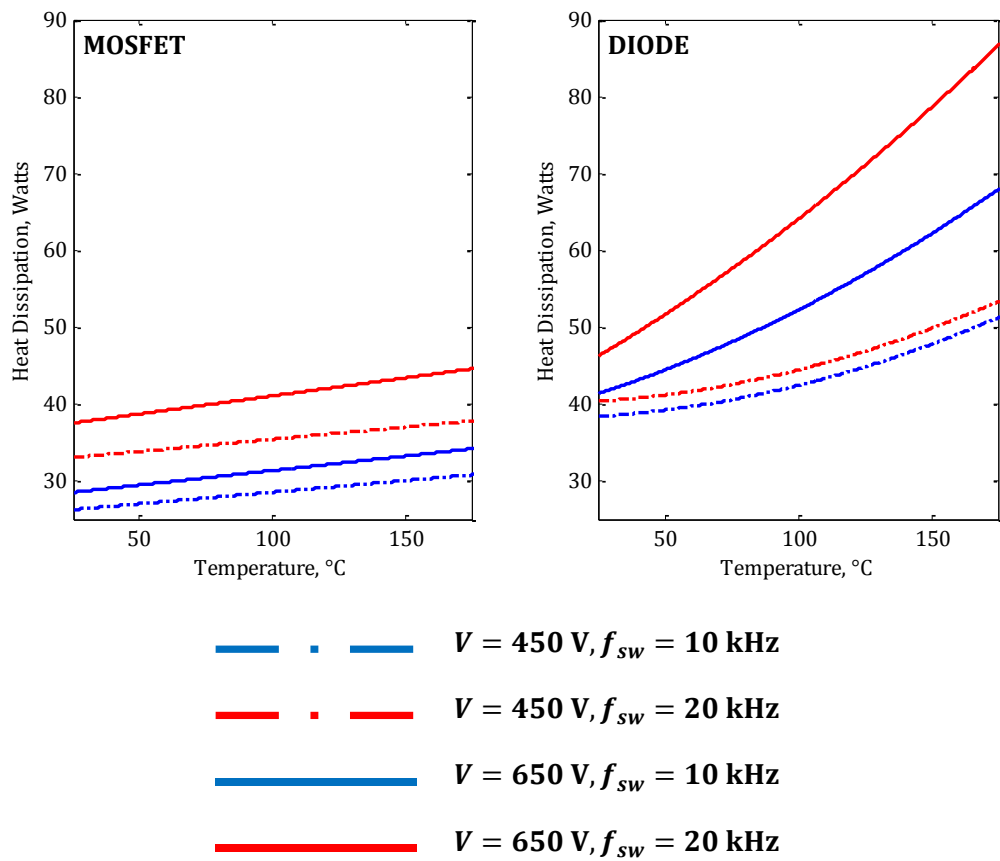
Figure 3.2 Heat generation model for (a) SiC MOSFET power switch and (b) Shottky diode at various voltage and switching frequency, with $I_{mos} = I_{diode} = 27A$ [14]

3.2 Modeling Parameters

Competitive design targets are set in order to confidently claim the applicability of this investigation to industrial needs. The values of this parametric study are ideally determined based on foreknowledge of parametric values commonly encountered in the automotive industry. The inverter design concept is benchmarked against those of current HEVs such as the Prius® or the Insight®. The literature has suggested that a power inverter marketed towards these vehicles can be acceptably rated for anywhere from 200 V [14] to 1200 V [20] with switching frequencies in the vicinity of 20 kHz [14].

The United States Office of Transportation and Air Quality (OTAQ) of the Environmental Protection Agency (EPA) publishes a vehicle emissions federal test procedures (FTP) for light-duty vehicles and light-duty trucks. Furthermore, the OTAQ makes available vehicle target speed drive profiles that are periodic in time to represent the conditions of a test procedure. However, a supplemental FTP (SFTP) was needed in order to address shortcomings of the tailpipe emissions portion of the current procedure due to an inadequate representation of "aggressive (high speed and/or high acceleration) driving behavior, rapid speed fluctuations, driving behavior following startup, and the use of air conditioning" [26]. The EPA designated this supplemental procedure "US06" and is representative of 596 seconds, 8.01 driven miles, and an average speed 48.37 mph. The appropriate technical personnel at ORNL have recognized this supplemental procedure as a good representative operational drive cycle condition given the purpose of the revision to the current FTP and the objective of this study. This data was used to calculate electric current that would be encountered in a HEV power inverter and is reproduced in Figure 3.3 in units of miles per hour (mph) directly from the OTAQ and in units of amperes from ORNL. Figure 3.3 (c) is the absolute value of the current which will be used in equations (3.4) through (3.9) because heat generation is based on the magnitude of the current.

18
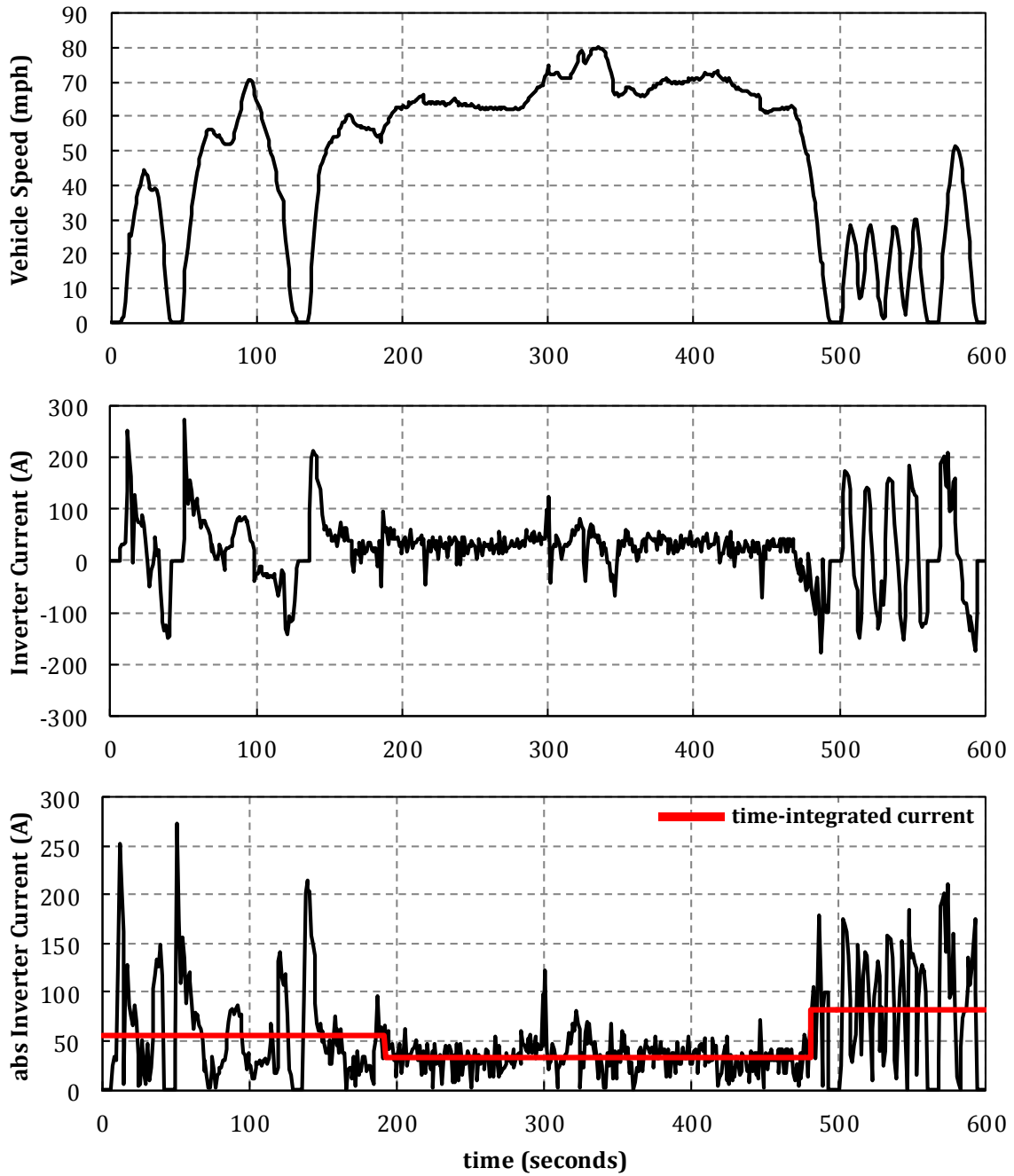
Figure 3.3 EPA Supplemental Federal Test Procedure US06 drive cycle in units of (a) vehicle speed in miles per hour [26], (b) current to inverter in amperes, $I_{US06}(t)$, and (c) absolute current inverter to inverter in amperes, $|I_{US06}(t)|$

19

One may observe that the US06 Drive Cycle can be segmented into three sections, which are [0,192) seconds, [192,482] seconds, and (482,602] seconds. The respective time-integrated current of these three time intervals are 56, 34, and 82 A and are represented by the red horizontal line in Figure 3.3 (c) for each interval. A steady-state simulation can be appropriately evaluated at the highest inverter current of the time intervals, 82 A to evaluate the steady-state thermal performance to compare with the final temperature in a transient analysis.

The total number of inverter cards for the purposes of this investigation is $N = 9$ cards. Observe that the radial inflow inverter thermal plot in Figure 1.2 utilizes the radial symmetry and has a $360°/N = 40°$ angle between symmetry planes. In light of this and also assuming that each MOSFET power switch and Shottky diode will be supplied the same current, the current value of equations (3.4) through (3.9) is $I_{MOS} = I_{diode} = \frac{|I_{US06}(t)|}{N}$. The current for a steady-state simulation at the highest time-integrated current level will be $82/9 = 9.1$ A. The heat generation model plotted in Figure 3.2 is plotted for $I_{MOS} = I_{diode} = 27$ A which represents $240\,\mathrm{A}/N$ since this current is the near maximum value of the US06 drive cycle plotted in Figure 3.3 (c).

The cylindrical shape of the axial inflow inverter concept takes advantage of convenient placement of an axial fan as well as a cylindrical ring capacitor it accommodates similar to that of Figure 3.4 (a). The "power ring" is the assembled capacitor with the housing and external connections as in Figure 3.4 (b) [27]. The capacitor to be used in this investigation is based on a modified power ring from SB Electronics® and is in fact modeled in Figure 1.2 on page 4. A prudent assumption is that this capacitor, although extremely efficient, generates heat as it stores and passes electrical energy due to marginally small inefficiencies. For the purposes of this simulation, the capacitor dissipates 10 W. A computer simulation that models a 40° sweep of the annular inverter will generate $10\,\mathrm{W} \times \frac{40°}{360°}$ of heat.
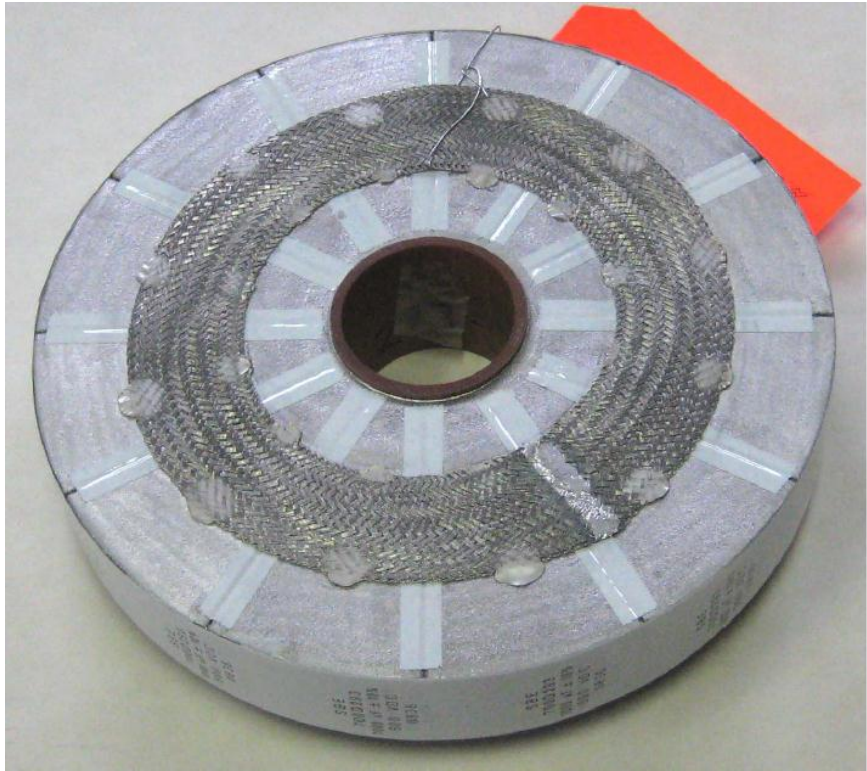
(a)
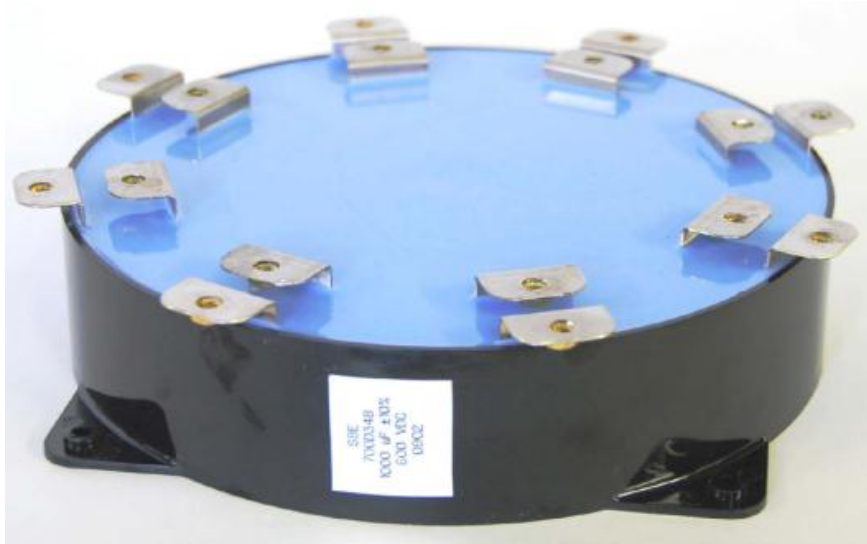
(b)

Figure 3.4 SB Electronics® [27] (a) internal capacitor and (b) power ring assembly

3.3 Computational Fluid Dynamics

3.3.1 Governing Equations

Fundamental assumptions are established before proceeding to other modeling techniques. The fluid flow is incompressible and Newtonian, therefore mass and momentum is conserved. Furthermore, fluid properties are not a function of temperature in the simulations which allows for the thermal decoupling of the mass and momentum conservation laws from the conservation of energy. The governing vector equations of fluid dynamics in light of the fundamental assumptions together with the conservation of energy and auxiliary relationships are

Conservation laws [28]

$$\mathbf{\nabla} \cdot \mathbf{u} = 0 \tag{3.10}$$

$$\rho \frac{D\mathbf{u}}{Dt} = \rho \mathbf{g} - \mathbf{\nabla} p + \mu \mathbf{\nabla}^2 \mathbf{u} \tag{3.11}$$

$$\rho c_p \frac{DT}{Dt} = \dot{q} + k\nabla^2 T + \Phi \tag{3.12}$$

Auxiliary relations [28]

$$\frac{D}{Dt} = \frac{\partial}{\partial t} + (\mathbf{u} \cdot \mathbf{\nabla}) \tag{3.13}$$

$$\mathbf{u} \cdot \mathbf{\nabla} = u_i \frac{\partial}{\partial x_i} + u_j \frac{\partial}{\partial x_j} \tag{3.14}$$

$$\Phi = \mu \left(\frac{\partial u_i}{\partial x_j} + \frac{\partial u_j}{\partial x_i} \right) \frac{\partial u_i}{\partial x_j} \tag{3.15}$$

Air flowing through the axial inflow inverter will be coming from an axial fan placed above the inverter. In light of this and the complex flow path indicated by Figure 3.1, we proceed under the assumption that the flow is most correctly assumed to be turbulent (not laminar). The Reynolds number, Re, is calculated based on the inlet area and velocity and kinematic viscosity as

$$Re_{D_h} = \frac{V D_h}{\nu} \tag{3.16}$$

The turbulent flow approximation is valid, since the Reynolds number at the inlet area is $Re_{D_h} \cong 4800 > 4000$ for a flow rate of $Q = 30$ cfm per unit cell, which is a total flow rate of $Q \times N = 270$ cfm. This assumption will significantly impact and should improve the results since turbulent kinetic energy is dissipated into thermal internal energy which is a feature not captured by a laminar flow heat transfer model [29]. Turbulent flow modeling as discussed in Wilcox assumes that the Boussinesq approximation for turbulent flow is valid—that is, the molecular kinematic viscosity is augmented with a turbulent kinematic viscosity, ν_T [29]. The specific Reynolds-stress tensor and the specific turbulent kinetic energy, k, that are used in virtually all turbulence energy equation models are [29] therefore

$$\tau_{ij} = 2\nu_T S_{ij} - \frac{2}{3}k\delta_{ij} \tag{3.17}$$

$$\frac{\partial k}{\partial t} + U_j \frac{\partial k}{\partial x_j} = \tau_{ij}\frac{\partial U_i}{\partial x_j} - \epsilon + \frac{\partial}{\partial x_j}\left[(\nu + \nu_T/\sigma_k)\frac{\partial k}{\partial x_j}\right] \tag{3.18}$$

The two closure models for (3.18) used in this study are known as the "standard $k\text{-}\epsilon$" and the "Wilcox (2006) $k\text{-}\omega$," or $k\text{-}\epsilon$ and $k\text{-}\omega$, respectively. Both are models of the specific turbulent kinetic energy, k, with the difference being that either the specific energy dissipation, ϵ, or specific energy dissipation rate, ω is modeled. Among the many parameters in these closure models, the turbulent length scale, l_T, can be arbitrarily chosen as well as the velocity scale, $k^{3/2}$ and will be addressed in the discussion on boundary conditions. The two closure models are as follows:

Wilcox (2006) $k\text{-}\omega$ model [29]

Kinematic Eddy Viscosity:

$$\nu_T = \frac{k}{\tilde{\omega}}, \quad \tilde{\omega} = \max\left\{\omega, C_{lim}\sqrt{\frac{2S_{ij}S_{ij}}{\beta^*}}\right\}, \quad C_{lim} = \frac{7}{8} \tag{3.19}$$

Turbulence Kinetic Energy:

$$\frac{\partial k}{\partial t} + U_j \frac{\partial k}{\partial x_j} = \tau_{ij}\frac{\partial U_i}{\partial x_j} - \beta^* k\omega + \frac{\partial}{\partial x_j}\left[\left(\nu + \sigma^*\frac{k}{\omega}\right)\frac{\partial k}{\partial x_j}\right] \tag{3.20}$$

23

Specific Dissipation Rate:

$$\frac{\partial \omega}{\partial t} + U_j \frac{\partial \omega}{\partial x_j} = \alpha \frac{\omega}{k} \tau_{ij} \frac{\partial U_i}{\partial x_j} - \beta \omega^2 + \frac{\sigma_d}{\omega} \frac{\partial k}{\partial x_j} \frac{\partial \omega}{\partial x_j} + \frac{\partial}{\partial x_j} \left[\left(\nu + \sigma \frac{k}{\omega} \right) \frac{\partial \omega}{\partial x_j} \right] \qquad (3.21)$$

Dimensionless Closure Coefficients and Auxiliary Relations:

$$\alpha = \frac{13}{25}, \ \beta = \beta_o f_\beta, \ \beta^* = \frac{9}{100}, \ \sigma = \frac{1}{2}, \ \sigma^* = \frac{3}{5}, \ \sigma_{do} = \frac{1}{8} \qquad (3.22)$$

$$\sigma_d = \begin{cases} 0, & \frac{\partial k}{\partial x_j} \frac{\partial \omega}{\partial x_j} \leq 0 \\ \sigma_{do}, & \frac{\partial k}{\partial x_j} \frac{\partial \omega}{\partial x_j} > 0 \end{cases} \qquad (3.23)$$

Standard k-ϵ model [29]

Kinematic Eddy Viscosity:

$$\nu_T = C_\mu k^2 / \epsilon \qquad (3.24)$$

Turbulence Kinetic Energy:

$$\frac{\partial k}{\partial t} + U_j \frac{\partial k}{\partial x_j} = \tau_{ij} \frac{\partial U_i}{\partial x_j} - C_{\epsilon 2} \frac{\epsilon^2}{k} + \frac{\partial}{\partial x_j} \left[(\nu + \nu_T / \sigma_\epsilon) \frac{\partial \epsilon}{\partial x_j} \right] \qquad (3.25)$$

Dissipation Rate:

$$\frac{\partial \epsilon}{\partial t} + U_j \frac{\partial \epsilon}{\partial x_j} = C_{\epsilon 1} \frac{\epsilon}{k} \tau_{ij} \frac{\partial U_i}{\partial x_j} - C_{\epsilon 2} \frac{\epsilon^2}{k} + \frac{\partial}{\partial x_j} \left[(\nu + \nu_T / \sigma_\epsilon) \frac{\partial \epsilon}{\partial x_j} \right] \qquad (3.26)$$

Dimensionless Closure Coefficients and Auxiliary Relations:

$$C_{\epsilon 1} = 1.44, \ C_{\epsilon 2} = 1.92, \ C_\mu = 0.09, \ \sigma_k = 1.0, \ \sigma_\epsilon = 1.3 \qquad (3.27)$$

Note that the turbulent kinematic viscosity, ν_T, is modeled as a property of the flow in both cases. As a guideline, the k-ϵ model is generally more stable than k-ω model albeit less accurate in some instances [28]. The two closure models are related [29] by

$$\omega = \epsilon / (C_\mu k), \text{ and } l = C_\mu k^{3/2} / \epsilon \qquad (3.28)$$

These relationships give the user flexibility in solving for the velocity field and pressure distribution with both models. This can be advantageous for highly complex geometries or highly non-

linear flow simulations when accuracy must be traded for convergence in order to initialize a converged solution.

When the fluid turbulent model is employed, the velocity field obtained is used to calculate both the solid and fluid field temperatures. Viscous heating and pressure work are ignored in the temperature solution, and the constant properties assumption is once again employed. The governing equation of heat transfer reduces to

$$\rho c_p \frac{\partial T}{\partial t} + \nabla \cdot [(k + k_T)\nabla T] = \dot{q} - \rho c_p \mathbf{u} \cdot \nabla T \tag{3.29}$$

for which $(k + k_T)$ are respectively defined as the thermal conductivity augmented with the turbulent thermal conductivity, defined as

$$k_T = \frac{c_p \mu_T}{Pr_T} \tag{3.30}$$

The velocity field is zero in a solid, yielding k_T and the second term on the right hand side of (3.29) to zero where these equations are applied for solid domains. The heat generated, $\dot{q}$, is replaced with the conduction plus the switching losses, $\dot{q}_{cond} + \dot{q}_{sw}$ (see 3.1 Heat Generation Model, page 14). The turbulent thermal conductivity, k_T, is modeled using a correlation for the turbulent Prandtl number, Pr_T, from Kays et al. which will be used again in the thermal wall functions [30], stated as

$$\frac{1}{Pr_T} = \frac{1}{2Pr_{T\infty}} + \frac{0.3}{\sqrt{Pr_{T\infty}}} \frac{c_p \mu_T}{k} - \left(0.3 \frac{c_p \mu_T}{k}\right)^2 \left[1 - \exp\left(-\frac{k}{0.3 c_p \mu_T \sqrt{Pr_{T\infty}}}\right)\right] \tag{3.31}$$

$$Pr_{T\infty} = 0.85 \tag{3.32}$$

$$\mu_T = \nu_T \rho \tag{3.33}$$

That the dimensionless group $Pr_T = c_p \mu_T / k_T$ is strictly derived as a property of the flow is a key distinction. Note that μ_T and Pr_T are a function of the turbulent kinetic energy.

3.3.2 Boundary Conditions

The manner in which boundary conditions are specified can have a significant impact on the final solution as well as the solution methodology. When resources of time or processing capability

have an impact on the solution approach, boundary conditions of the problem can likely be affected. For turbulent flow, one may wish to accurately represent any of the circulation zones that are expected in a computational model or solve for a velocity solution in the vicinity of wall boundaries, but doing so may require the user to add multiple steps to a solution approach before a final solution is obtained. Limitations on computational resources can also be accounted for by taking advantage of the radial symmetry such as was the case in Figure 1.2 on page 4.

An exact surface boundary condition for turbulent flow modeling follows from the no-slip condition such that $\tau_{ij}(y = 0) \equiv \tau_w = 0$ when y is the coordinate direction perpendicular to the wall [29]. However, the velocity solution cannot be resolved all the way to the wall in a straightforward manner. A small distance away from the wall is chosen for which the fluid velocity is specified according to Wilcox [29] as

$$U^+ = \frac{U}{u_\tau} = \left[\frac{1}{\kappa}\ln(y^+) + C\right] \tag{3.34}$$

$$u_\tau = \sqrt{\tau_w/\rho} \tag{3.35}$$

$$y^+ = \frac{u_\tau y}{\nu} = \frac{\rho C_\mu^{1/4} k^{1/2} y}{\mu} \tag{3.36}$$

where:

U^+ = Dimensionless velocity

u_τ = Friction velocity

y^+ = Dimensionless, sublayer-scaled distance

C = Dimensionless closure coefficient, 5.5

κ $\cong$ Von Kármán constant, 4.4

Typically, convergence is achieved when y^+ is chosen far from the wall. Upon obtaining an initial solution specifying $y^+ \leq 200$, successive solutions can be obtained by stepping down this parameter to $y^+ \cong 30$ which is the lower limit for which y^+ is defined [28].

The wall boundary conditions for the turbulent flow terms, k, ϵ, and ω are derived from stating that turbulent energy production equals dissipation [29]. The wall functions for these turbulent flow parameters are defined as

$$k = \frac{u_\tau^2}{\sqrt{\beta^*}}, \quad \omega = \frac{k^{1/2}}{\beta^{*1/4}\kappa y}, \quad \epsilon = \beta^{*3/4}\frac{k^{3/2}}{\kappa y} \tag{3.37}$$

The flow inlet boundary condition specification involves a simple value for the inflow velocity. The turbulent flow parameters are either chosen as turbulence length scale, L_T, and turbulence intensity, I_T, or initial values for k and ϵ or ω, denoted k_0, ϵ_0, and ω_0, respectively. When choosing to specify L_T and I_T, lower values will cause for small eddies to be resolved and will thus be more accurate but may require that the value be stepped down in a similar manner as was discussed for y^+. Choosing values of $I_T = 0.1\%$ and $L_T = 0.001$ m are sufficient for the purposes of this investigation.

Choosing an outflow boundary affects solution convergence as well as CPU time to solve the problem. As before, one may choose to specify an outflow boundary incorrectly to obtain a converged solution before proceeding to calculate a final solution that would not converge without intermediate steps. As some of the air flow makes a 90° turn downwards when entering the center hole of the capacitor before exiting the outflow boundary, a circulation zone may reside in the vicinity of the capacitor, represented in the simplified schematics in Figure 3.5 which shows two possible outflow boundaries that are considered in the interest of obtaining an accurate solution. The boundary conditions in Figure 3.5 (a) and (b) are respectively

$$(\mu + \mu_T)\left(\nabla \mathbf{u} + (\nabla \mathbf{u})^{\mathrm{T}}\right) \cdot \mathbf{n} = \mathbf{0}, \; p = 0 \tag{3.38}$$

$$-p + (\mu + \mu_T)\left(\nabla \mathbf{u} + (\nabla \mathbf{u})^{\mathrm{T}}\right) \cdot \mathbf{n} = -f_0\mathbf{n}, \; p \cong f_0 = 0 \tag{3.39}$$

Note that the pressure at the outlet is either explicitly or implicitly defined in these equations. The outlet boundary condition of Figure 3.5 (a) can greatly improve the ability for a finite element model to reach convergence. This condition is ideal when the flow is expected to be fully developed with streamlines perpendicular to the exit plane, ensure that the uniform pressure specification is ac-
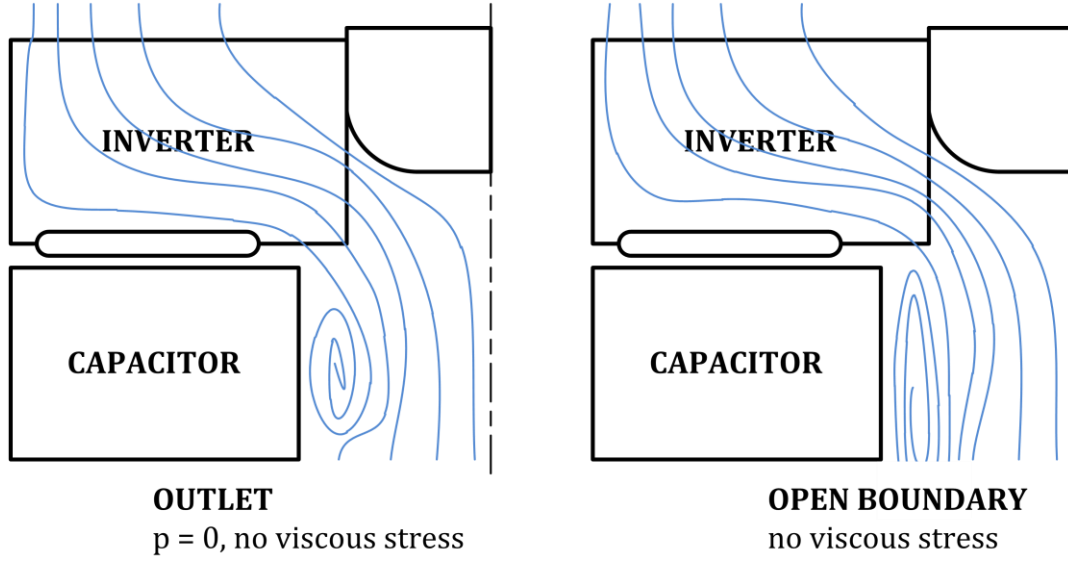
Figure 3.5 Outflow boundary conditions representing (a) pressure-corrected with no mass inflow across boundary and (b) small inflow quantity crossing the boundary possible

curate. In this instance, the model no longer accounts for the possibility of a small amount of mass inflow at this boundary such as is the case when an outlet boundary is placed nearby expected recirculation zones. The boundary condition of Figure 3.5 (b) is similar yet more accurate since it allows for small amounts of mass inflow at the exit plane at the cost of less-strict convergence criteria.

The thermal interaction with the flow quantities calculated using the methods described above are modeled using the temperature law of the wall given as (3.40) that enables us to obtain a temperature solution from the wall to y^+ even though the flow solution is not specifically calculated in this region [28]. The thermal wall function is a heat flux boundary condition, and the resistance to heat transfer is related to the resistance to momentum transport through

$$T^+ = \frac{T_w - \bar{T}}{T^*} = \int_0^{y^+} \frac{dy}{1/Pr + \mu_T(y)/\mu Pr_T(y)} \tag{3.40}$$

$$T^* = \frac{q_w}{\rho c_p u_\tau} \tag{3.41}$$

$$q_w'' = \frac{\rho c_p C_\mu^{1/4} k^{1/2}(T_w - T)}{T^+} \tag{3.42}$$

Thermal feasibility is also established for high temperature ambient environments, thus the outer wall interaction with the environment is given in (3.43) [31].

$$q'' = h(T_s - T_{amb}) \tag{3.43}$$

where:

h = Convection coefficient, $W/(m^2 \cdot K)$

q'' = Heat flux, W/m^2

T_{amb} = Ambient temperature, °C

T_s = Solid domain temperature, °C

3.4 Model Properties

The capacitor is made of radially wound zinc material and is modeled as an anisotropic material. The thermal conductivity is defined for the radial and tangential directions due to the winding. The capacitor thermal conductivity, k_{CAP}, is redefined in Cartesian coordinates in (3.44) [3] as

$$k_{CAP} = \begin{bmatrix} \frac{x^2}{x^2+y^2}k_{rr} + \frac{y^2}{x^2+y^2}k_{\theta\theta} & \frac{xy}{x^2+y^2}k_{rr} - \frac{xy}{x^2+y^2}k_{\theta\theta} & 0 \\ \frac{xy}{x^2+y^2}k_{rr} - \frac{xy}{x^2+y^2}k_{\theta\theta} & \frac{y^2}{x^2+y^2}k_{rr} + \frac{x^2}{x^2+y^2}k_{\theta\theta} & 0 \\ 0 & 0 & k_{zz} \end{bmatrix} \tag{3.44}$$

where:

k_{rr} = Capacitor radial thermal conductivity, 113 W/(m·K)

$k_{\theta\theta}$ = Capacitor tangential thermal conductivity, 0.15 W/(m·K)

All other materials are considered to be isotropic and are listed below together with the source of the material properties.

Table 3.1 Properties of Materials

	Density	**Thermal conductivity**	**Specific heat**	**Dynamic viscosity**	**Source**
	ρ	k	c_p	μ	
	kg/m^3	$W/(m \cdot K)$	$J/(kg \cdot K)$	$N \cdot s/m^2$	
Torlon	1 410	0.259			[32]
Copper	8 933	401.0	385		[31]
Zinc	7 140	113.0	389		[31]
Cotronics® 914 Ceramic	2 225	0.403 8	835		[33]
Aluminum Nitride	8 933	148.0	385		[34]
316 Stainless Steel	8 238	13.40	468		[31]
Aluminum	2 770	177.0	875		[31]
Silicon Carbide	3 100	370.0	690		[35]
Silicone Gel	2 330	0.170	712		[36]
Air at 300K	1.1614	0.026 3	1 007	184.6×10^{-7}	[31]

3.5 Implementation

3.5.1 Procedure

The computations are performed using the governing equations as specified above with COMSOL Multiphysics® computer software which is used to solve vector equations in complex three-dimensional domains using the finite element method (FEM). With considerations regarding mesh element length, computational resources, and time aside, an *ideal* guideline for stable turbulent flow heat transfer modeling which captures the physics of the problem accurately are summarized below.

1. Set $y^+ = 150$ in the wall boundary conditions and ensure the outlet boundary condition is specified such that $p = 0$ and mass inflow is not possible. Solve for the velocity field and pressure distribution using the k-ϵ model.

2. Step down y^+ until $y^+ \cong 70$ and solve for the flow quantities using the k-ϵ model. This process can take several iterations depending on the stability of the computations as y^+ is decreased.

3. Change the outlet boundary condition to allow marginal mass inflow with no pressure correction. Solve for the flow quantities using the k-ω model.

4. Step down y^+ until $y^+ \cong 30$ in the wall boundary conditions and solve for the flow quantities using the k-ω model.

5. Solve for a final fluid and solid temperature distribution given that the results conserve mass, momentum, and energy.

When project constraints of time and computational resources are in place, a sufficient turbulent flow model is solved using the k-ϵ turbulence model with a wall boundary condition that specifies $30 \leq y^+ \leq 50$, and the outlet boundary condition with the zero pressure condition (3.38) is used since an accurate model of the recirculation zone in the vicinity of the capacitor does not contribute to

the key objective of this study. When the nonlinear flow quantities are solved for, the temperature

solution is obtained in a straightforward manner using the parameters as previously described.

3.5.2 Verification

Mesh characteristics of finite element method computations contribute significantly to the accuracy of the results but are also subject to the project constraints as with everything else previously

discussed. Mesh guidelines are established using simplified models that solve the same equations

used in the present study. A computational model consisting of a heat-generating chip mounted to a

flat substrate is investigated, and cooling air flows past the chip and plate assembly, reducing the

temperature of the system. A simplified 2D schematic is given in Figure 3.6 although the computations are performed in a three-dimensional domain. The chip is generating 36 W of heat for the purpose of this investigation. The chip is insulated on the top and the sides so that heat only flows into

the substrate and transfers to the fluid from the substrate surface. Furthermore, the only non-insulated

boundary of the substrate is the surface that interacts with the chip and the surfaces that are exposed

to air flow. The thermal energy is therefore routed from the chip to the substrate and to the air flow

domain. In a perfectly modeled steady-state system, the energy at the inflow boundary is equal to the

energy at the outlet boundary plus the energy from the heat-generating chip. The global energy balance error is computed with respect to the heat generated in the chip as

$$e = \left(\frac{q_{out} - q_{in}}{\dot{q}_{gen}} - 1 \right) \times 100\% \qquad (3.45)$$

where:

e $\quad = \quad$ Energy balance error, %

q_{in} $\quad = \quad$ Total energy entering the flow domain, W

q_{out} $\quad = \quad$ Total energy leaving the flow domain, W

$\dot{q}_{gen}$ $\quad = \quad$ Heat generated in the chip, W

The large size of the air domain is chosen to impose the boundary condition that the far field is unaffected by the presence of the chip and the substrate. For this reason, symmetric boundary conditions are used to impose a mean flow parallel to the air domain boundaries.

The primary purpose of the simplified model is to study the effect of mesh on the results and to establish a relationship between energy balance and maximum temperature. The domain properties and boundary conditions are consistent in all of the models, but the turbulence model employed is variable and documented for each computation since mesh dependency may be a function of the set of equations employed. The mesh refinement and relevant model characteristics are summarized below, with the velocity field and pressure distribution first solved using the k-ϵ turbulence model.

A. A default mesh consisting of linear finite elements is established and refined once.

B. Model (A) with quadratic elements

C. Model (B) solved with the global convergence tolerance reduced from 10^{-3} to 10^{-4}

D. Model (C) with a once-refined mesh using default refinement settings

E. Model (D) with a once-refined mesh using default settings. Turbulent flow quantities are now solved for using the k-ω model.

F. Model (E) with a once-refined mesh using an adaptive refinement method.

The heat transfer rate is integrated across the boundaries, and intermediate as well as global energy balances are computed from the results. The area-integrated heat transfer rates are denoted as $q_1, q_2, \ldots, q_6$ and are presented in Watts in Table 3.2 along with the energy balance results. The relationship between maximum device temperature and energy balance is given in Figure 3.7, showing a decreasing mesh dependency with increasing mesh density. We proceed to apply these results to more complex systems by recognizing that the maximum temperature of the computations may be slightly higher with increased mesh density. This knowledge plays a part in the decision-making process with regards to project constraints and other verification methods. Essentially, limited resources cause us to preserve conservative assumptions and pursue aggressive design targets.

33
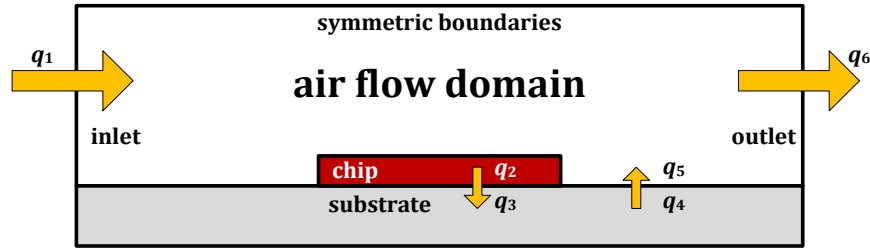
Figure 3.6 Simplified schematic of verification model

Table 3.2 Verification study results

| | | Normal total heat transfer rate (W) | | | | | | T (°C) | | Energy balance | |
	Model	q_1	q_2	q_3	q_4	q_5	q_6	Min	Max	$\dfrac{q_5 - q_4}{q_4}$	$\dfrac{q_6 - q_1}{q_2}$
A	k-ϵ	1360.6	36.0	32.8	31.4	37.8	1403.8	357.5	**378.0**	21%	**20.1%**
B	k-ϵ	1360.6	36.0	32.8	31.4	40.3	1400.1	387.9	**408.0**	28%	**9.8%**
C	k-ϵ	1360.6	36.0	32.8	31.4	40.3	1400.1	387.9	**408.0**	28%	**9.8%**
D	k-ϵ	1360.6	36.0	33.5	32.4	39.1	1399.8	395.0	**416.0**	21%	**8.9%**
E	k-ω	1360.6	36.0	33.5	32.4	39.5	1399.6	389.6	**409.8**	22%	**8.5%**
F	k-ω	1360.6	36.0	34.8	34.6	38.3	1399.7	391.4	**411.6**	11%	**8.6%**
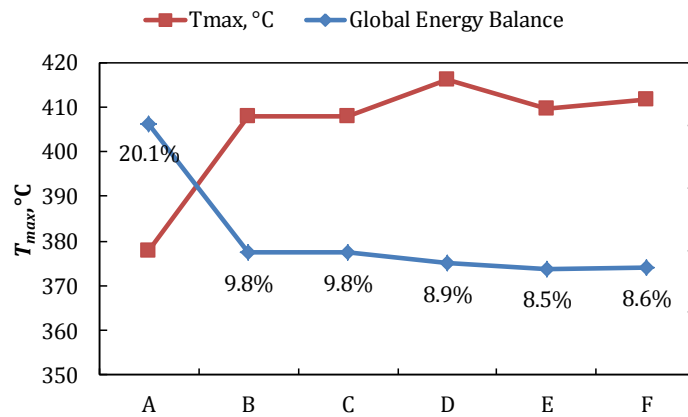
Figure 3.7 Verification study results

34

3.5.3 Summary

Both steady-state and transient solutions are obtained. For both of these solutions, heat generation is based on the electric operational parameters of the devices (switching frequency, current, and voltage) and the junction temperature, T_j. In the steady-state case, current is kept constant, and in the transient case, the current is a function of time as obtained from the EPA US06 drive cycle (Figure 3.3 on page 19).

The problem is solved using the logic of Figure 3.8 which is intended to describe how the input parameters are used to obtain a solution that translates to thermal feasibility and performance of the air-cooled inverter. A unique aspect of this project is the iteration on T_j, shown as a feedback loop in Figure 3.8 An initial junction temperature is specified for which the initial value of $\dot{q}_{cond} + \dot{q}_{sw}$ for each MOSFET and diode is calculated. With these values, the inlet air temperature, ambient air temperature, and air flow rate, a junction temperature is calculated. Succeeding iterations of junction temperature also iterate on $\dot{q}_{cond} + \dot{q}_{sw}$ until a converged solution is obtained. In transient investigations, the convergence on T_j and $\dot{q}_{cond} + \dot{q}_{sw}$ is necessary in order to proceed to the next time step. This approach is an accurate way to model the heat generation as described since the experiments suggested this temperature dependency [14]. In previous years and in the literature cited that simulated a thermal packing concept applied to power electronics, this approach has not been attempted to problems of this nature to the best of our knowledge.
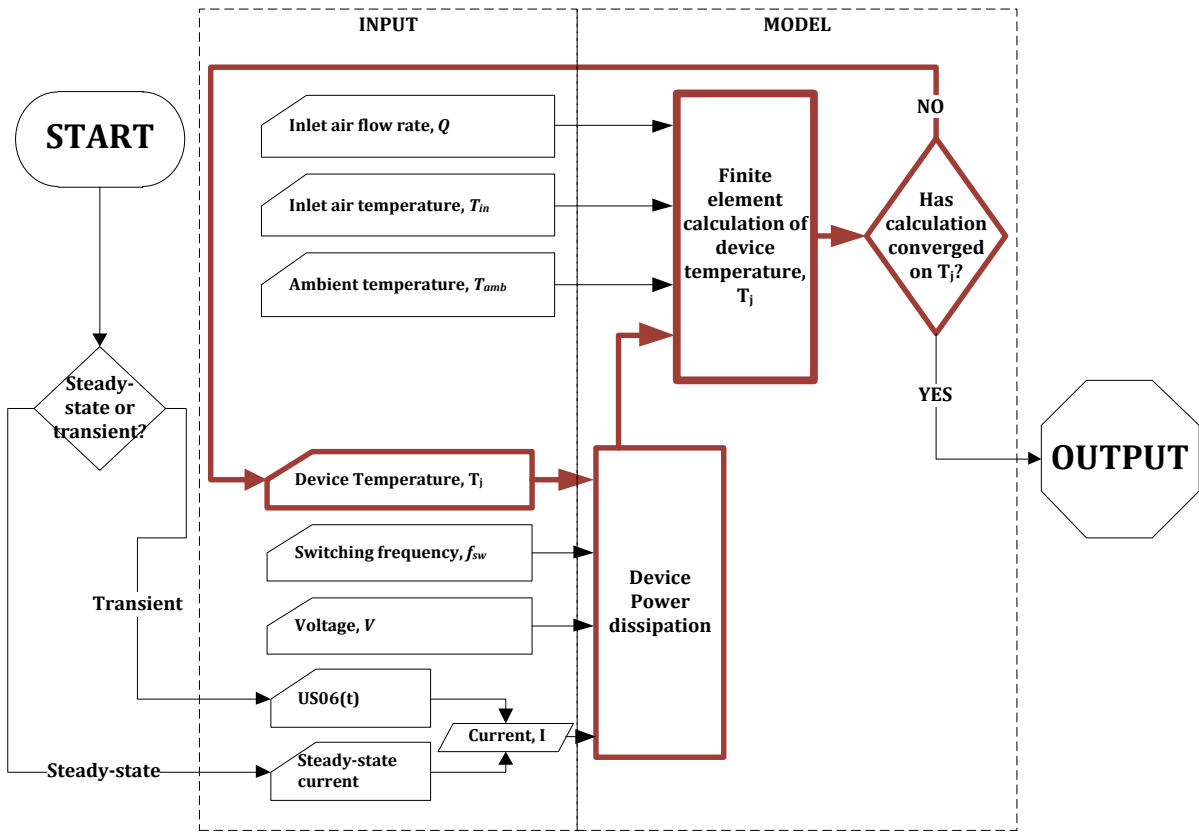
Figure 3.8 Logic diagram for numerical solution procedure

Chapter 4. Preliminary Results

4.1 Overview

The axial inflow inverter concept undergoes continuous revision as design goals are communicated over the course of the year. Figure 4.1 shows the major milestones of the project over the course of FY 2010, beginning on October 1st, 2009 with a first objective to quantify the relationship between the axial inflow inverter in the present investigation and the radial inflow inverter in the FY 2009 study. When major changes to the design concept are encountered, the revision quantifier is updated. This may include major geometric changes or inverter circuitry layout. Each major revision is denoted as A, B, etc. while minor revisions are denoted AA, AB, AC, etc. Minor changes may include small geometric changes or material properties.

As Figure 4.1 illustrates, most of the design process was performed in the absence of the final heat generation model of (3.4) through (3.9) on page 15 and the US06 drive cycle in Figure 3.3 on page 19. Revisions A through D were evaluated at heat generation levels of 24 and 36 W dissipated in each power switch and diode in order to maintain consistency with the investigations of FY 2009 [3]. The significance of finalizing the heat generation model is consistent with the timing between
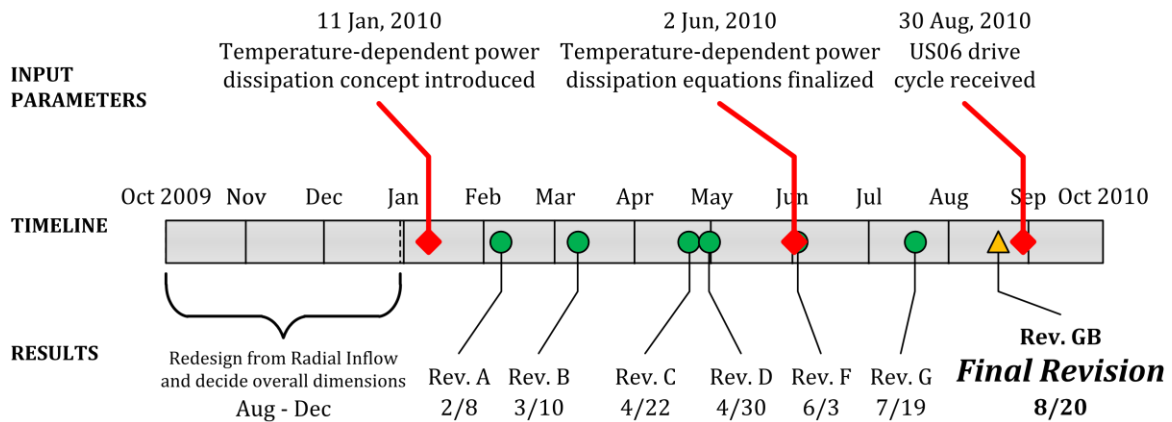
Figure 4.1 Project timeline

37

concept revisions denoted "Rev. F" and "Rev. G." The current supplied to the devices per the heat generation model described previously was $I_{MOS} = I_{diode} = 240/N$ A due to a prior knowledge of the approximate maximum value of the EPA US06 drive cycle. However, the highest time-integrated current for the third interval of the drive cycle is 82 A. Thus, concept Revision G was given aggressive design targets relative to what was required when using the federal test procedures from the EPA. A housing structure was only designed after thermal feasibility was established, and previous revisions are not presented with a housing design. Note that the time that the heat generation model was received does not affect the efforts to lower the ideal blower power input to the system. That is, changes made along the way to lower pressure drop were not affected even though changes made to lower device temperature were affected.

A detailed discussion of the first concept model is given in order to introduce the variables that are important in this design process. Further discussion highlights how each of the important aspects of the design process impacts the results. Thus, in subsequent designs, only the impact of the design changes on the results are presented and discussed.

4.2 Initial Concept

The first concept of the axial inflow inverter is presented in Figure 4.2 which is a cut-away view of the concept. A color scheme is chosen only for visualization purposes as is the case for the presentation of subsequent concepts. The purpose of the first model is to maintain consistency with the radial inflow inverter concept. Specifically, the initial axial inflow inverter concept compares readily with the radial inflow inverter concept without cooling fins. There are three inverter cards for each of the three phase legs in this concept, giving nine total inverter cards. The cards are configured radially over a circular capacitor and air flows downward (i.e. from top to bottom) around the inner hub and each inverter card and through the center hole in the capacitor. The inner hub is sized so that the minimum flow area between the inner edge of the capacitor and the rounded edge of the inner hub

is not smaller than the exit area. The total diameter and height are 9.25 inches (235 mm) and 3.9 inches (100 mm), respectively, and the total volume is 265 cubic inches (4.3 L).

The top and bottom halves of the card can be thought of as "phase" and "DC" sides, respectively. The phase and DC half of each card contains three devices—two power switches and one diode—which are evenly spaced as close to the leading edge as possible where the heat transfer coefficient is the highest. The devices are mounted to a DBC construction with AlN as the substrate material. A thermal barrier made of Cotronics® Rescor 914 Glass Ceramic [33] is placed between the inverter cards and the capacitor in order for heat to be routed away from the capacitor. The card is mounted to the capacitor via the tabs that also connect the DC positive and negative capacitor terminals to the inverter cards. The capacitor represents a modified power ring from SBElectroncs® similar to the power ring in Figure 3.4 on page 21 with the key difference being that the power ring here has a central hole to allow air to flow through it. The only major difference of the first concept be-
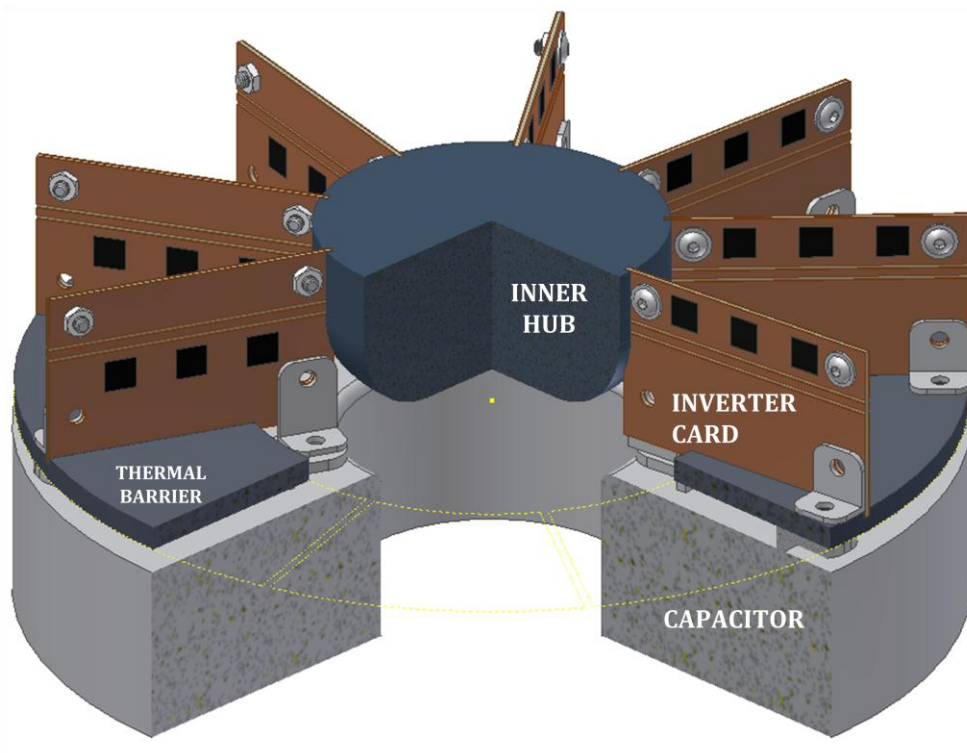
Figure 4.2 Axial inflow inverter Revision A

tween the radial inflow inverter is the configuration of the inverter card and the addition of the center hub which routes air flow around the card.

Computer models developed for numerical computations are recreated from the computer-aided drawing (CAD) concept drawings and take advantage of the radial symmetry. Since a thermal and flow solution is computed around one of nine cards, thermal models represent a $360°/9 = 40°$ sweep of the power inverter with the card in the center of the "wedge" between two symmetry planes. Since the capacitor is modeled to generate 10 W of total heat dissipation, this quantity is also divided by 9 for the purpose of the investigation. Again maintaining consistency with the radial inflow inverter studies, a solution with an airflow of $Q = 64.8$ cfm per wedge (i.e. per unit cell) was computed. The total air flow through the device is $Q_{total} = Q \times N = 583.2$ cfm).

The key results are summarized in Table 4.1 below. Also reported is the inlet to outlet area ratio difference between the radial inflow and the axial inflow concepts because this parameter affects the pressure drop and ideal blower power required that was computed. The results are also a strong function of the fillet radius of the inner hub which was the subject of a separate study before computing a solution for one unit cell. In the current model, the flow cross sectional area through the inverter relative to the inlet area is stepped down to 20% between the thermal barrier and the inner hub then 14% between the capacitor inner edge and the inner hub before air flows through the center of the

Table 4.1 Revision A results compared with radial inflow

		Radial inflow	Axial inflow	Difference
Outlet to inlet area ratio, AR	%	10.5	11.3	+8%
Pressure Drop, ΔP	Inches H$_2$O	13.6	11.8	
Ideal blower power, P_{in}	Watts	936	806	-13%
	hp	1.26	1.08	
Maximum temperature, T_{max}	°C	380	272	108°C

capacitor at an area ratio of $AR = 11\%$ with respect to the inlet area. The pressure drop, ΔP, through the device is the inlet pressure integrated over the inlet area minus the outlet pressure integrated over the outlet area, and the ideal blower power was simply computed using (4.1).

$$P_{in} = Q \times \Delta P \qquad\qquad\qquad (4.1)$$

The thermal profile of the results is given in Figure 4.3. The maximum reported temperature is a result of a total of 192 W dissipated from each unit cell of the power inverter. In Table 4.1, the maximum junction temperature was lowered by 108°C and this is significant. However, the pressure drop is reduced only by 13.8%.
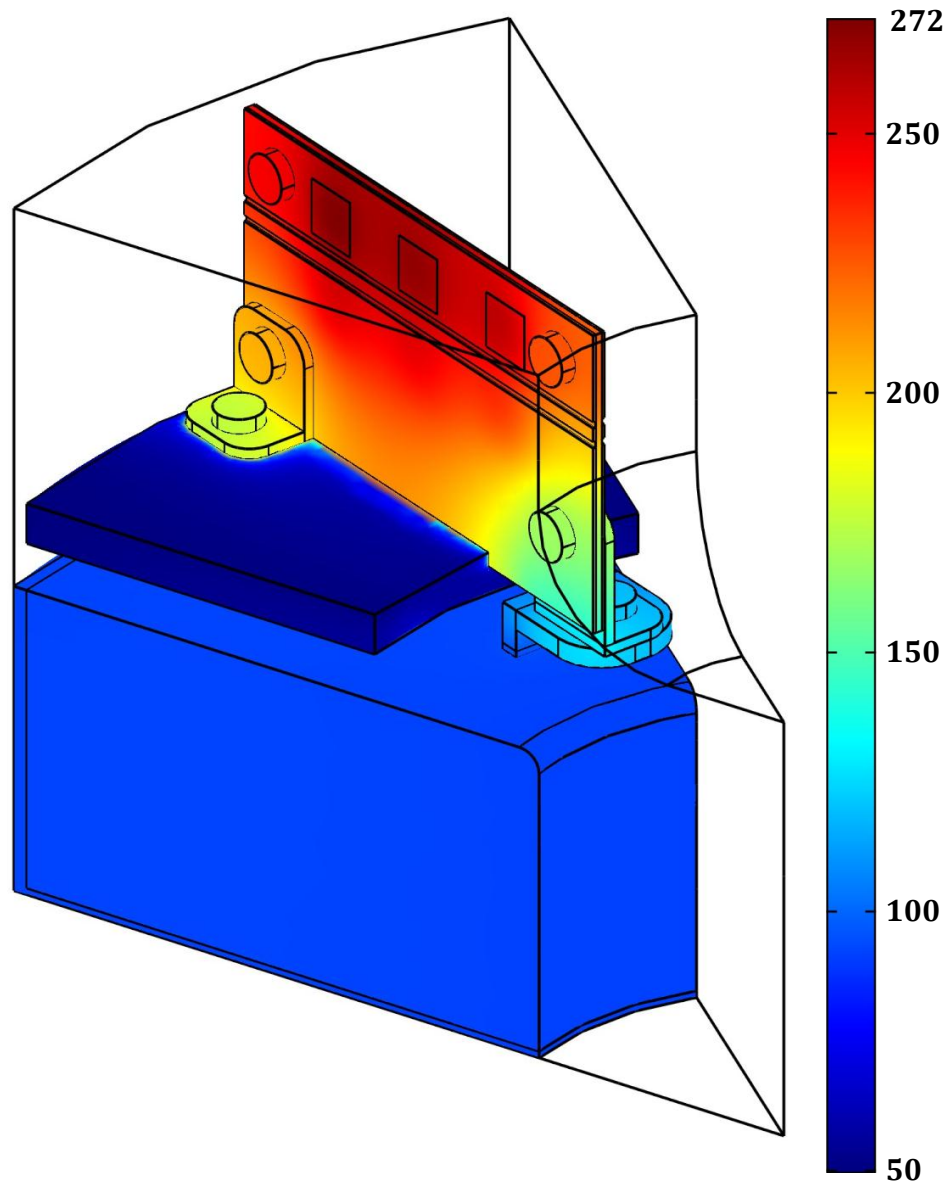
Figure 4.3 Temperature distribution of axial inflow inverter Revision A (°C) when the total heat generated is 192 W, and the unit cell air flow rate of 64.8 cfm

From these results, several improvements are quickly apparent. High pressure drop is expected at the onset with a total area reduction ratio of approximately only 11%. Furthermore, this cross-sectional flow area reduction is for the most part very abrupt at the entrance of the capacitor inner hole. Because of the relative dimensions used to compute the capacitor volume, the capacitor inner diameter can increase considerably without having a detrimental effect on the capacitor height when the volume is held constant. Increasing the capacitor inner diameter by 33% from 3 to 4 inches will increase the capacitor height by only 10% from 2.5 to 2.7 inches. Furthermore, since an air gap exists between the thermal barrier and the capacitor, a large flow recirculation zone is expected, which adversely affects the pressure drop of the system.

4.3 Major Design Features

The variables that contributed to the design process can generally be explained as either lowering the maximum device temperatures or the ideal blower power requirements. Much of the variables that are changed in order to lower device temperature were only finalized when the heat generation model was finalized. However, every geometric change made to reduce ideal blower power requirements (i.e., reduce pressure drop) contributed positively in all subsequent changes. In other words, these changes never adversely affected the temperature solutions (see the discussion of the project timeline on page 37). The general parameters that have a significant impact on the solution are summarized below.

- **Lowering device temperature**

    1. Inverter card circuitry layout

    2. Inverter card overall dimensions and thickness

    3. Inverter card materials of construction

    4. Number of power switches and Shottky diodes

    5. Use of heat transfer surface area

6. Mounting hardware materials of construction

- **Lowering ideal blower power requirements**

    1. Capacitor inner diameter

    2. Flow guidance hardware

    3. Capacitor connection tabs placement

    4. Inner hub diameter and fillet radius

    5. Roundedness of components

4.4 Flow Guidance

The results of the initial studies are further analyzed to suggest a path forward. A solution was initially computed for the same geometry but without an inverter card in the open space above the capacitor before computing the temperature distribution in Figure 4.3 above. These studies concluded that only 9.4% (1.11 inches H_2O) of the total pressure drop through the system was due to the presence of the card, giving the indication that pressure drop reduction can be pursued by other means as listed above. As previously mentioned, the large and abrupt reduction in flow area contributes significantly to the results, especially since the height of the unit is only 3.9 inches. In addition to increasing the inner diameter of the capacitor at the outlet, the area ratio can be lowered further at the inlet, which was in fact the purpose of placing an inner hub at the inlet. More inlet area can be "cut out," much like what was done with the inner hub because all of the air flowing between inverter cards is not being used to lower the device temperature. We approximate the boundary layer thickness of turbulent air flow past the inverter card using the flat plate turbulent flow solution given by [31] as

$$\delta = 0.37 x Re_x^{-1/5} \tag{4.2}$$

$$Re_x = \frac{\mu U x}{\rho} \tag{4.3}$$

where:

δ =   Velocity boundary layer thickness

Re_x =   Flow direction Reynolds number

U =   Inlet flow velocity

x =   Flow direction coordinate axis

μ =   Fluid dynamic viscosity

ρ =   Fluid density

With a card width of $W = 45$ mm in the flow direction and an inlet air flow rate not lower than $Q = 30$ cfm per unit cell, the velocity boundary layer thickness will not exceed approximately 2.5 mm in the current configuration. Applying this approximation to the radial configuration, the angle between the boundary layer thickness and the centerline of the card is only $4°$. This assumption is valid for the objective of this approximation since the angle is small. The assumption is made that the flow is turbulent at the outset for the purpose of this investigation; therefore, the relative boundary layer growth does not depend on the Prandtl number, Pr, and the thermal boundary layer thickness, δ_T, will approximately equal the velocity boundary layer thickness. That is, for turbulent flow, $\delta_T \approx \delta$ [31]. In summary, the thermal boundary layer approximately occupies a $4°$ sweep from the centerline of the inverter card outward.

The air flow cannot be segmented into individual inlet channels that are either rectangular or swept through $4°$ on each side of the inverter cards. This complex flow area would be difficult to simulate experimentally, but the cooling air can rather be guided to the space around the inverter cards, since flow from an axial fan is placed above the power inverter. Reducing the flow area from a $20°$ sweep on either side of each card to $10°$ will also increase the flow velocity in the vicinity of the card, enhancing the heat transfer characteristics.

Concept Revision DA is suggested with this thought in mind and presented in Figure 4.4 which also includes several other design changes as noted. The capacitor inner diameter is further increased, increasing the outlet to inlet area ratio to approximately $AR = 20\%$ which also increases the intermediate cross-sectional area between the inner hub and the capacitor inner edge. The surface area of the card is increased by 11%, and the chips are centrally placed on this card. The complex nature of the flow partitions is addressed Revision DB in Figure 4.5 along with other modifications as documented using the callouts in the figures.

PARTITION REDUCES
VOLUMETRIC AIR
FLOW BY 50%

INNER HUB WITH
INCREASED FILLET
RADIUS

INVERTER CARD
WITH 11% MORE
SURFACE AREA

CAPACITOR WITH
INCREASED ID TO
REDUCE FAN POWER
REQUIREMENTS

Figure 4.4 Axial inflow inverter Revision DA

REDESIGNED
INNER HUB

INVERTER
CARD GATE
CONNECTION

REDESIGNED FLOW
PARTITIONS FOR
PRACTICALITY

REDESIGNED
MOUNTING
HARDWARE

LEAKAGE PORT ALLOWS
FOR AIR FLOW UNDER
THERMAL BARRIER

MOUNTING HARDWARE
DOES NOT PROTRUDE
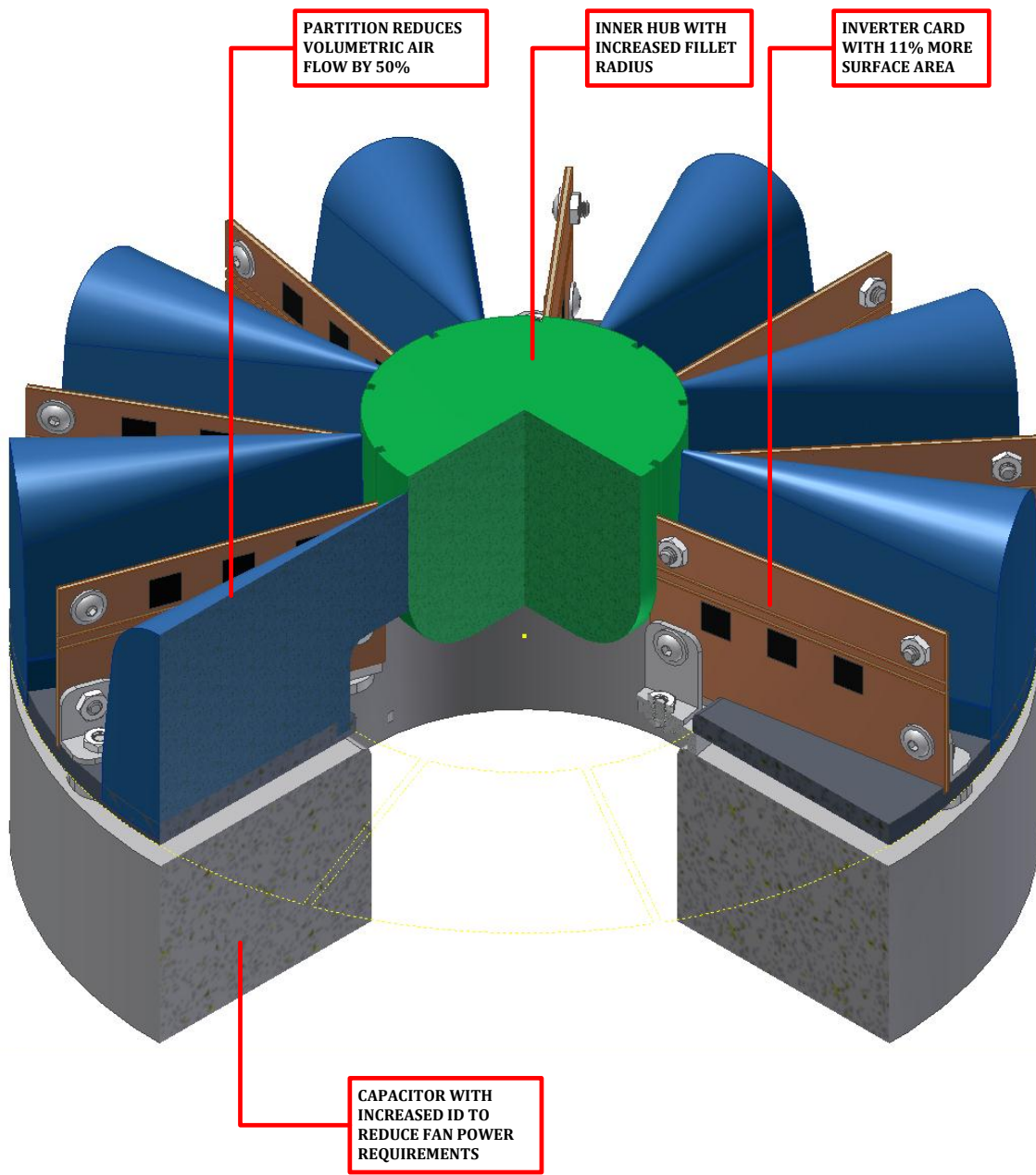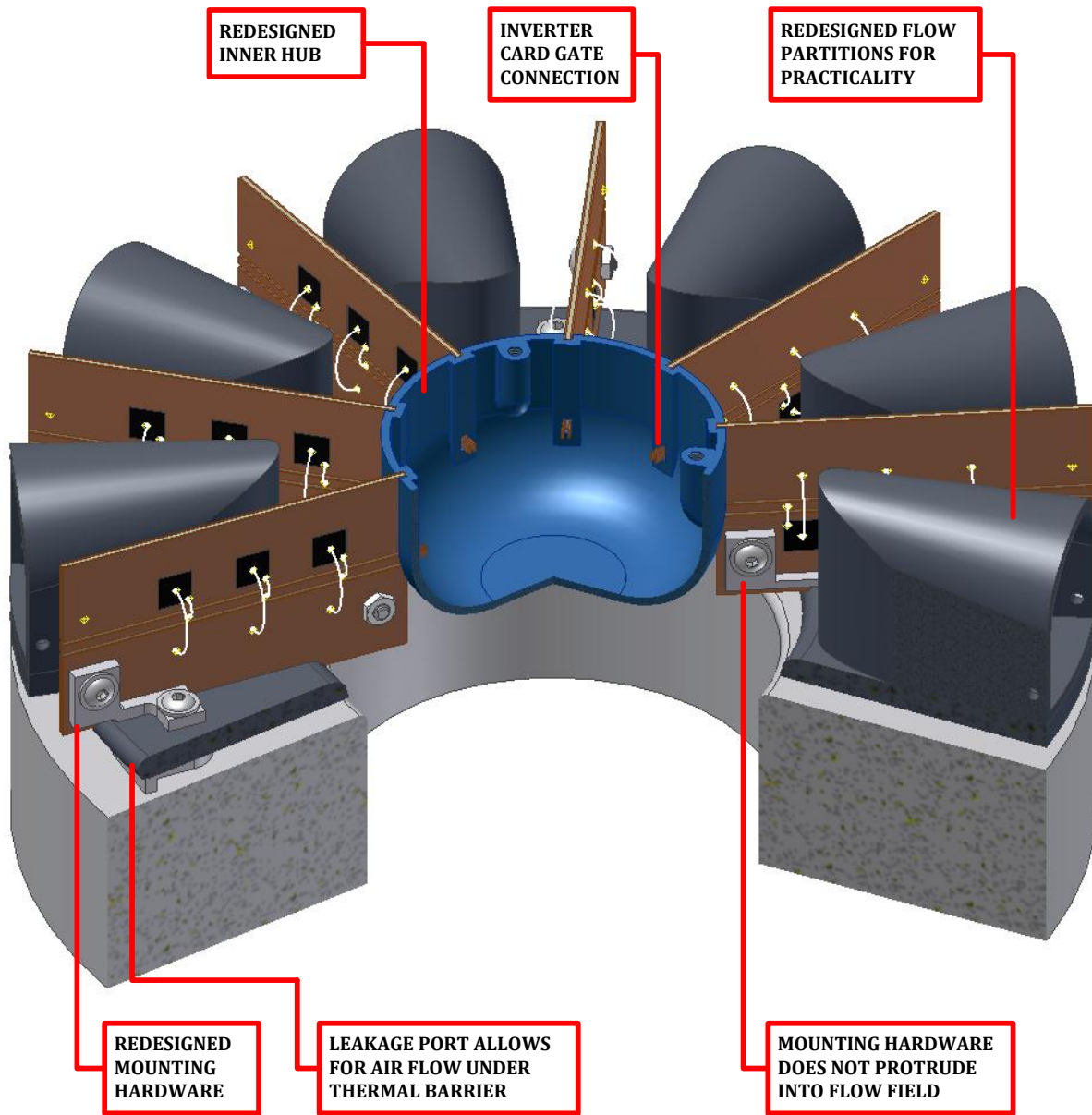INTO FLOW FIELD

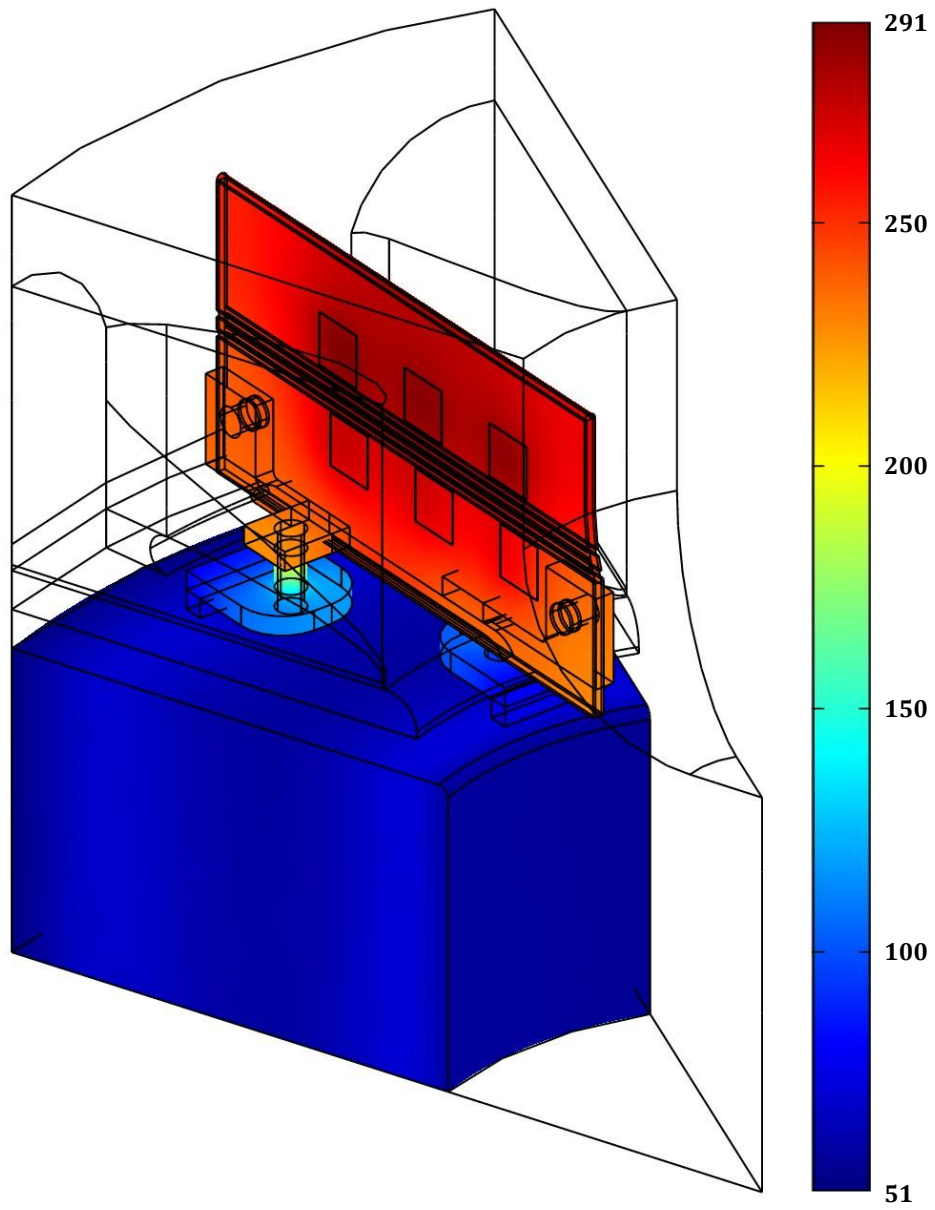Figure 4.5 Axial inflow inverter Revision DB

Figure 4.6 Thermal profile of Revision DB, °C. $Q = 64$ cfm, $\dot{q}_{MOS} = 36$ W, $\dot{q}_{diode} = 24$ W. Total heat generated per unit cell = 192 W.

Revision DB of Figure 4.5 addressed many notable shortcomings of Revision DA of Figure 4.4. As previously mentioned, electrical feasibility is also a key design aspect that must be demonstrated. Thus, the inner-connectivity of the inverter was requested as well as connections to other auxiliary electrical systems. The flow partitions in Revision DA were approximately 20% higher than the inverter cards with the idea that air flow acceleration is ideally achieved upstream of the inverter cards. However, this benefit was not worth the additional total height and volume of the power inverter. The flow partitions in Revision DB have been redesigned for manufacturability and utilize a simpler approach. The external packaging is simplified since the height is now flush with the inverter cards. The space inside the inner hub and the flow partitions is utilized to house a gate driver that will modulate the switching sequence of the MOSFET power switches and current sensors can be housed inside the flow partitions, improving the electrical feasibility of the this concept. A flow solution was modeled for Revision DB. The inlet velocity of this analysis was 6.42 meters per second ($Q = 61$ cfm per unit cell) and the velocity accelerates to approximately 20 meters per second in the vicinity of an inverter card because of the flow guidance. *The analysis predicted a pressure drop of 5.7 inches H_2O across the inverter which is a reduction of 52% from the initial concept.*

The thermal plot of Revision DB is shown in Figure 4.6 with a maximum device temperature of 291°C. The mounting hardware is modeled as stainless steel which is most practical and a good choice considering that the low thermal conductivity of stainless steel minimizes heat conduction to the capacitor. The size of the mounting bolts has proven to be sufficient, and the maximum temperature in the capacitor as a result is 73°C, which is below the maximum operational temperature of 100°C. The DBC card construction is chosen as before and the chips are repositioned and more spread out on the card surface in order to dissipate the heat more uniformly and avoid unnecessary hot spots. The partitions are modeled as insulating material along with the thermal barrier. However, with the high temperatures computed, these components can be used as additional heat transfer surfaces in future models given that the temperature of the capacitor remains low.

50

4.5 Mounting Hardware

The mounting hardware was completely redesigned in order to accommodate the complex flow path. Figure 4.7 demonstrates one of the key differences between previous concepts and Revision DB. An abrupt reduction in flow area causes a pressure spike of approximately 350 Pa. With the addition of a leakage flow path behind the thermal barrier, this pressure spike is prevented because the flow area is essentially opened up not only by means already discussed but now at the outer diameter of the thermal barrier. Figure 4.7 reveals that the maximum pressure in 2D axisymmetric models was reduced by 6.2% as a result of this change. The leakage path also allows the capacitor to be cooled on one additional surface. The results of previous concepts indicated that the thermal barrier maintained a temperature of close to 50° when the capacitor and inverter card increased in temperature, prompting the allowance of the leakage path to open up. Essentially, the capacitor temperature is not expected to increase as a result of the increase in air temperature at that location.

Observe that another key difference with the capacitor mounting hardware is marked between Revisions DA and DB. We can expect flow recirculation with capacitor tabs that are protruding into
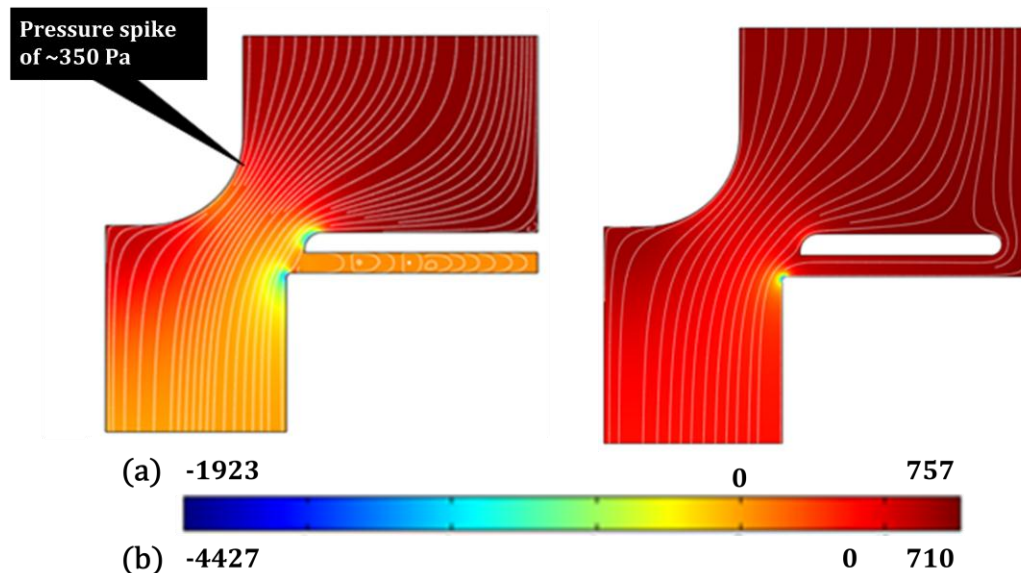
Figure 4.7 2D axisymmetric pressure profile, Pa, subject to an inlet flow velocity of 6.4 m/s: (a) without rear leakage port and (b) with rear leakage port

the flow field. With the mounting hardware redesigned, the capacitor tabs are placed underneath the thermal barrier to open up the flow path in the reduced space. Because of the introduction of the leakage port at the outer edge of the capacitor, the mounting bracket at the outer radius of the capacitor is also redesigned to accommodate air flow in the downward direction (see comments on Figure 4.5, page 48).

The capacitor tabs were repositioned four times, and Figure 4.8 illustrates the design process with respect to the position of these tabs. Depicted is a top view of a 40° sweep of the capacitor from the outer diameter at the top of the figure to the center point of the inverter at the bottom of the figure. The inverter card is placed above the vertical centerline in the figure. Figure 4.8 (a) indicates that the area ratio of the first capacitor was approximately 11% which did not cause the capacitor tabs to protrude outwards into the flow field. The card dimensions were increased in succeeding iterations, causing the mounting hardware to be repositioned in order to accommodate this change. The new position of the capacitor tabs affected the flow field characteristics because the capacitor inner diameter was also increased. As a result, the capacitor tabs were then repositioned underneath the thermal barrier at the time when a rear air leakage path was also introduced as described above. Figure 4.8 (c) also shows the approximate air flow path below the thermal barrier given the position of the tabs. In succeeding design iterations, the capacitor tabs are repositioned once more and out of the way of the air flow path as in Figure 4.8 (d). The final position of the capacitor tabs is the most standard and simplest approach, and is consistent with the original design of the power rings from SBElectronics® (see Figure 3.4 on 21).
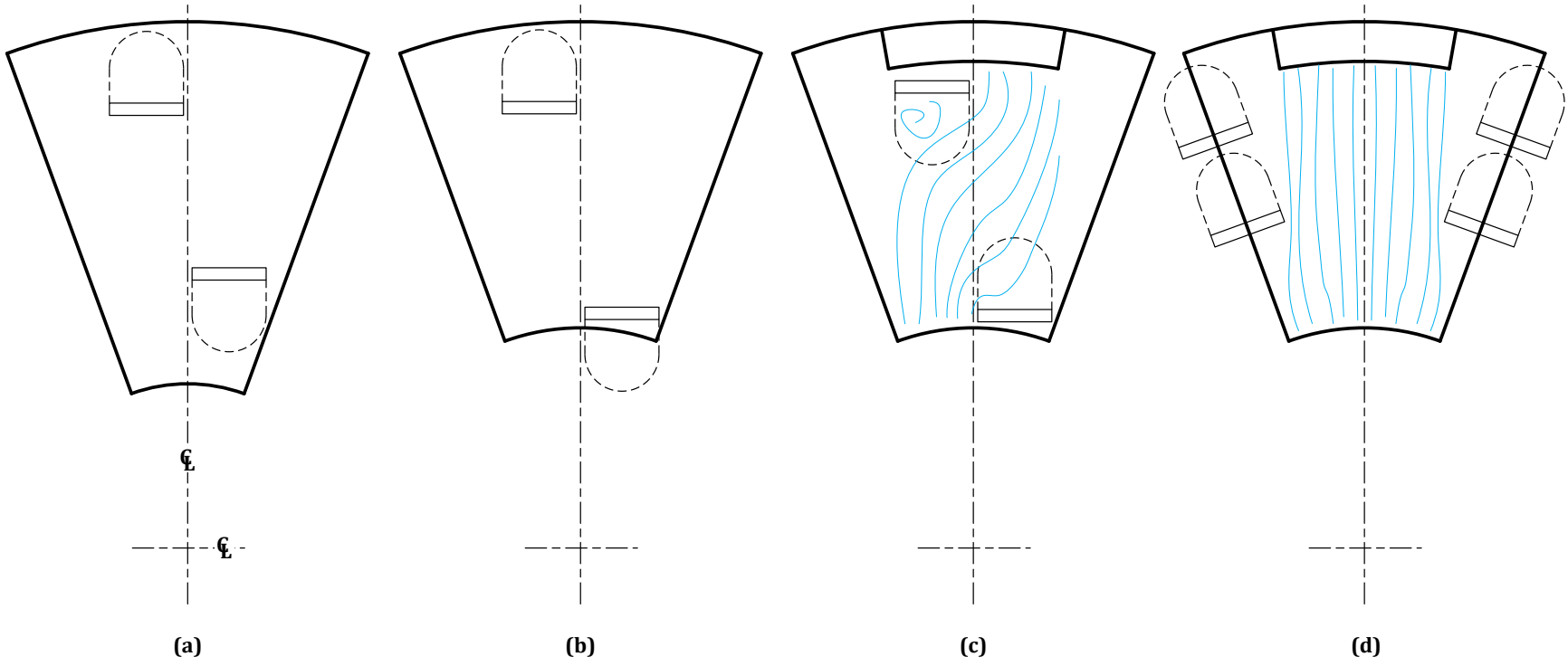
Figure 4.8 Capacitor tabs design evolution

(a)   (b)   (c)   (d)

53

4.6 Air Flow Between Fins

With the implementation of the heat generation model of (3.4) through (3.8) which was made available during the final months of the study, the head load increased nearly one to one and a half times in the MOSFET power switches and nearly three to four times in the diodes. The current design concept incorporating a direct-cooled substrate was pushed to the limit and a more prudent approach was to investigate the use of fins to increase the heat transfer surface area to more effectively cool the inverter cards. The tradeoff of incorporating fins in the design concept is the increased modeling complexity as well as the cost of ideal blower input. Two concepts that were investigated are depicted in Figure 4.9, which shows a top view of the axial inflow inverter. The first concept in Figure 4.9 (a) incorporates concentric rings that could be a part of the top housing and be fitted to the shape of each of the cards and the flow partitions. The second concept in Figure 4.9 (b) utilizes a "modularized" approach for which each inverter card has its own finned structure.

The finned structure in both of these concepts cannot extend the length of the inverter card

(a)   **(b)**
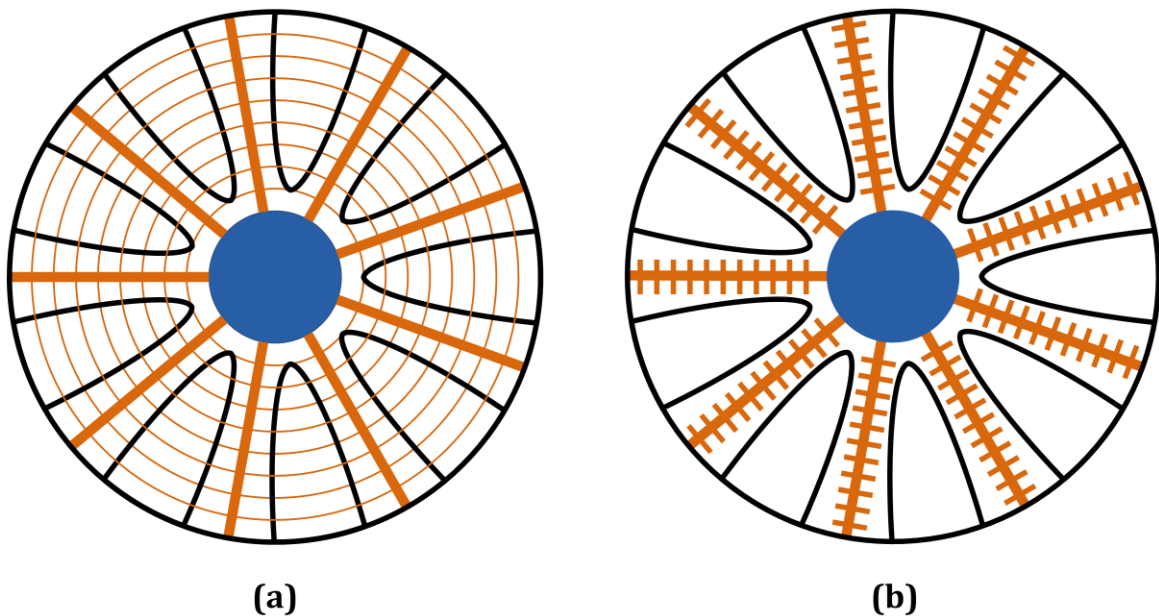
Figure 4.9 Fin design concepts (a) concentric rings and (b) modularized

since the air flow turns 90° inward at the capacitor and should be avoided. The height is chosen from general 2D-axisymmetric studies that investigated the impact of the flow-direction length of the fins on the pressure drop as a result of this 90° turn. From these studies, the height in the flow direction is not to exceed approximately 60% of the flow volume above the thermal barrier or 25 mm measured downward from the top of the inverter card in this case. The fin spacing is uniform in both concepts because air flow will take the path of least resistance if the spacing is non-uniform. In light of this, the fins must extend as much as possible in the direction perpendicular to each inverter card to prevent air from flowing around instead of through the fins.

The first concept utilizing concentric rings takes advantage of all possible surface area and also opens up the possibility of heat conduction to the flow partitions which then can be made of a conducting material for even more heat transfer surface area. However, the concept is simply too complex because each ring would have to be machined to fit the shape of the flow partitions and the inverter cards. Furthermore, the rings would need to be made from an exotic material that is a good heat conductor yet an electrical insulator such as AlN. A modularized approach has advantages over concentric rings with regards to simplicity, manufacturability, and maintaining electrical feasibility.

Scofield et al. [11] presented the development of a modularized inverter with a finned structure that is used as a benchmark model and a guideline from which to size the fins. They used the finite element method to study thermal management of a system that dissipated 100 W per MOSFET and 50 W per diode which is roughly opposite of the heat load expected according to the heat generation model used in this study. The heat-generating devices are mounted to a DBC substrate that is housed in a structure made of Torlon® (an insulating material). A set of fins are mounted to the backside of the DBC structure and protrude out of the housing on one side. The top enclosure is not utilized for carrying away heat from the module. The dimensions of the fins are varied and studied parametrically. The results of their work are reproduced in Figure 4.10 and Table 4.2.
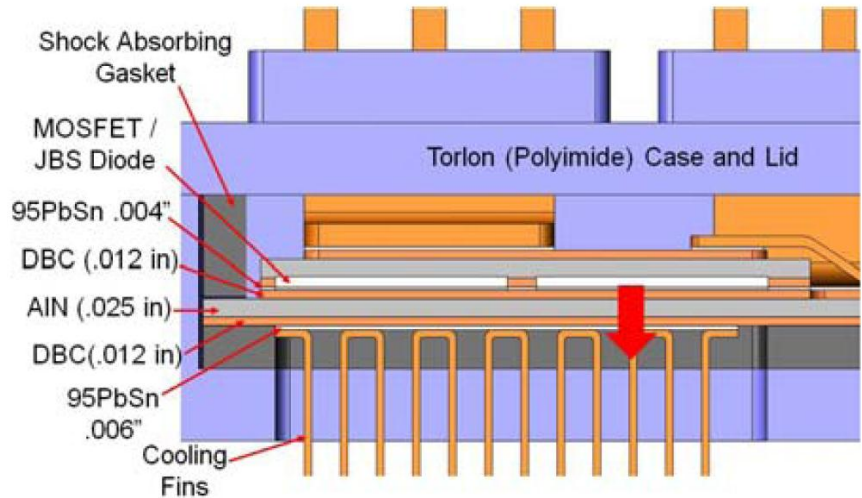
Figure 4.10 "Cross-sectional view of Gen-II design" [11]

Table 4.2 "Thermal modeling results for Gen II module designs with AlN substrates
and various Cu fin arrangements. Inlet air flow = 2500 ft/min, MOSFET heat
generation = 100 W" [11]

Fin thickness 10^{-3} in.	Fin spacing 10^{-3} in.	Fin height in.	Total fin area in.^{2}	Inlet air flow volume per module cfm	Peak MOSFET Junction Temp Rise °C
8	26	0.5	40.3	5.9	166
10	32	0.5	33.3	5.8	172
20	52	0.5	22.4	5.2	178
8	40	1	58.1	13.1	156
10	45	1	51	12.2	155
20	52	1	40.3	11	138

In the present study, the inverter card of Revision DB would essentially need to be flipped inside out. Since heat-generating devices are on both sides of the DBC structure in previous concepts, both inner walls of an enclosed structure would need to carry heat-generating devices. The basic inverter card module would have a symmetric profile as illustrated in Figure 4.9 (b). Enclosing the MOSFETs and diodes makes the module much more electrically feasible because the entire housing will be filled with silicone gel to prevent dielectric breakdown. The overall thickness would grow from 1.8 mm to more than 6 mm considering the space needed for interconnectivity of components. Instead of using DBC in a Torlon® housing, CTE mismatch can be significantly reduced by changing the materials of the inverter card in successive design concepts to direct-bonded aluminum (DBA) and the housing is to be made of aluminum as well. The entire housing can be used for a heat transfer conduction and surface area and the fins are then extruded directly from the housing instead of protruding from the inverter card.

The important parameters to understand as to how the presence of fins impacts the flow solution are the wetted perimeter, $\wp$, channel area, A_{ch}, and the friction factor, f. Figure 4.11 is a functional schematic of the flow field through each fin from which the dimensions used to calculate $\wp$ and A_{ch} are defined. The length from the fin tip to the partition surface, x_2, will vary for two reasons. Moving from the capacitor outer diameter inwards, the edge of the flow partitions begins tangential to the radial coordinate direction and end radially inwards.

The relationships in equations (4.6) through (4.10) are used to determine the impact of the presence of fins on the flow solution for which the Reynolds number, Re_{D_h}, for each fin is calculated based on the hydraulic diameter, D_h [37]. The friction factor, f, is plotted for each given Reynolds number, showing Re_{D_h}, on the Moody diagram in Figure 4.12 [38]. This information is used to calculate the resultant additional pressure drop, ΔP, plotted in Figure 4.13 when $N_{fins} = 60$.

The applicable equations are given below.

$$\wp = 2x_1 + 2y_2 \tag{4.4}$$

$$A_{ch} = x_1 y_1 + x_2 y_2 \tag{4.5}$$

where:

x_1 = Fin height perpendicular to the card

x_2 = Distance between the fin tip and the flow partition

y_1 = Distance between fins

y_2 = Fin pitch

$$D_h = \frac{4A_{ch}}{\wp} \tag{4.6}$$

$$Re_{D_h} = \frac{UD_h}{\nu} \tag{4.7}$$

$$\frac{1}{f^{1/2}} = 2.0 \log\left(0.64 Re_{D_h} f^{1/2}\right) - 0.8 \tag{4.8}$$
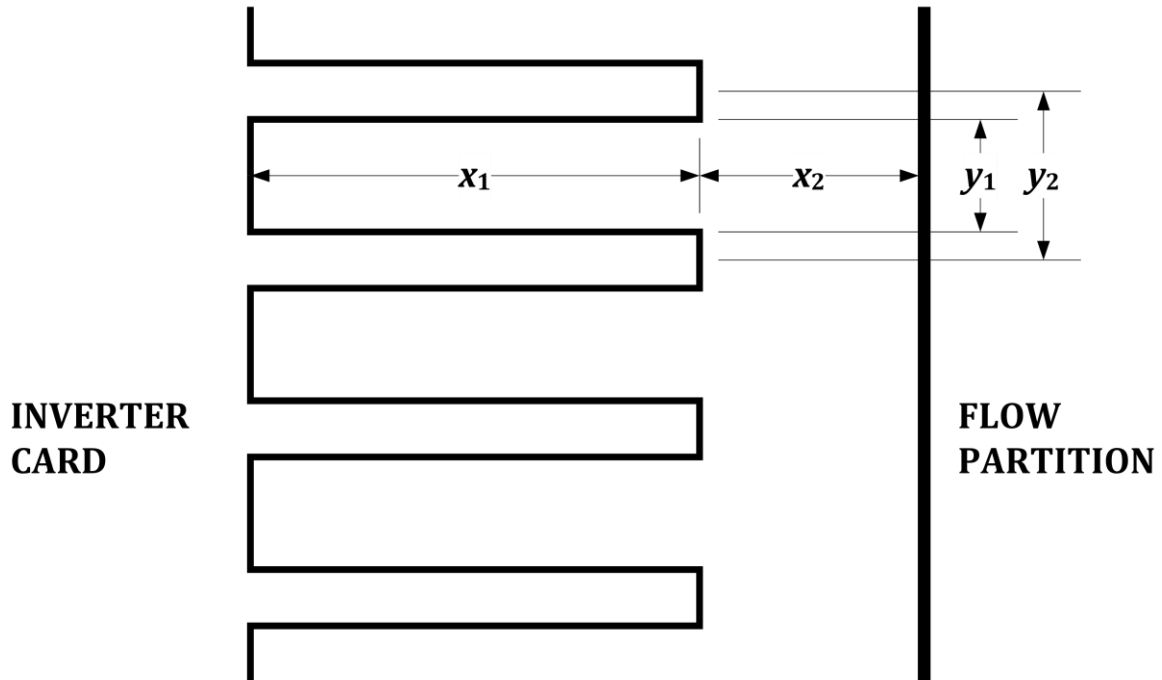
Figure 4.11 Fin dimensions for ΔP calculations

58

$$h_f = f \frac{L}{D_h} \frac{U^2}{2g}$$ (4.9)

$$\Delta P = \rho g h_f$$ (4.10)

A low Reynolds number will yield lower pressure drop through the fins but a higher air flow velocity will increase the heat transferred to the bulk fluid. Decreasing the Reynolds number without decreasing the velocity can be accomplished by decreasing the channel cross-sectional area. The heat transfer surface area is maximum between the fins and the flow partitions when $\wp$ is less than or equal to the perimeter of A_{ch}. Thus, decreasing A_{ch} without decreasing $\wp$ will decrease the Reynolds number and thus the pressure drop through each set of fins without decreasing the heat transfer performance. This can be done by carefully minimizing the length between the fins and the flow partitions. The flow through the fins plotted on the Moody diagram takes into account an approximate length of $x_2 = 2.09$ mm from the fin tip to the partition surface.
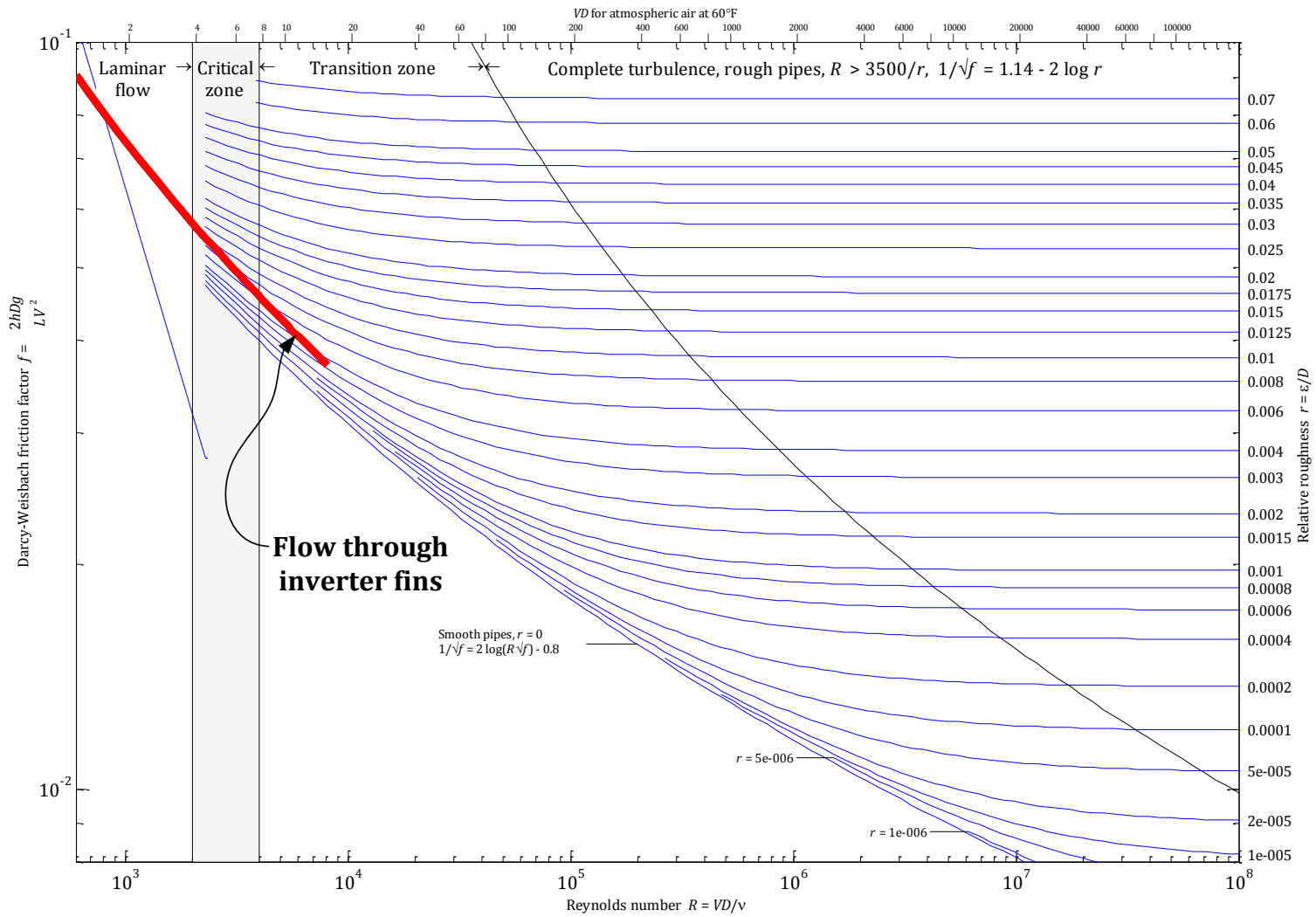
Figure 4.12 Moody diagram showing flow through inverter fins

60
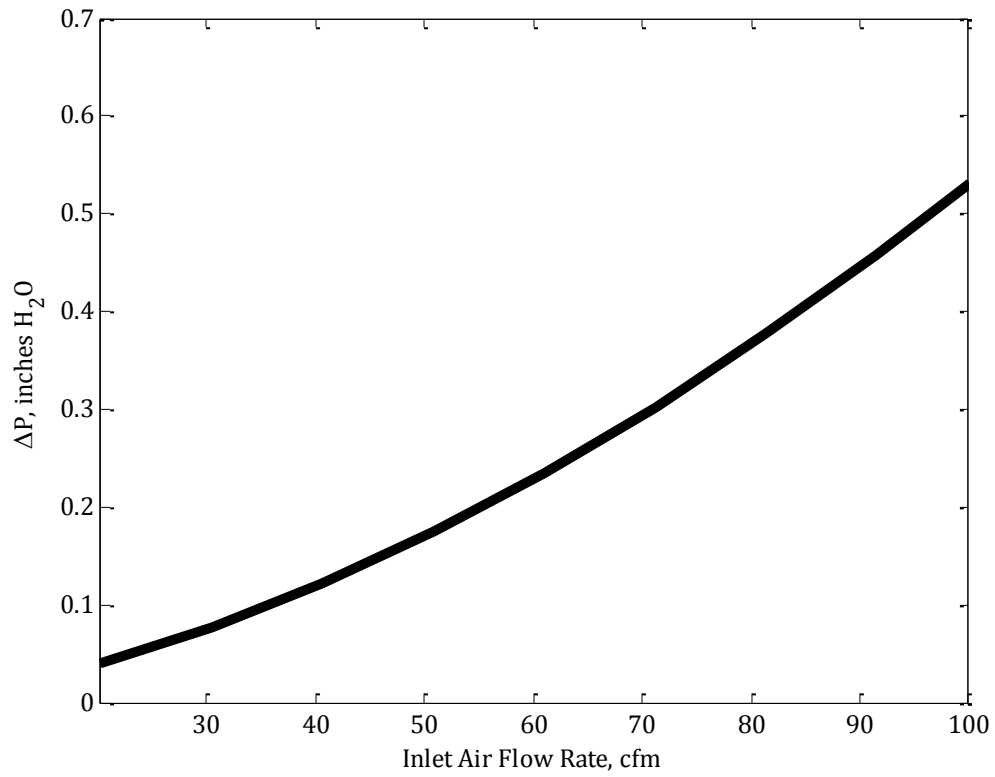
Figure 4.13 Additional pressure drop due to fins, $N_{fins} = 60$

4.7 Summary of Results

Since the FY09 design had unacceptably high pressure drop and blower power requirements, the early stages of the present study was focused on reducing them. The pressure drop predicted by the finite element models was 11.8 in. H_2O for Rev. A, an 11% improvement over the radial inflow configuration results, and only 1.11 of 11.8 in. H_2O (9.4%) of the pressure drop was due to the presence of the card. The original major contributor to high ideal blower power input required to cool the inverter was due to the fact that the flow area was reduced by 90% through the inverter. That is, for Rev. A, $A_{out}/A_{in} \cong 10\%$, which is a major contributor to the 11.8 in. H_2O of pressure drop. In the current design configuration, $A_{out}/A_{in} \cong 19\%$. This increase will reduce pressure still further. Additionally, when flow guides were first introduced at the time of Rev. D, the results predicted a pressure drop of 5.7 in. H_2O across the inverter which represented a 49% reduction in pressure drop across the inverter from previous design revisions. The addition of flow partitions is a significant contributor to this reduction. Revisions A through D were modeled using conservative heat generation estimates for each of the components, and a maximum temperature of approximately 290°C was computed. Rev. F was the first design revision after a significant increase in heat generation was expected, and cooling fins were added which increased the predicted ΔP to 6.4 in. H_2O. A major difference between Rev. F and the final design Rev. G is that the capacitor tabs were repositioned 20° radially and out of the main flow path to reduce the pressure drop further. Table 4.3 and Table 4.4 below summarize the above discussion of the pressure drop results in tabular form and the revision history that is also illustrated on the timeline of Figure 4.1, respectively.

The final configuration, Revision G, yields a pressure drop of 6.4 in. H_2O for an inlet flow rate of 60 cfm per unit cell, and the associated results are discussed in Section 5.3 Flow Characteristics – Results of Parametric Study.

Table 4.3 Influence of configuration changes on the pressure drop

Rev.	Major Design features	ΔP (in. H$_2$O)
A	$A_{out}/A_{in} = 10\%$	11.8
D	Flow partitions are incorporated. Capacitor tabs are repositioned. Leakage path is at outer radius.	5.7
F	Fins are added for heat transfer.	6.4

Table 4.4 Summary of revision history

Rev.	Primary Features and Major Changes
A	Compares readily to the radial inflow inverter design
B	The chips are spread evenly across an elongated inverter card. The capacitor inner diameter and the radius of the center hub are enlarged.
C	More of the leading edge of the inverter card is exposed to incoming cooling air by making the card symmetric in the axial inflow direction.
D	Flow guide partitions are incorporated and the insulating material has a leakage port at the outer radius of the capacitor. The capacitor tabs are reconfigured to not be protruding into the flow field in order to lower pressure drop through the system.

Table 4.4, continued.

Rev.	Primary Features and Major Changes
E	In light of experimental data suggesting a significant increase in the heat generated, a design is presented that shows twice as many cards in order to reduce the current and voltage supplied to each diode and MOSFET. Flow or temperature profiles are not calculated for this revision.
F	The card is flipped inside out in order to house a finned structure because of the increased heat load based on experimental data. Flow guides are incorporated to reduce pressure drop, and the capacitor inner diameter is increased.
G	More fins are incorporated in the design, the flow guides, center hub, and mounting structure serve a new purpose of carrying away heat from the card, a capacitor bus structure is introduced, and the device is much more electrically feasible and realistic.
GB	Insulating material is replaced with aluminum and aluminum nitride where possible and the MOSFET and diode positions are re-ordered in order to reduce device temperatures.

Chapter 5.   Final Results

5.1 Overview

Revision GB is the final axial inflow inverter concept for which thermal feasibility is established. A discussion on the basic functionality of the latest power inverter concept including the improvements of the system over Revision GA precedes a presentation of the details that are critical to performance. The un-scaled functional diagrams of Revision GA and GB are given in Figure 5.1 and Figure 5.2, respectively.

The most notable difference of Revision G is that the inverter card is essentially flipped inside out from previous concepts. Figure 5.1 and Figure 5.2 show two halves of an inverter card. Each half consists of heat-generating SiC MOSFET power switches and Shottky diodes that are mounted to the top of a direct-bond aluminum (DBA) structure. These two halves of the inverter card are housed inside an aluminum structure to which thirty cooling fins are mounted on each side. The cooling fins interact with the cooling air that flows from above the inverter cards. The top of the DBA structure is segmented to connect to the capacitor on the lower half, a gate driver in the middle, and the external phase connection on the upper half. Current flows from the positive terminal of the capacitor to the positive terminal of the inverter card. Alternating current is generated by the power inverter in the top of the card which connects to external systems. Direct current flows from the top half of the inverter card to the negative terminal of the card and continues to the negative terminal of the capacitor.

The second most notable difference is the manner in which the capacitor positive and negative terminals connect to the corresponding terminals of the inverter cards and is the first notable difference of Revision GB over Revision GA. The capacitor tabs no longer connect directly to each side of the inverter card but electric current instead flows through a capacitor bus which consists of a posi-

tive and negative layer separated by an aluminum nitride electrical isolator. The male and female connectivity of the capacitor bus and the inverter cards was reversed in Revision GB in order to address manufacturability concerns. The capacitor bus is given structural rigidity since it is bolted to the thermal barrier. The mounting bolts are placed inside the flow partitions in Revision GB since the previous location of the bolts in Revision GA below the fins does not allow for fastening tools to reach the bolts without difficulty.

Revision GB improves the heat transfer, structural, and electrical characteristics of the power inverter concept over Revision GA by changing the thermal barrier and flow partition material from Cotronics® Ceramic 914 to aluminum. This change is made possible since the capacitor bus negative terminal is on the top and since 100°C was not exceeded in the capacitor in the investigation of previous concepts. The negative terminal of the capacitor now interacts with the entire device and effectively grounds the system, which improves the control of live phase connections. Changing the functionality of these components from thermal insulators to thermal conductors significantly increases the heat transfer surface area. Heat flows from the inverter cards to the capacitor bus previously via the positive and negative terminals of each half of the inverter card. In the latest concept, the heat conducted through the inverter card positive and negative terminals is less restrictively spread out to multiple surfaces and not just the underside of the capacitor bus positive terminal. This material change also applied to the inner hub of the power inverter, which is not shown in the figures. Changing the inner hub to a heat-conducting material improves the thermal characteristics toward the center of the power inverter.
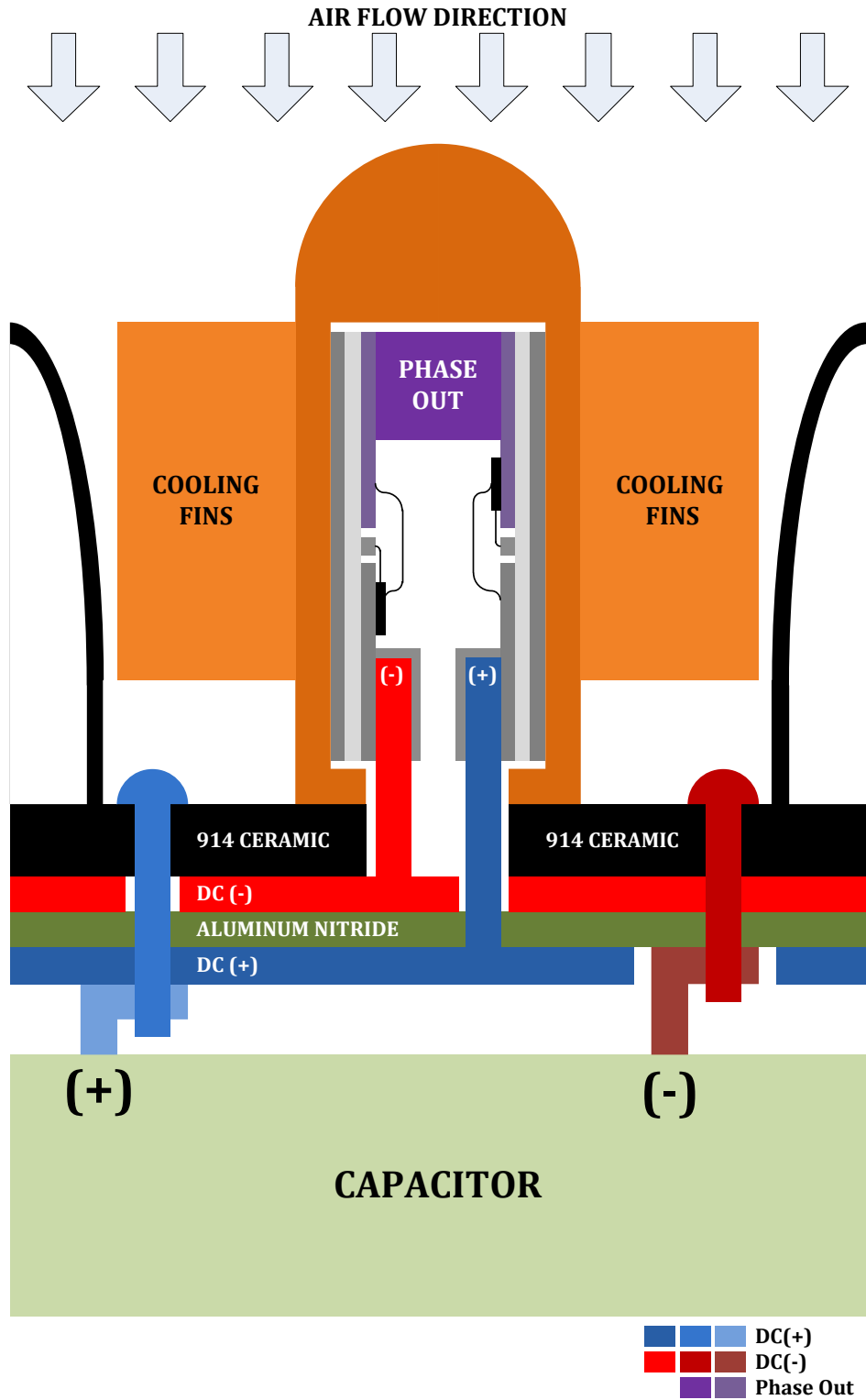
Figure 5.1 Functional schematic of power inverter concept, Revision GA

AIR FLOW DIRECTION

PHASE OUT

COOLING FINS

COOLING FINS

(-) (+)

ALUMINUM

ALUMINUM
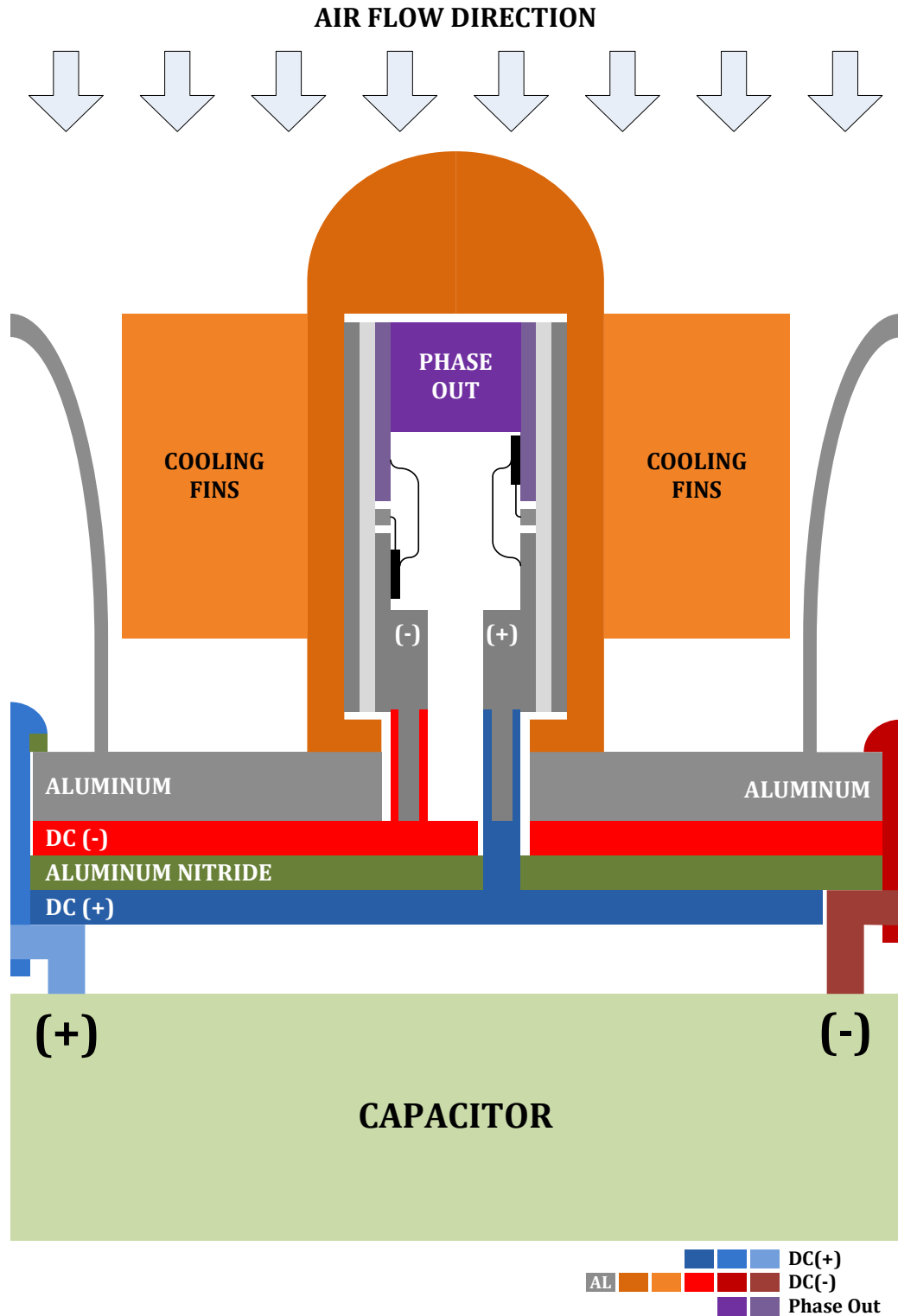
DC (-)

ALUMINUM NITRIDE

DC (+)

(+)

(-)

CAPACITOR

DC(+)
AL DC(-)
Phase Out

Figure 5.2 Functional schematic of power inverter concept, Revision GB

5.2 Detailed Description of the Final Concept

A cut-away view and an exploded view of the power inverter concept Revision GB is given in Figure 5.3 and Figure 5.4, respectively. The outer diameter and height are 9.4 in. (239 mm) and 4.5 in. (115 mm), respectively, and the total volume of the device is 313 cubic inches (5.1 liters). The exit diameter at the bottom of the inverter is 4 in. (100 mm), which is also the inner diameter of the cylindrical capacitor. Although the concept is presented in varying colors for clarity, most of the device is made from aluminum as previously discussed.

The most prominent distinction of the latest concept from previous concepts from Figure 5.3 and Figure 5.4 is that the concept includes external packaging with external system mounting considerations in place. This external frame is completed with a top enclosure lid which is made up of a metal mesh screen to which the inner hub is mounted. The second-most prominent feature of the latest concept is that the entire device is assembled from the bottom up as demonstrated in Figure 5.4. Each inverter card module is held in place by fitting into grooves on three sides of each module, and the top enclosure that fastens to the housing is against each inverter card module on the top (fourth) side. As before, three inverter cards per three phase legs (9 total cards) are included in the final assembly, and one external connection serves each phase. Each inverter card module is exactly the same even though the location with respect to the external phase connection may be different for three cards. The three external phase connections protrude outwards at 120° apart from one another, and one set of external gate driver connections that protrude out of each inverter card can be found inside the inner hub where the gate driver is to be housed. The inner-connectivity between inverter cards and the phase connection to external systems consist of simple aluminum components that line the inverter housing and connect cards behind the flow partitions are depicted in Figure 5.5.

INTERNAL PHASE
CONNECTION
ACROSS 3 CARDS

INTERNAL GATE
CONNECTIONS

TOP SCREEN WITH
EXTERNAL FAN
MOUNTING HOLES

EXTERNAL PHASE
CONNECTION

4.5 inches
(114.7 mm)

3.94 inches (100 mm)

9.41 inches (239 mm)

OUTER CASING
WITH 4 MOUNTING
HOLES SIZED FOR
M10 BOLTS

INTERNAL DC
CONNECTIONS IN
PARTITION SPACE

OUTER CASING
THICKNESS: 4.5mm

CARD CONNECTION
TO CAPACITOR
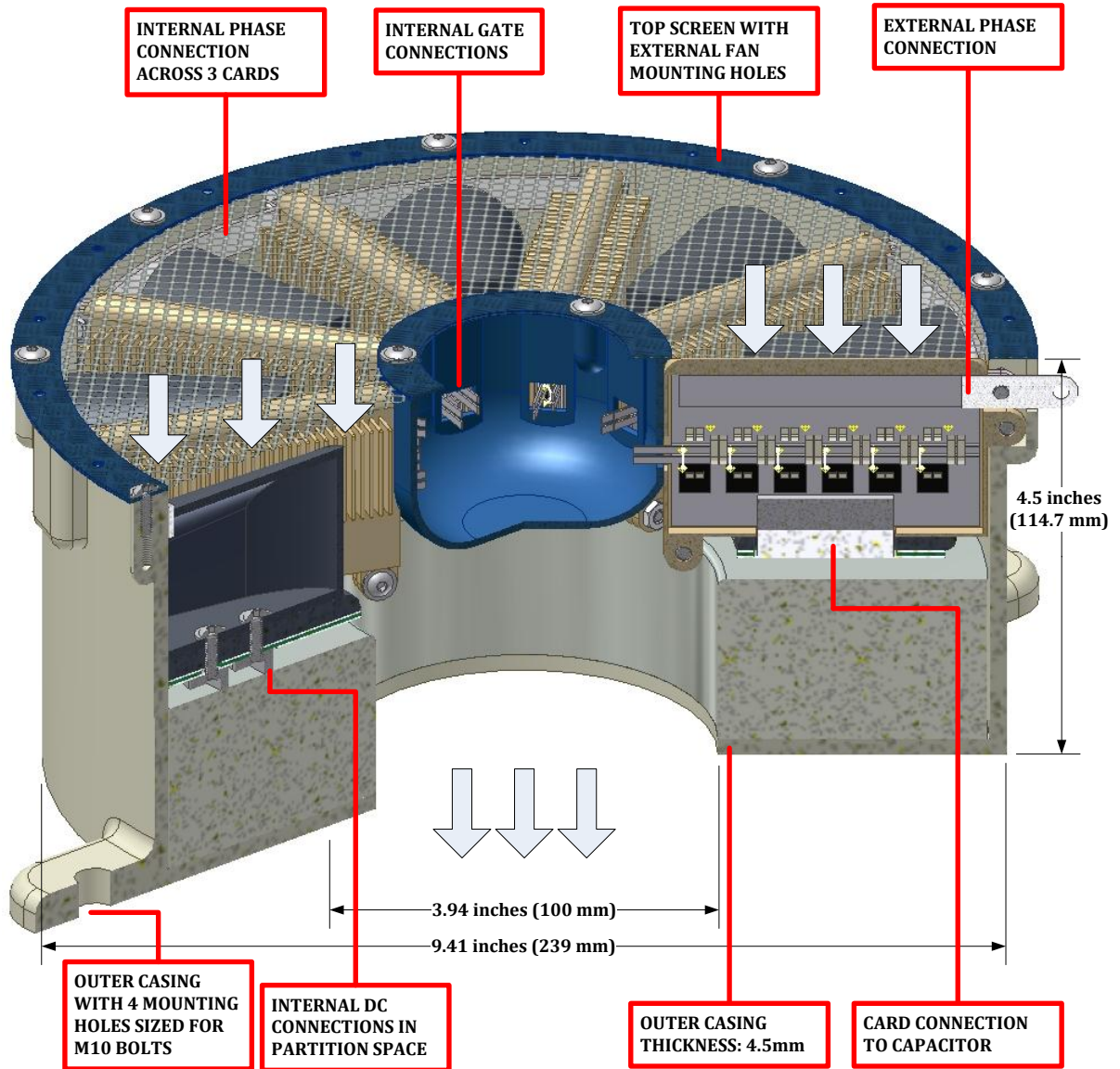
Figure 5.3 Cut away view of the final axial inflow inverter concept, Revision GB

FAN
MOUNT

INVERTER
CARDS

FLOW
GUIDES

CAPACITOR

INVERTER
HOUSING

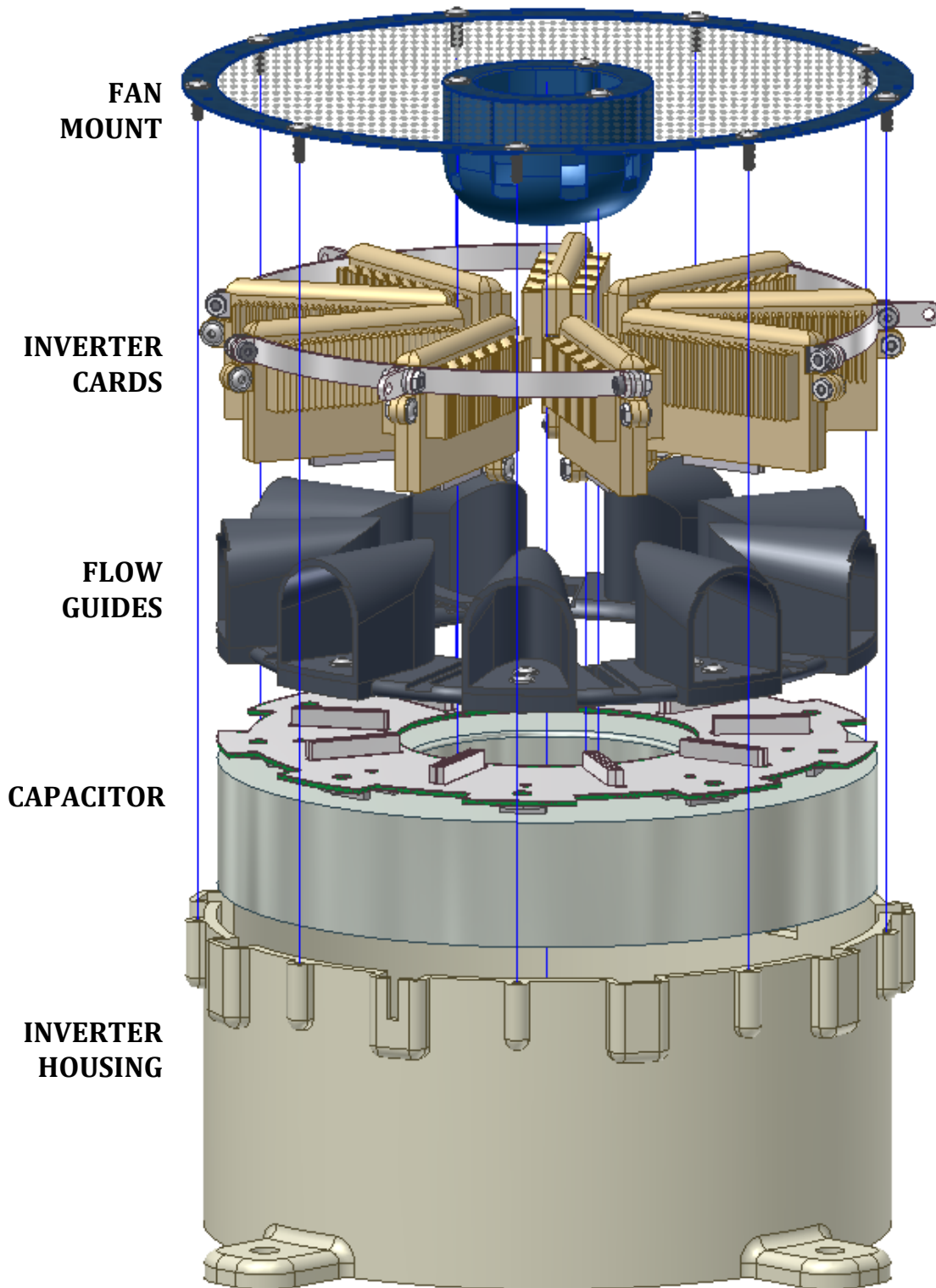Figure 5.4 Exploded view the final axial inflow inverter concept, Revision GB

71
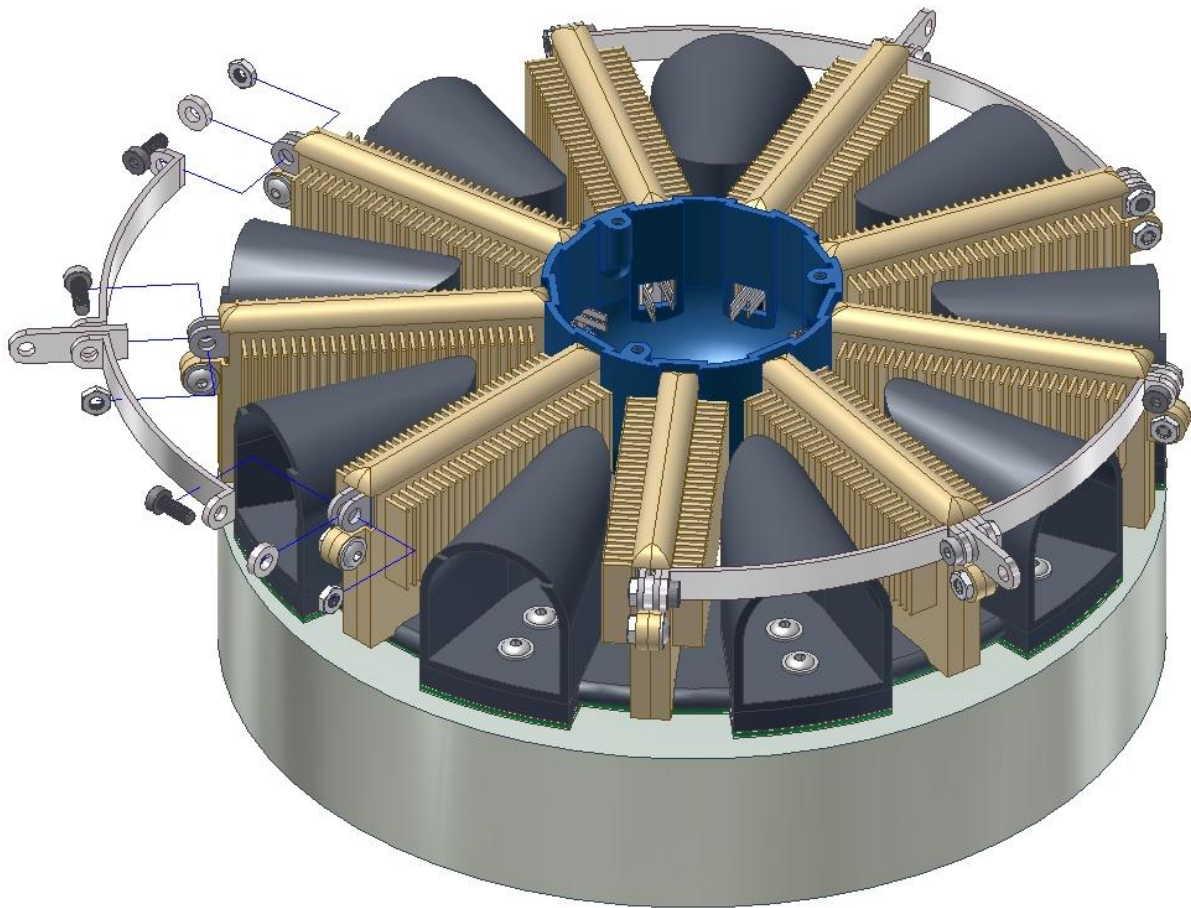
Figure 5.5 Exploded view showing internal and external phase connectivity

Figure 5.6 shows the inverter card opened up, Figure 5.7 show the connectivity between the inverter card and the capacitor, and Figure 5.8 gives further details of the card. The inverter card module is held together by two sets of fasteners that are located in opposite corners. The three power switches and three diodes are alternately mounted to the DBA structure, as shown in Figure 5.6. The ribbon bonds connect the devices to the opposite half of the card and the wire bonds connect the devices to the gate driver to be housed in the inner hub. Also shown is the gate connections which protrude out of the side of the card that is against the inner hub and the phase connection that protrudes out of the side that is against the inverter housing. A 1-mm gap exists between the perimeter of the card and the housing to account for thermal expansion.

Figure 5.8 shows the critical dimensions of the internal components from which the total card thickness is based on and illustrates the alternate mounting of the power switches and diodes that are critically placed to allow room for the ribbon and wire connections between the devices and the aluminum substrate and to prevent electrical arching. The entire inverter card cavity is to be filled with Silicone gel [36] to prevent this arching and to also prevent dielectric breakdown, and thus maintain the integrity of the components. The dimensions of the ribbon bonds that contribute to the total thickness of the card were determined by measuring the height of a ribbon bond on a benchmark model inverter card.
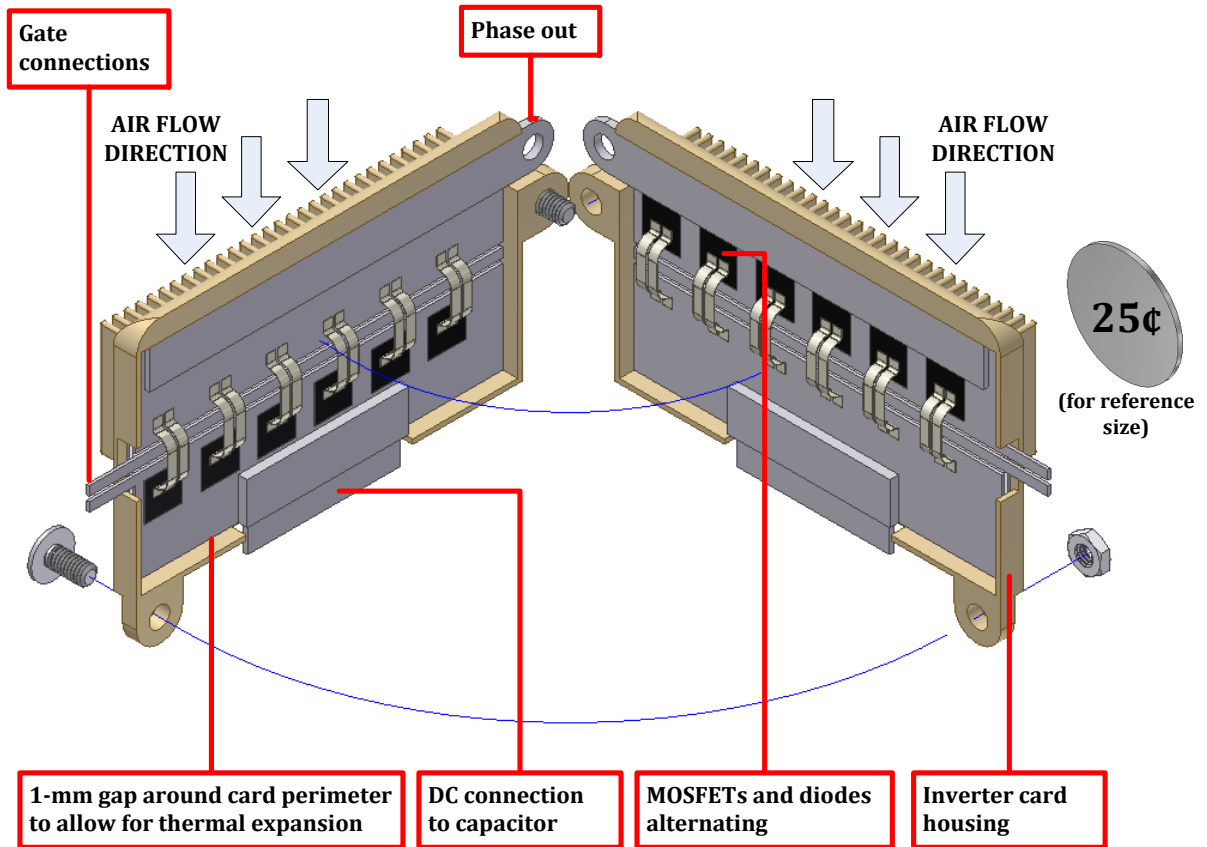
Figure 5.6 Inverter card inner details
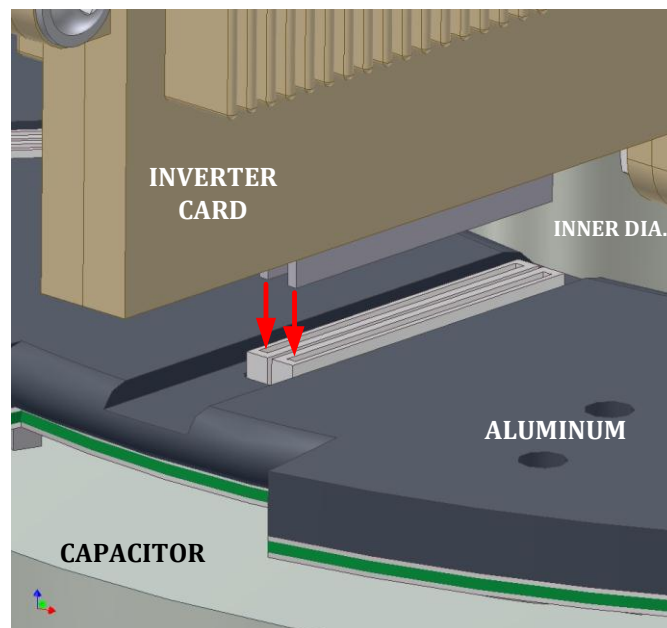
Figure 5.7 Card connectivity to capacitor positive and negative terminals

(TOP OF CARD)

10mm

HOUSING

DBA

ALUMINUM (1mm)
ALUMINUM (0.58mm)
ALUMINUM NITRIDE (0.66 mm)
ALUMINUM (0.58mm)

CHIP   CHIP

RIBBON BOND   RIBBON BOND   RIBBON BOND   RIBBON BOND   RIBBON BOND   RIBBON BOND

CHIP

GATE WIRE

0.044 in   0.064 in   0.079 in   0.128 in
(1.11 mm)   (1.632 mm)   (2 mm)   (3.5 mm)

Figure 5.8 Inverter card internal details and layout

5.3 Flow Characteristics – Results of Parametric Study

The numerical results characterizing the flow properties of the inverter are obtained for an inlet air flow rate of $30 \leq Q \leq 60$ cfm per unit cell and are presented in terms of pressure drop through the inverter and ideal blower power requirements in Table 5.2. The results represent a reduction in system pressure drop that is primarily due to the combined effect of changing the inlet to outlet area ratio, addition of flow partitions, capacitor tabs reconfiguration, addition of outer diameter leakage path, and a relatively minor negative effect of utilizing cooling fins. The combined effect of adding fins and reconfiguring the capacitor tabs were only investigated in the final concept, Revision G, and improved the pressure drop results by 28% at $Q = 60$ cfm from 6.4 inches H_2O to 5.0 inches H_2O compared to Revision F which was also evaluated at this flow rate. Furthermore, the inverter cards, structural components, fins, and capacitor inner edge are all rounded in order to eliminate unnecessary adverse pressure gradients associated with recirculation zones at these boundaries.

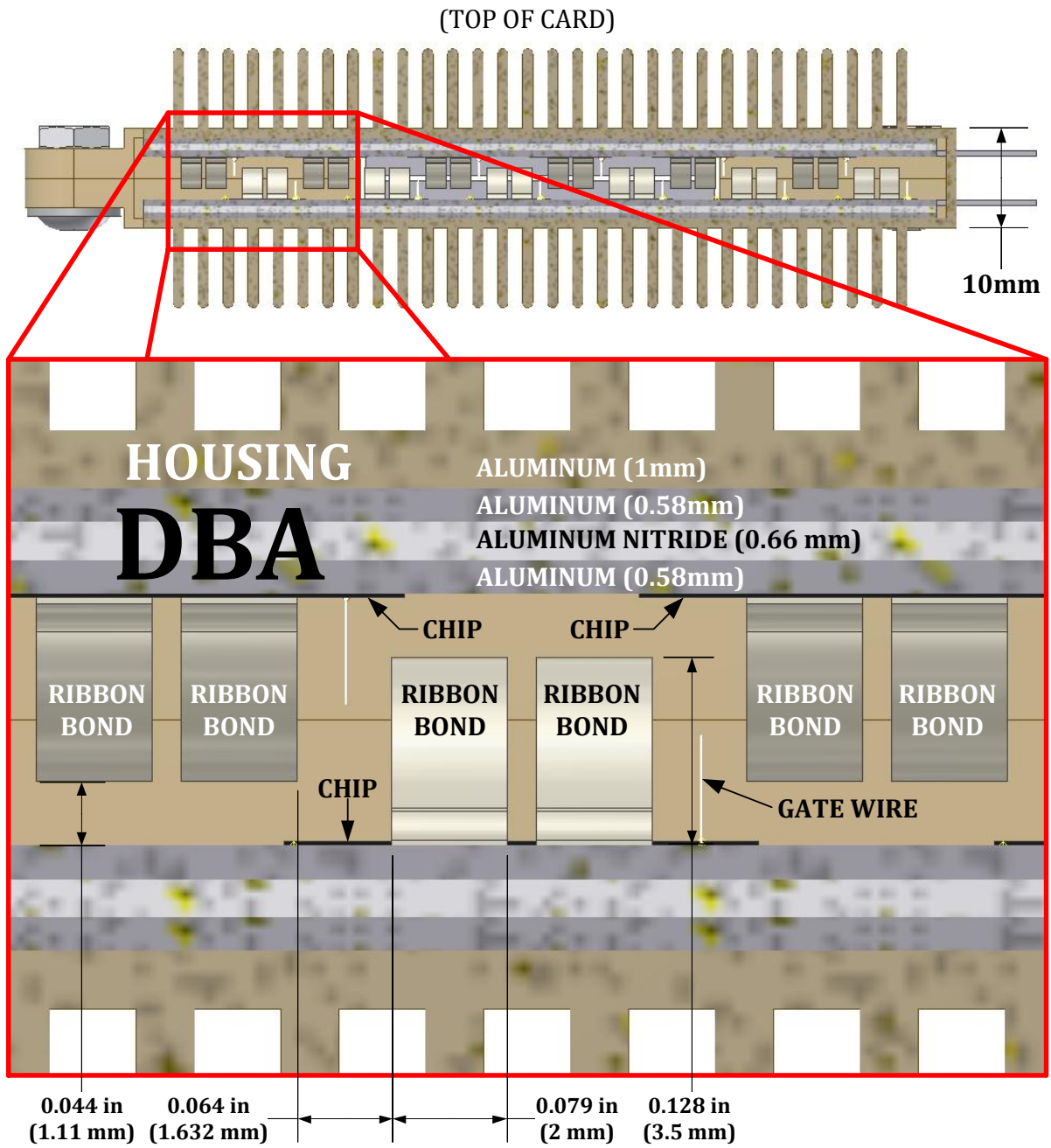With the flow partition and the addition of the fins in the final concept, the flow cross-sectional area became smaller and much more complex in shape. This could decrease the local hydraulic diameter significantly and thus Reynolds number. To be sure that the flow remains turbulent, the quantities are calculated at a position located at half of the length of the fins in the flow direction. The Reynolds number is computed at the inlet and the mid-section and given as a function of cell flow rate in Table 5.2. In general, flow is turbulent in circular pipes for $Re_D \geq 2300$ [31]. This principle serves as a guideline to verify the turbulent flow assumption made before calculating the pressure drop and blower power requirements numerically. The assumption is valid everywhere in the inverter since the lowest Reynolds number is $Re_{D_h} \cong 2700$ at the mid-length through the fins for a cell flow rate of $Q = 30$ cfm. Therefore, for all cases reported in this work reported here, turbulent flow models were used.

Table 5.1 Effective hydraulic diameter at inlet and mid-length of fins
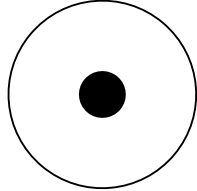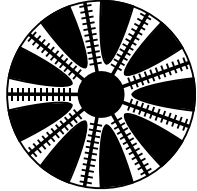
		Flow cross-section (white space is flow area)	
		at inlet	**at mid-length of fins**
Cross-sectional area, A_c	mm^2	40 326	13 717
Perimeter, $\wp$	mm	990	11 527
Hydraulic diameter, $D_h = \frac{4A_c}{\wp}$	mm	163	4.76

Table 5.2 Final concept flow characteristics numerical results

Volumetric flow rate per cell, Q	cfm	**30**	**40**	**50**	**60**
Total volumetric flow rate, $Q \times N$	cfm	270	360	450	540
Inlet velocity, U_{in}	m/s	3.2	4.2	5.3	6.4
	mph	7	9	12	14
Inlet Reynolds number, Re_{D_h}		32 560	43 420	54 270	65 120
Mid-section velocity, U_{mid}	m/s	9.29	12.4	15.5	18.6
	mph	21	28	35	42
Mid-section Reynolds number, Re_{D_h}		2 782	3 710	4 638	5 565
Pressure drop, ΔP	Pa	323	558	877	1 253
	inches H$_2$O	1.3	2.2	3.5	5.0
Ideal blower power input	W	40.3	92.6	182.0	312.0
	hp	0.05	0.12	0.24	0.42

5.4 Thermal Characteristics – Results of Parametric Study

5.4.1 Transient Results

The parametric study is conducted using the values summarized in Table 5.3 below, representing sixteen combinations of parametric values. The inlet air flow rate per unit cell is taken as the lowest and highest values used to determine the ideal blower power requirements summarized in Table 5.2 in the previous section, and the inlet air temperature is kept the same at 50°C in all transient simulations. The ambient air temperatures, T_{amb}, used in this parametric study represent typical ambient environments under the hood of an automobile where a power inverter is to be placed. Additionally, the ambient temperature is also the initial temperature of the entire system at the beginning of each transient simulation. That is, $T_0 = T_{amb}$. The voltage and switching frequency have been used to characterize the thermal performance of power electronics by previous authors [14]. The voltage, switching frequency, and current are used in the heat generation functions in equations (3.4) through (3.9) (see 3.1 Heat , page 14). Note that the only transient input parameter is the current of the MOSFETs and the diodes, according to the absolute US06 inverter current in Figure 3.3 (c) on page 19. Results are computed as a response to one US06 cycle.

Table 5.3 Input parameters used for transient simulations

Type	Variable	Units	Values
Parametric	Air flow rate per unit cell, Q	cfm	30, 60
	Ambient air temperature, T_{amb}	°C (°F)	50 (122), 120 (248)
	Voltage, V	V	450, 650
	Switching frequency, f_{sw}	kHz	10, 20
Fixed	Inlet air temperature, T_{in}	°C	50
Transient	Current, $I_{MOS} = I_{diode} = I$	A	$I_{US06}(t)/N$

The results of these simulations are summarized in Table 5.4. In the table, the simulations are numbered 1 through 16 for each combination of the parametric values. The maximum temperature of the models at each instance of time, $T_{max}(t)$, always occurs in heat-generating domains, i.e. the MOSFETs or diodes. The maximum temperature in the table, T_{max}, is the maximum junction temperature among all the devices at a given instance of time for one cycle. The time at which T_{max} occurs is also reported in the table and is denoted $t|_{T=T_{max}}$. The temperature at the end of one cycle is denoted T_{final} and is used to compute the change in temperature from the beginning to the end of one cycle, denoted $\Delta T_{cycle} = T_{final} - T_0$.

The strongest impact on the maximum temperatures shown in the table is the ambient temperature, T_{amb}. Thus, the color scheme of the table indicates a grouping of sixteen finite element models into four groups based on this parameter. Of all the models, the highest maximum device junction temperature reported is $T_{max} = 164°C$ (327°F) which is reported for the lowest air flow rate, and higher ambient temperature, voltage, and switching frequency—condition #8 in Table 5.4. The maximum temperature always occurred in a diode since the heat generated from the diodes are significantly higher than the power switches, as indicated in Figure 3.2 on page 17.

In the models for which $T_{amb} = 120°C$, the end of cycle maximum temperature is less than the initial temperature; that is, $T_{final} < T_0$, which is an important indication that a simulation of multiple cycles will not exceed the maximum temperature reported in Table 5.4. Observe that when $Q = 30$ cfm, $T_{amb} = 50°C$, $V = 650$ V, and $f_{sw} = 20$ kHz (model #4), the final temperature is 111°C. The temperature profile of a second transient cycle will be nearly identical to the temperature profile of the first cycle with $T_{amb} = 120°C$ (model #8) with the difference being that the surroundings is still at 50°C. In other words, the temperature profile of model #4 subject to a second transient cycle will yield similar results to model #8. One can infer from this result that the maximum temperature will not exceed 164°C for any $T_{amb} \leq 120°C$.

Table 5.4 Transient thermal results at $T_{in} = 50°C$

	INPUT PARAMETERS				RESULTS			
	Q	T_{amb}	V	f_{sw}	T_{max}	$t\vert_{T=T_{max}}$	T_{final}	ΔT_{cycle}
	CFM	°C	V	kHz	°C	seconds	°C	°C
1	30	50	450	10	103	575	84	34
2				20	108	593	90	40
3			650	10	116	575	93	43
4				20	142	593	111	61
5		120	450	10	142	13	87	-33
6				20	145	13	93	-27
7			650	10	152	13	97	-23
8				20	**164**	13	115	-5
9	60	50	450	10	92	575	74	24
10				20	99	575	77	27
11			650	10	105	575	79	29
12				20	121	593	90	40
13		120	450	10	124	13	74	-46
14				20	125	13	78	-42
15			650	10	133	13	80	-40
16				20	147	13	90	-30

The maximum junction temperature profiles with respect to time are presented in Figure 5.9 through Figure 5.14 showing the absolute US06 inverter current repeated from Figure 3.3 (c) for reference since the transient temperature profiles are understood in light of the input transient current. Figure 5.9 and Figure 5.10 give the temperature profiles of all sixteen of the transient computations and is segmented into separate plots for fixed Q and V and varying T_{amb} and f_{sw}. The temperature profiles for $Q = 60$ cfm in Figure 5.10 are less distinguishable from one another when compared to the temperature profiles for $Q = 30$ cfm in Figure 5.9 because the effect of each parameter in the results goes down when the air flow rate is increased. This might be explained by the following reasoning. With increasing airflow rate, the heat transfer coefficient and the ability to cool the system increases. At $Q = 60$ cfm, the results show that the increased heat loads associated with changes in parameters such as V, f_{sw}, etc. on T_{max} are not as significant. However, at $Q = 30$ cfm the cooling ability of air is lower and makes the system more sensitive to changes in heat load associated with parameters mentioned above.

(a)

(b) Q = 30 cfm, V = 450 V

Legend for (b):
- T_{amb} = 50°C, f_{sw} = 10 kHz
- T_{amb} = 50°C, f_{sw} = 20 kHz
- T_{amb} = 120°C, f_{sw} = 10 kHz
- T_{amb} = 120°C, f_{sw} = 20 kHz

(c) Q = 30 cfm, V = 650 V

Figure 5.9 Transient thermal results: (a) reference abs. US06 current (b) Q = 30 cfm, V = 450 V (c) Q = 30 cfm, V = 650 V

(a)

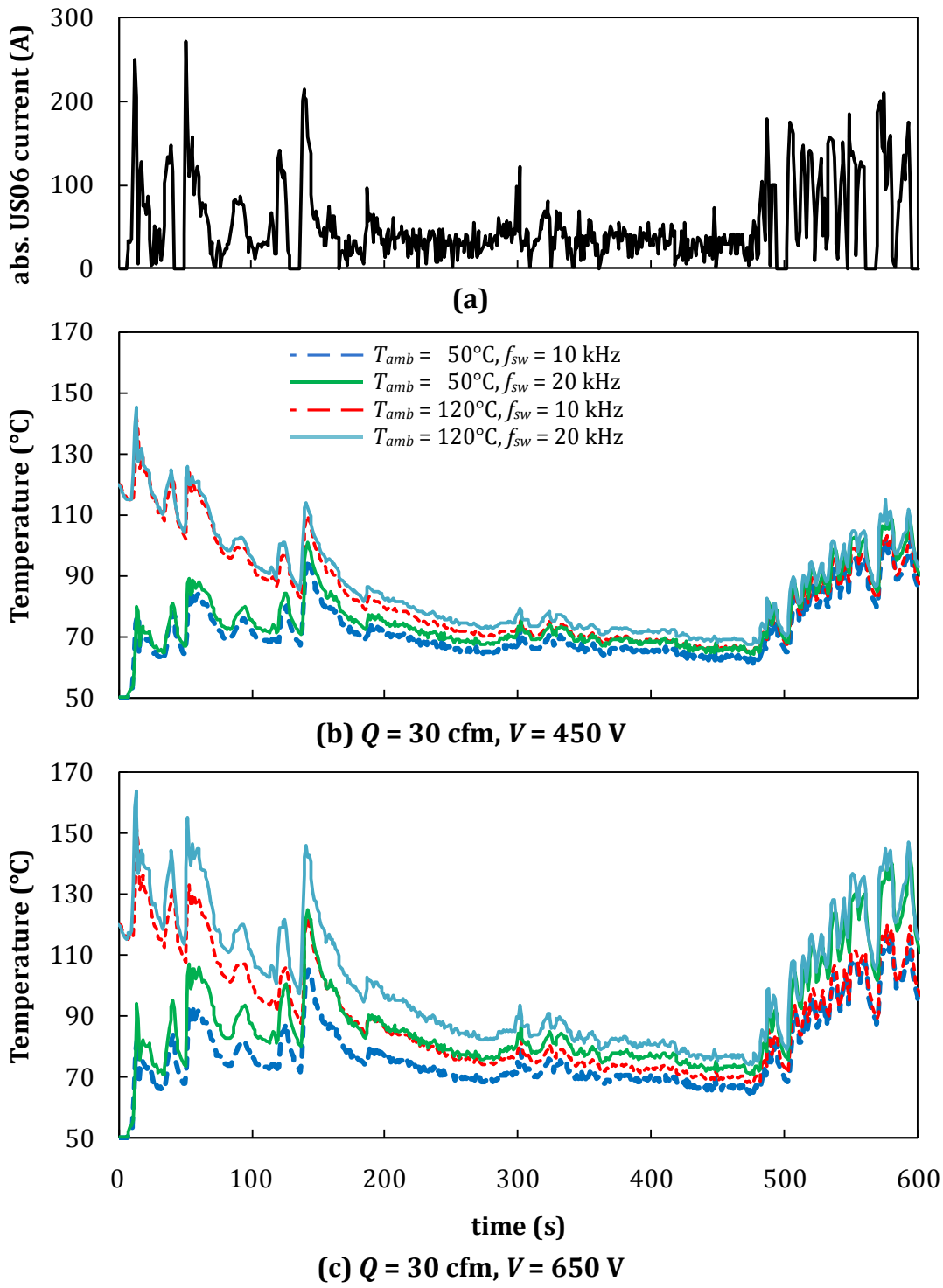**(b)** Q = 60 cfm, V = 450 V

(c) Q = 60 cfm, V = 650 V

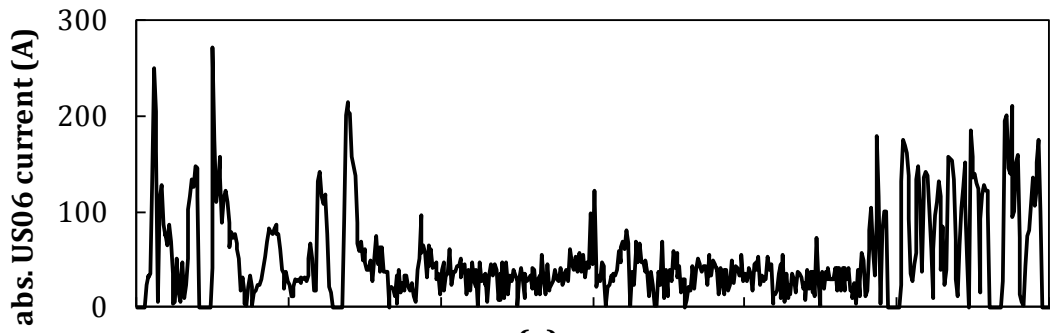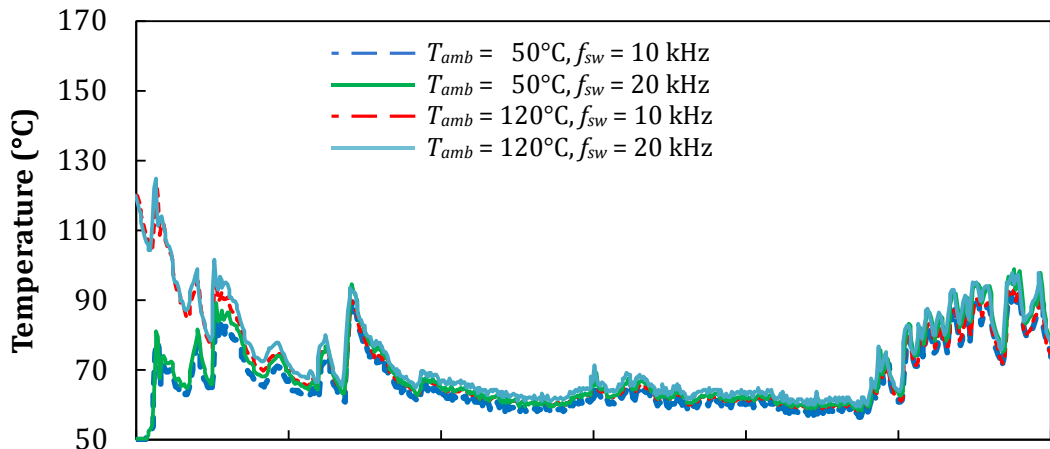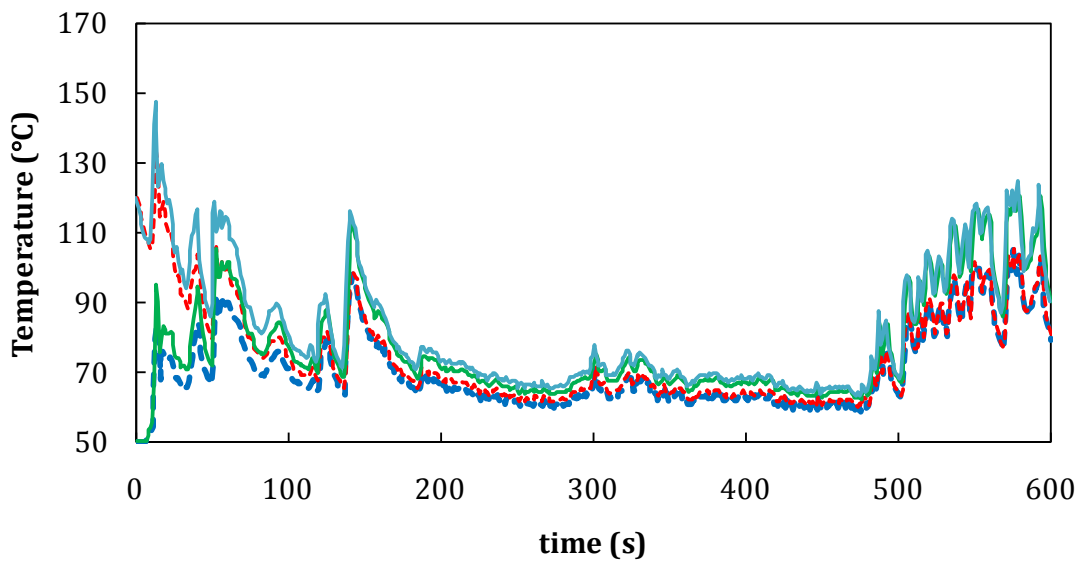Figure 5.10 Transient thermal results: (a) reference abs. US06 current (b) Q = 60 cfm, V = 450 V (c) Q = 60 cfm, V = 650 V

83

The succeeding plots, Figure 5.11 through Figure 5.14, present the results showing the influence of changing one parameter at a time on T_{max} while holding all others constant in order to characterize the system sensitivity to each variable. When one parameter is varied to reproduce two temperature profiles for each figure, the remaining fixed parameters take the values of $Q = 30$ cfm, $T_{amb} = 50°C$, $V = 650$ V, and $f_{sw} = 20$ kHz. These values are chosen for which higher maximum temperature is expected.

The effect of each parameter on maximum junction temperature for the fixed values described are quantified by taking the absolute value of the difference of the temperature profiles in subplot (b) and plotting the result in subplot (c) of each corresponding figure in Figure 5.11 through Figure 5.14. Figure 5.12 demonstrates the effect of T_{amb} on the results and indicates that the model is insensitive to T_{amb} after approximately 300 seconds as was suggested in Table 5.4. The results demonstrate the most model sensitivity to voltage when studied at the lower air flow rate and higher frequency as plotted in Figure 5.13 with a maximum absolute temperature difference between the two temperature profiles of Figure 5.13 (b) of 33°C. This low flow rate and higher frequency combination represents the worst case scenario as far as T_{max} is concerned.
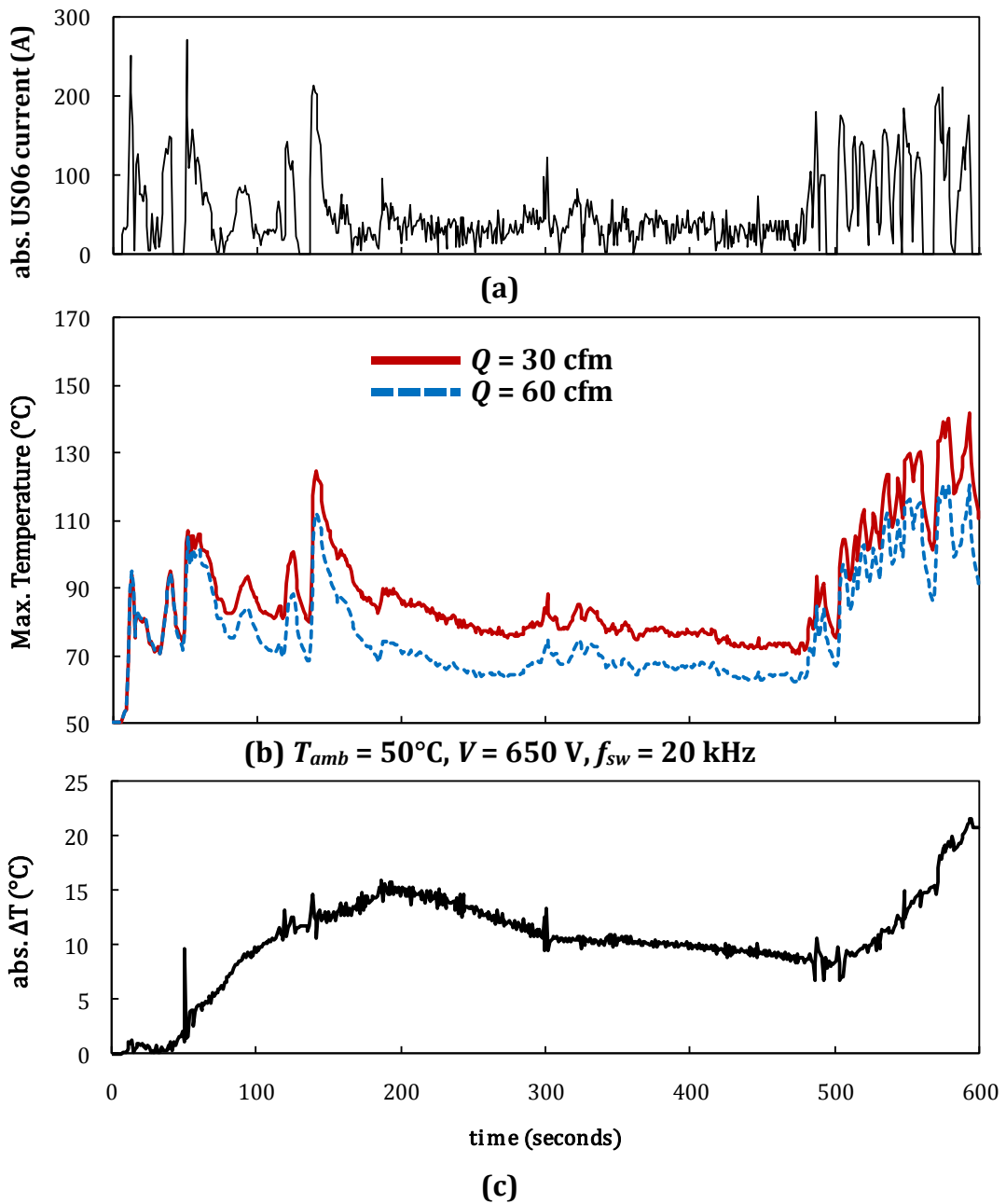
Figure 5.11 Transient thermal results for showing the affect of Q: (a) reference abs. US06 current (b) T_{max} for $T_{amb} = 50°C$, $V = 650\,V$, $f_{sw} = 20\,kHz$ (c) abs. difference of temperature profiles in (b)

Figure 5.12 Transient thermal results showing the affect of T_{amb}: (a) reference abs. US06 current (b) T_{max} for $Q = 30$ cfm, $V = 650$ V, $f_{sw} = 20$ kHz (c) abs. difference of temperature profiles in (b)

Figure 5.13 Transient thermal results showing the affect of voltage: (a) reference abs. US06 current (b) T_{max} for $Q = 30$ cfm, $T_{amb} = 50°C$, $f_{sw} = 20$ kHz (c) abs. difference of temperature profiles in (b)
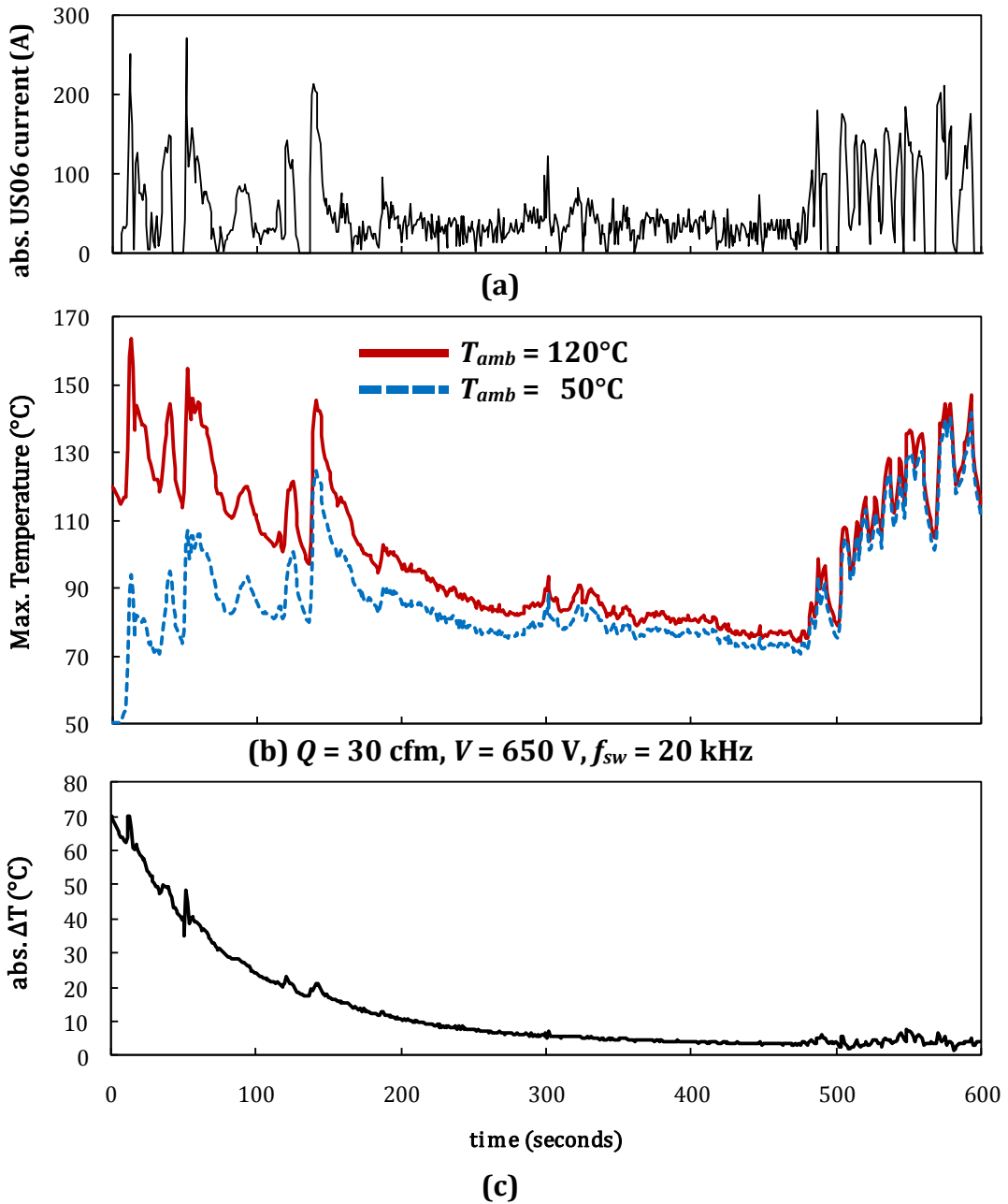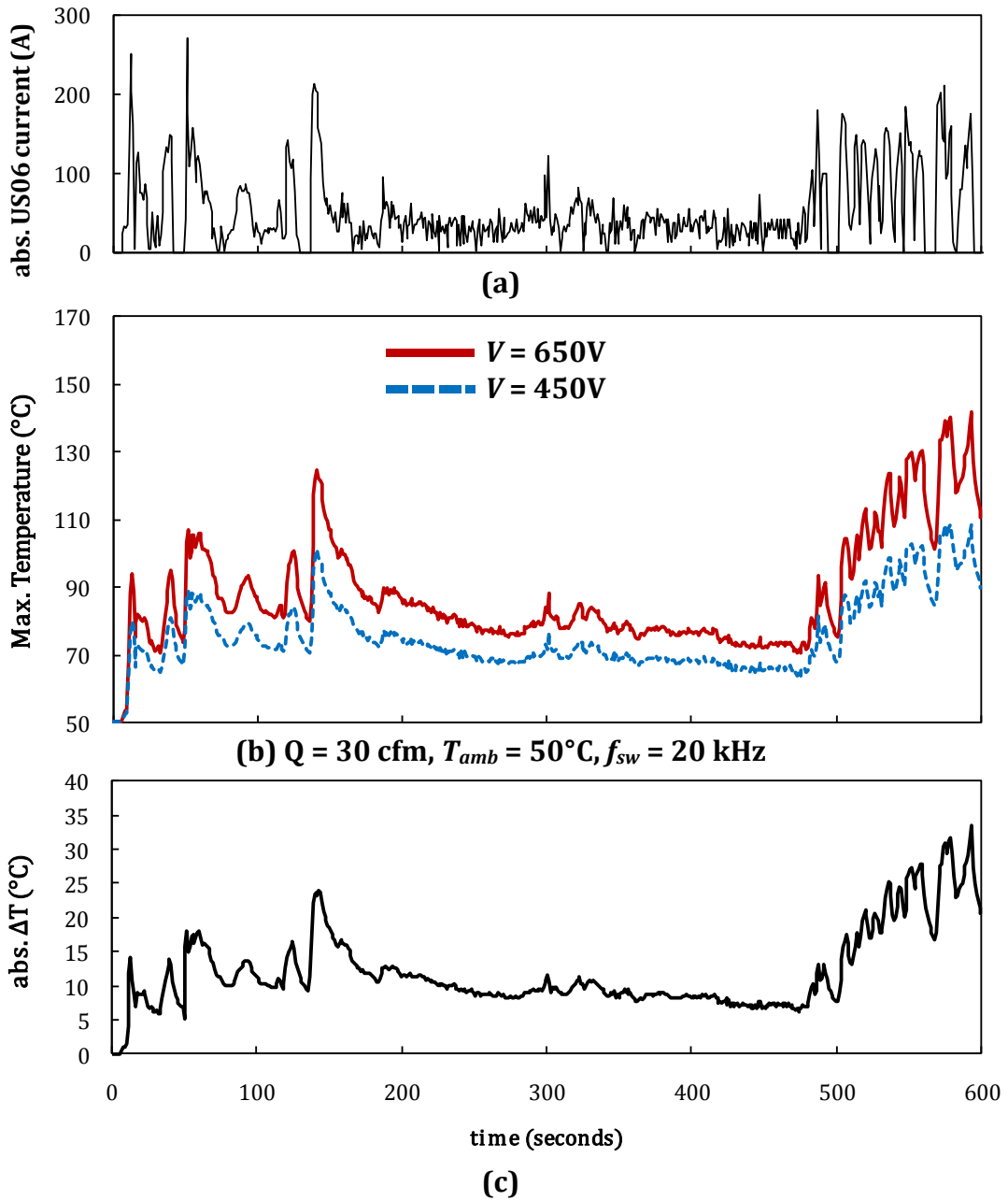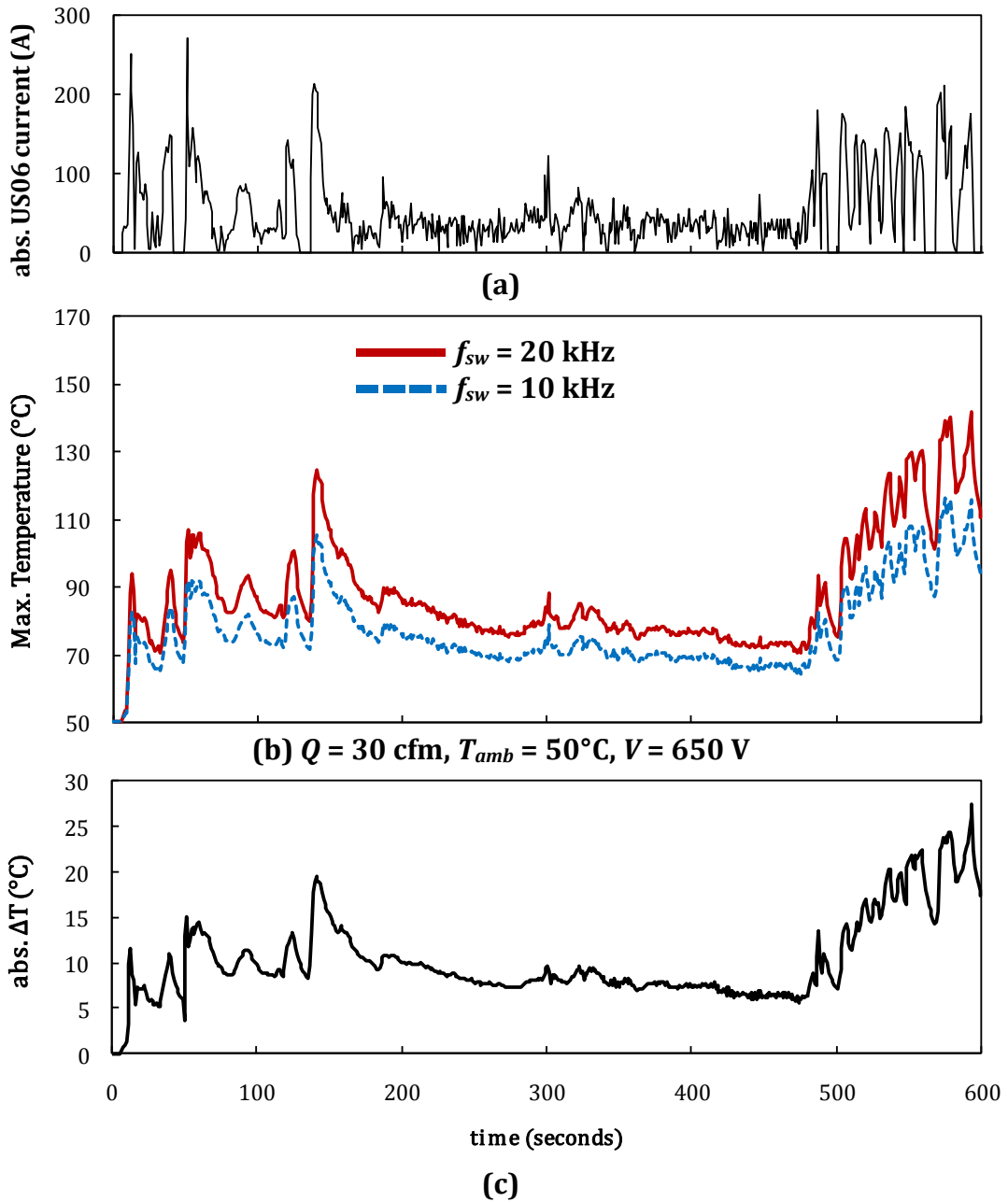
Figure 5.14 Transient thermal results showing the affect of f_{sw}: (a) reference abs. US06 current (b) T_{max} for $Q = 30$ cfm, $T_{amb} = 50°C$, $V = 650$ V (c) abs. difference of temperature profiles in (b)

5.4.2 Steady-State Results

The steady-state results are computed for a current of 82A because this value represents the highest time-integrated absolute US06 current supplied to the inverter when the drive cycle is segmented into three time intervals (see 3.2 Modeling Parameters, page 18). Additionally, the worst case parameters are chosen for the steady-state analysis. More specifically, the steady-state model is computed for $Q = 30$ cfm, $T_{amb} = 120°C$, $V = 650$ V, and $f_{sw} = 20$ kHz. The heat generated in each device and device junction temperatures computed for the steady-state scenario described are given in Figure 5.15 which indicates the relative placement of the devices and an average MOSFET and diode heat generation of $P_{MOS} = 9.4$ W and $P_{diode} = 19.1$ W, respectively, equating to 171 W of total heat generation per inverter cell.

The leftmost diode, D1, in Figure 5.15 is the device with the highest junction temperature which is, in fact, close to the temperature of the leftmost wall that interacts with the ambient temperature of $T_{amb} = 120°C$. The figure indicates the influence of alternately mounting the MOSFETs and

AIR FLOW DIRECTION

Figure 5.15 Heat generated, $\dot{q}$, and steady-state device temperature, T_j (°C).
$Q = 30$ cfm, $T_{amb} = 120°C$, $V = 650$ V, $f_{sw} = 20$ kHz. D and M represent
diode and MOSFET, respectively

diodes in the configuration as shown. In previous power inverter concepts, the relative placement was opposite of what is shown here—i.e. the top left device was M1, and the bottom right device was D6. In these previous models, th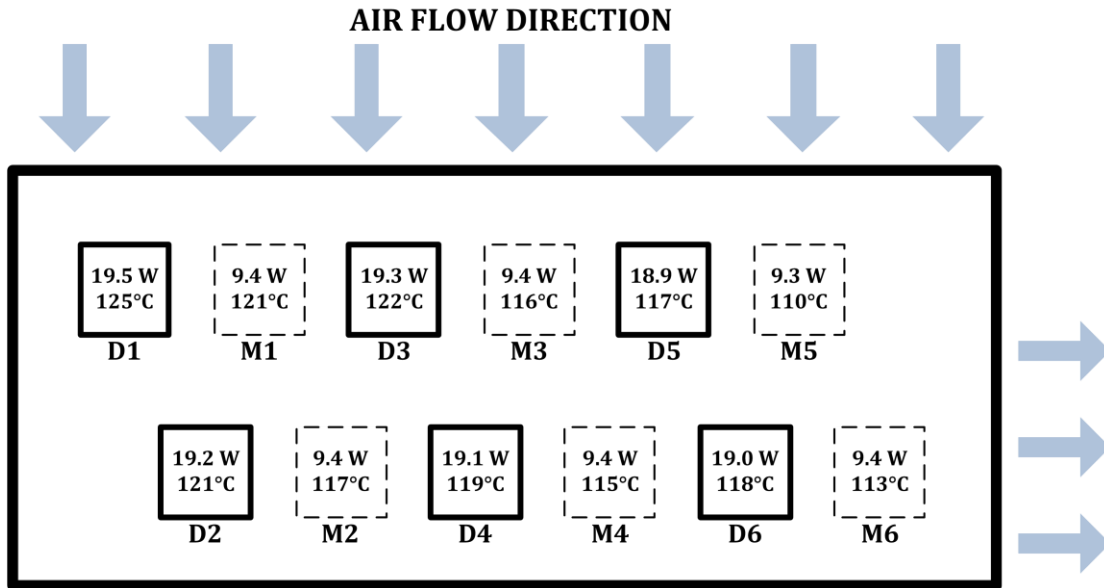e maximum device junction temperature was instead at the former location of D6 (currently the location of M6) because the fins do not extend the length of the card, and without sufficient heat removal from this device, the heat generated from the device also increased. For the present configuration, the vertical placement of the devices makes it possible to accommodate the inner connectivity of the devices to the substrate via ribbon bonds and wire bonds inside the card, and the vertical symmetry gives electrical characteristics that are better than vertically non-symmetric concepts. In other words, if the bottom row of MOSFETs and diodes were to be raised higher (raised towards the inlet) in order to be closer to the finned structure on the back side of the devices, the top row would need to be lowered to maintain vertical symmetry, and the heat distribution would be more concentrated instead of spread out more evenly. These adverse conditions are avoided by the configuration represented in Figure 5.14.

The solid domain surface temperature plots are presented below in Figure 5.16 and Figure 5.17 showing the temperature of the inverter card and structural components and the capacitor, respectively. The outer wall of the inverter card is exposed to the ambient environment, which is why the maximum in Figure 5.16 is 125°C as discussed above. As previously discussed, the material of construction used for all the structural components were changed to aluminum to make use of the additional heat transfer surfaces that interact with the air flow. In the steady-state results computed, the thermal conductivity of the inner hub is taken to be $k = 148 \, \text{W/m} \cdot \text{K}$ instead of $k = 177 \, \text{W/m} \cdot \text{K}$ to preserve conservativeness in the numerical results, especially since the current location of M6 is not in the nearest vicinity to the finned structure. The benefit of doing this is apparent since these components now take on the temperature of the inverter card and thereby provide additional area for direct cooling by air. The inner hub essentially makes up for heat transfer surface for M6 which is not in the near vicinity of the fins like the other devices are.
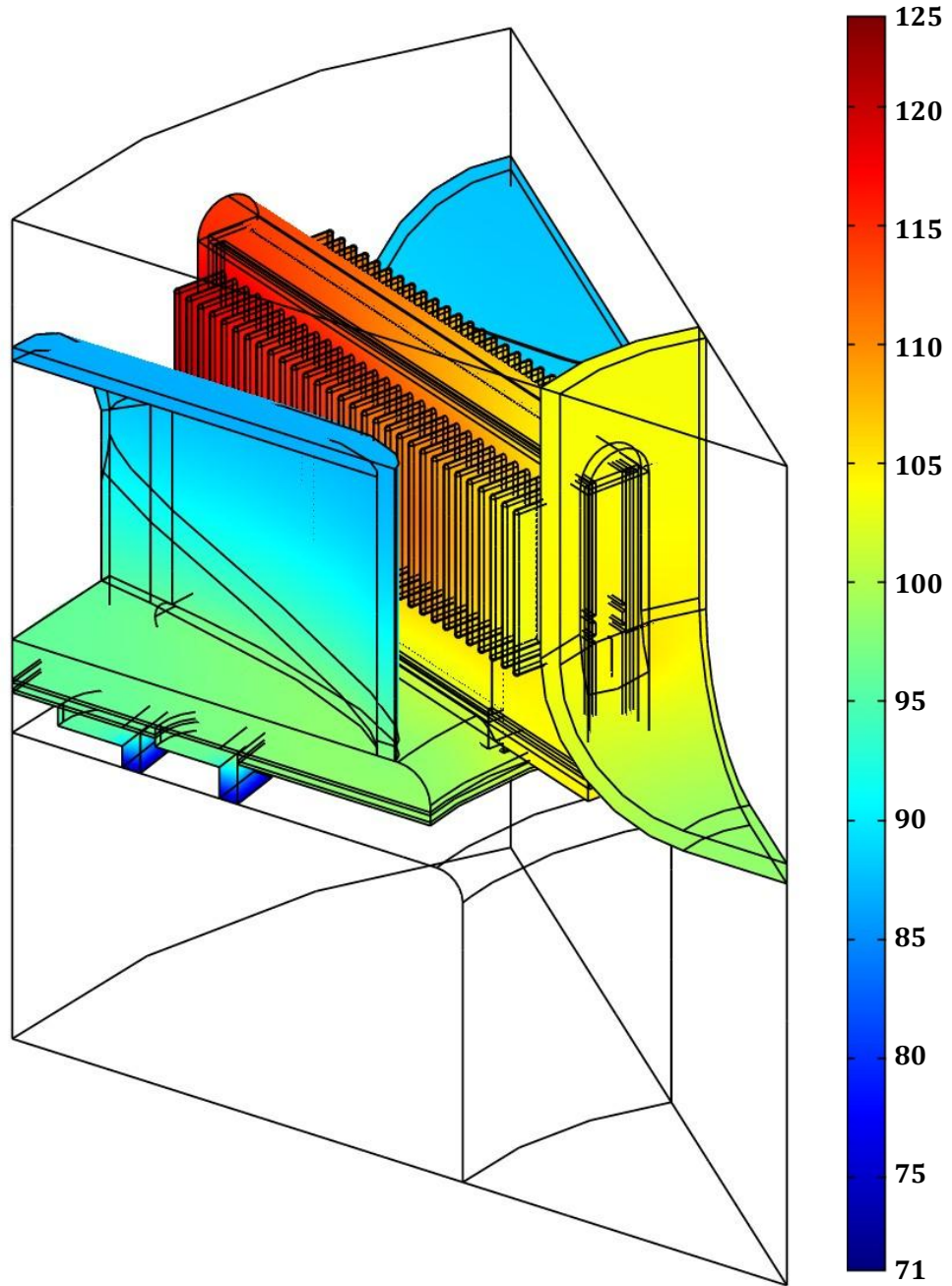
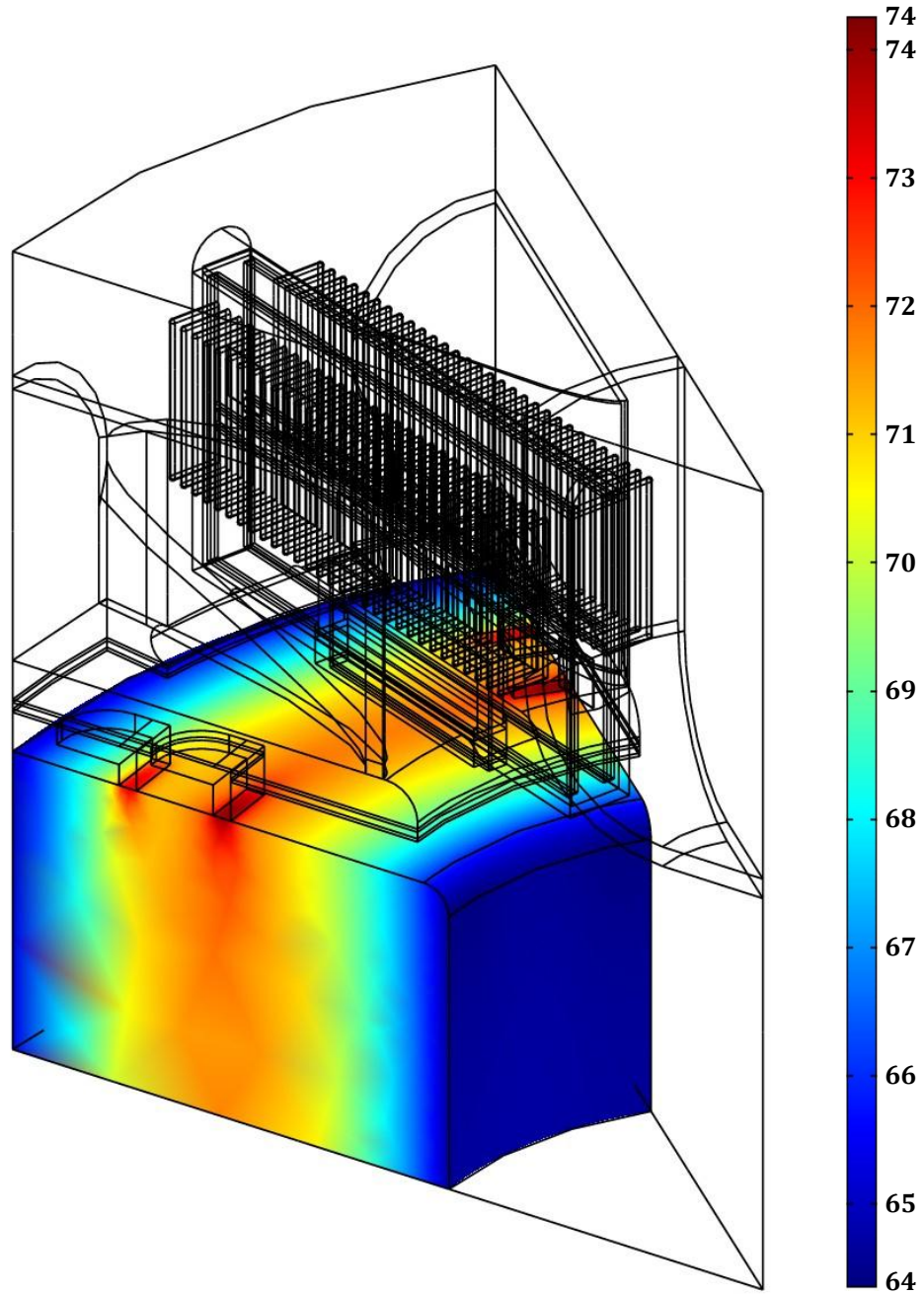Figure 5.16 Temperature distribution of solid domains of Revision GB inverter card, T_s (°C); $Q = 30$ cfm, $T_{amb} = 120$°C, $V = 650$ V, $f_{sw} = 20$ kHz

Figure 5.17 Temperature distribution of Revision GB capacitor, T_s (°C); $Q = 30$ cfm, $T_{amb} = 120°C$, $V = 650$ V, $f_{sw} = 20$ kHz

Chapter 6.   Conclusions

6.1 Summary

The purpose of this study is to determine the thermal feasibility of using air to cool an electronic power inverter. The research objective primarily addresses the need to reduce the weight and volume of the power electronics systems with their dedicated auxiliary systems onboard a hybrid electric vehicle. Cooling a power inverter with air will eliminate the need to store a dedicated cooling water system, and is an alternative approach to the idea of integrating the power inverter into the cooling loop of the internal combustion engine. The configuration of the air-cooled inverter presented in this study incorporates a cylindrical shape accommodating a collinear axial air blower and a cylindrical capacitor with a center hole. Inverter cards are oriented radially above the capacitor. The present work is a continuation of FY 2009 in which a radial inflow inverter concept was presented, and lessons learned from that study are incorporated into the design process of the present work.

Thermal feasibility is established using numerical computational methods by finite element analysis. The problem is considered in a multidisciplinary, integrated approach. That is, electrical circuitry layout is designed in tandem with the thermal management of the devices as opposed to designing a thermal packaging system to accommodate electrical hardware. Although computational results govern the analysis, experimental results are used to model the heat generated from each of the heat-generating devices. The heat generation is modeled as a function of the junction temperature, current, voltage, and switching frequency. Note that the junction temperature is an important result of the computations. Thus, the numerical analysis is iterative on the junction temperature and the heat generation in both steady-state and transient simulations.

The work began by simply reconfiguring the flow field around the inverter cards and the capacitor from the radial inflow inverter concept for which the outlet cross-sectional area was 10% of

the inlet cross-sectional area. The flow characteristics were improved from the initial axial inflow concept by reducing the pressure drop through the system by 53%. The developed concept uses an increased outlet to inlet area ratio, and incorporated flow partitions that guide the flow of air toward the near vicinity of each inverter card to lower the pressure drop through the system. The ideal blower power input required for an axial fan is 5.7 inches H_2O at 60 cfm.

The parametric values in this investigation represent values that are encountered for automotive applications. For the parametric variables studied, the lowest air flow rate in this investigation is 30 cfm, and the highest values of the other parameters simulated are ambient temperature, 120°C; voltage, 650 V; and switching frequency, 20 kHz. In the transient simulations, current is a function of time. The transient thermal response is computed when the system is subject to transient inverter current representing the US06 supplemental federal test procedure from the United States Environmental Protection Agency. In these simulations, the initial temperature of the system is the same as the ambient temperature specified. A steady-state computation is presented for a time-integrated current value that represents the last segment of the US06 supplemental test procedure when the procedure is segmented into three distinct time intervals.

When the model is subject to one or multiple current cycles, the maximum temperature does not exceed 164°C (327°F) for the combination of parameters studied that will yield the highest temperature profile. Although the maximum temperature in one cycle is most sensitive to ambient temperature, the ambient temperature affect decays after approximately half the duration of one cycle. Of the parametric variables considered, the system is most sensitive to inlet air flow rate.

6.2 Recommendations

The first recommendation for future work is in regards to model validation. More validation can quantify the difference between the standard k-ϵ model and the Wilcox (2006) k-ω model for turbulent flow heat transfer computations. In addition to this, the results are also affected by overall

mesh density and the mesh density in the finned structure. With a low mesh density especially in the solid domains, global energy balance error increases and the maximum temperatures may be reported to be lower as a result. Because air flow through fins are approximated as small channels of air flow, an important consideration is the amount of mesh elements across each flow channel—that is, the number of elements from fin to fin. Furthermore, the results of this validation study may be subject to the turbulent flow model used and the amount of heat generated in the simplified models.

A second recommendation is in regards to the physical phenomena of the problem. Finite element analysis computations were performed under the constant property assumptions in order to preserve computational resources. That is, flow quantities are solved for separately from the thermal solution, which lowers the computational requirements. However, the kinematic viscosity of air can be increased by approximately 65% over a 100°C temperature range, which decreases the Reynolds number and increases the maximum temperatures. With the ambient air, inlet air, and maximum solid temperatures now known, the properties can be chosen at higher temperatures and still be assumed constant.

The axial flow cylindrical inverter concept is studied for sixteen combinations of air flow rate, ambient temperature, voltage, switching frequency in transient simulations where the current is a function of time. For steady state simulations where the current is held constant, only the combination of parameters that would yield the highest expected temperatures was studied. One would understand the effect of flow rate, ambient temperature, voltage, and switching frequency at steady-state conditions if these variables were studied parametrically with a constant device current, and this study is left as a future recommendation.

The scope of power electronics research for high temperature applications has included thermal expansion and thermal cycling fatigue. These considerations would need to be addressed for the axial flow cylindrical capacitor in future studies.

95

References

[1]   "2011 Toyota Camry Technical Specifications - Kelley Blue Book." [Online]. Available: http://www.kbb.com/new-cars/toyota/camry/2011/specifications-technical?id=264161 &category=sedan. [Accessed: 22-Nov-2010].

[2]   "2011 Toyota Camry Hybrid Technical Specifications - Kelley Blue Book." [Online]. Available: http://www.kbb.com/new-cars/toyota/camry/2011/specifications-technical?id=264165 &category=sedan. [Accessed: 22-Nov-2010].

[3]   K. T. Lowe, I. T. Bodey, J. C. Faulkner, and R. V. Arimilli, Annual technical report on the feasibility of thermal packaging of air-cooled WBG inverter. Knoxville, TN: Mechanical, Aerospace, and Biomedical Engineering Department, The University of Tennessee, 2009.

[4]   Elshabini and F. D. Barlow, High-Temperature High-Power Packaging Techniques for HEV Traction Applications. 2006.

[5]   M. Chinthavali, L. M. Tolbert, H. Zhang, J. H. Han, F. Barlow, and B. Ozpineci, "High power SiC modules for HEVs and PHEVs," in Power Electronics Conference (IPEC), 2010 International, pp. 1842–1848, 2010.

[6]   T. Stockmeier, "From Packaging to "Un"-Packaging-Trends in Power Semiconductor Modules," in Proc. IEEE International Symposium on Power Semiconductor Devices and IC's, pp. 12–19, 2008.

[7]   N. R. Jankowski, L. Everhart, B. Morgan, B. Geil, and P. McCluskey, "Comparing microchannel technologies to minimize the thermal stack and improve thermal performance in hybrid electric vehicles," in Vehicle Power and Propulsion Conference, 2007. VPPC 2007. IEEE, pp. 124–130, 2008.

[8]   S. Kubota, T. Sakurai, and H. Okada, "Size and Weight Reduction Technology for a Hybrid System," SAE International Journal of Engines, vol. 2, no. 1, p. 1143, 2009.

[9]   N. Nozawa, T. Maekawa, S. Nozawa, and K. Asakura, "Development of Power Control Unit for Compact-Class Vehicle," SAE International Journal of Passenger Cars-Electronic and Electrical Systems, vol. 2, no. 1, p. 376, 2009.

[10] Y. Mizuno et al., "Development of New Hybrid Transmission for Compact-Class Vehicles," SAE International Journal of Engines, vol. 2, no. 1, p. 742, 2009.

[11] J. D. Scofield, J. N Merrett, J. Richmond, A. Agarwal, and S. Leslie, "Performance and Reliability Characteristics of 1200 V, 100 A, 200°C Half-Bridge SiC MOSFET-JBS Diode Power Modules," presented at the International Conference on High Temperature Electronics, Albuquerque, NM, 2010.

[12] M. A. Huque, L. M. Tolbert, B. J. Blalock, and S. K. Islam, "A High-Temperature, High-Voltage SOI Gate Driver IC with High Output Current and On-Chip Low-Power Temperature Sensor," in IMAPS International Symposium on Microelectronics, pp. 1–5.

[13] V. Bondarenko et al., "Characterization and Packaging of SiC JFET Power Modules for Extreme Environment Motor Drives," in Proceedings of the 2006 International High Temperature Electronics Conference, Santa Fe, NM, pp. 488–456, 2006.

[14] M. S. Chinthavali, B. Ozpineci, and L. M. Tolbert, "High-temperature and high-frequency performance evaluation of 4H-SiC unipolar power devices," in Applied Power Electronics Conference and Exposition, 2005. APEC 2005. Twentieth Annual IEEE, vol. 1, pp. 322–328, 2005.

[15] S. Hodge Jr, "SiC Schottky Diodes in Power Factor Correction."

[16] B. Ozpineci, L. M. Tolbert, S. K. Islam, and F. Z. Peng, "Testing, characterization, and modeling of SiC diodes for transportation applications," in Power Electronics Specialists Conference, 2002. pesc 02. 2002 IEEE 33rd Annual, vol. 4, pp. 1673–1678, 2002.

[17] L. M. Tolbert, B. Ozpineci, S. K. Islam, and F. Z. Peng, "Impact of Sic Power Electronic Devices for Hybrid Electric Vehicles," 2002.

[18] E. Hornung and U. Scheuermann, "Reliability of low current electrical spring contacts in power modules," Microelectronics Reliability, vol. 43, no. 9, pp. 1859–1864, 2003.

[19] D. C. Katsis and Y. Zheng, "Development of an extreme temperature range silicon carbide power module for aerospace applications," in Power Electronics Specialists Conference, 2008. PESC 2008. IEEE, pp. 290–294, 2008.

[20] J. D. Scofield, N. Merrett, J. Richmond, A. Agarwal, and S. Leslie, "Electrical and Thermal Performance of 1200 V, 100 A, 200° C 4H-SiC MOSFET-Based Power Switch Modules," in Materials Science Forum, vol. 645, pp. 1119–1122, 2010.

[21] D. B. Tuckerman and R. F. W. Pease, "High-performance heat sinking for VLSI," Electron Device Letters, IEEE, vol. 2, no. 5, pp. 126–129, 2005.

[22] R. J. Philips, Microchannel heat sinks. Massachusetts Inst. of Tech., Lexington (USA). Lincoln Lab., 1988.

[23] G. M. Harpole and J. E. Eninger, "Micro-channel heat exchanger optimization," in Semiconductor Thermal Measurement and Management Symposium, 1991. SEMI-THERM VII. Proceedings., Seventh Annual IEEE, pp. 59–63, 2002.

[24] D. Copeland, H. Takahira, W. Nakayama, and B. C. Pak, "Manifold microchannel heat sinks: Theory and experiment," Therm. Sci. Eng, vol. 3, no. 2, pp. 9–15, 1995.

[25] P. Salvati, F. Brucchi, and A. De Medici, Sinusoidal Inverter using SEMITOP® modules for Electric Vehicles applications. Semikron.

[26] "Federal Test Procedure Revisions | Cars and Light Trucks | US EPA." [Online]. Available: http://www.epa.gov/otaq/sftp.htm. [Accessed: 16-Nov-2010].

[27] T. Hosking, "Eddy Current Effects in Film Capacitors and their Impact on Interconnect Systems in High Power Applications," presented at the Motor, Drive & Automation Systems Conference 2009, Orlando, FL, 2009.

[28] F. M. White, Viscous Fluid Flow, 3rd ed. McGraw-Hill Education (ISE Editions), 2005.

[29] D. C. Wilcox, Turbulence Modeling for CFD, 3rd ed. Dcw Industries, Incorporated, 2006.

[30] W. Kays, M. Crawford, and B. Weigand, MP for Convective Heat & Mass Transfer, 4th ed. McGraw-Hill Science/Engineering/Math, 2004.

[31] F. P. Incropera and D. P. DeWitt, Fundamentals of Heat and Mass Transfer, 5th Edition, 5th ed. Wiley, 2001.

[32] "Quadrant Torlon EPP Duratron® T4203 PAI, Polyamide-imide, extruded (electrical grade)." [Online]. Available: http://quadrant.matweb.com/SpecificMaterial_torlon.asp ?bass-num=P1SM38. [Accessed: 30-Nov-2010].

[33] "Cotronics(r) Rescor 914 Datasheet."

[34] "Materials — Aluminum Nitride (AlN) Properties." [Online]. Available: http://accuratus .com/alumni.html. [Accessed: 30-Nov-2010].

[35] "Materials — Silicon Carbide (SiC) Properties." [Online]. Available: http://accuratus.com/ silicar.html. [Accessed: 30-Nov-2010].

[36] F. Breit, D. Malec, and T. Lebey, "Investigations on DC conductivity and space charge in silicone gel," in Electrical Insulation and Dielectric Phenomena, 2002 Annual Report Conference on, pp. 48–51, 2002.

[37] F. M. White, Fluid mechanics. McGraw-Hill, 2003.

[38] L. F. Moody, "Friction factors for pipe flow," Trans. ASME, vol. 66, no. 8, pp. 671–677, 1944.

Appendices

TempDepGen3main.m

```matlab
% This MATLAB code is used to display the heat generation model.
% Also included is a function file
% used in this script called "TempDepGen3function.m"

% TempDepGen3main.m

clc; clear all; close all;
set(0,'DefaultTextFontsize',10,...
    'DefaultTextFontname','Cambria',...
    'DefaultAxesFontname','Cambria');


% Input Parameters
Imos = 240/9; %A
Idiode = 240/9; %A
f = [10000,20000]; % kHz
V = [450,650]; % V
Tamb = 25; % deg C
Trange = 175; % deg C

% Raw Data, MOSFET
Rmosr    =   [  25 0.0169  ;  ...
                75 0.015   ;  ...
               100 0.0156  ;  ...
               125 0.0158  ;  ...
               154 0.0169 ];  % Ohms


PmosCondr = (2*Rmosr(:,2))*Imos^2; % WATTS
PmosCondr = [Rmosr(:,1),PmosCondr];

% Raw Data, DIODE
Rdioder   = [  25 0.0089  ;  ...
                75 0.0113  ;  ...
               100 0.0127  ;  ...
               125 0.0145  ;  ...
               154 0.0175 ];  % Ohms


PdiodeCond1r = (2*Rdioder(:,2))*Idiode^2; % WATTS
PdiodeCond1r = [Rdioder(:,1),PdiodeCond1r];

Vdioder    = [  25 0.873  ; ...
                75 0.8385 ; ...
               100 0.796  ; ...
               125 0.775  ; ...
               154 0.73  ]; % Volts


PdiodeVr = Vdioder(:,2)*Idiode; % WATTS
PdiodeVr = [Vdioder(:,1),PdiodeVr];


PdiodeCondr = [Rdioder(:,1),PdiodeCond1r(:,2)+PdiodeVr(:,2)];
```

```matlab
% Equation Scaling
ImosScale = Imos/62.5;
IdiodeScale = Idiode/62.5;

% Independent Variable: Temperature
T = Tamb:0.1:(Tamb+Trange);
M = zeros(length(T),length(f)*length(V)); % mosfet temperatures
D = zeros(length(T),length(f)*length(V)); % diode temperatures

if Imos == Idiode
    di = ['I_{m} = I_{d} = ',num2str(round(Imos)),'A'];
else
    di = ['I_{m} = ',num2str(round(Imos)),'A',...
            ', I_{d} = ',num2str(round(Idiode)),'A'];
end

yaxislabel = 'Heat Dissipation, Watts';
xaxislabel = 'Temperature, °C';

n = 0; k = 0; lw = 2;
for ff = f

    n = n + 1;
    m = 0;
    df = ['f_{sw} = ',num2str(ff/1000),'kHz'];

    for VV = V

        m = m + 1;
        k = k + 1;
        dv = ['V = ',num2str(VV),'V'];

        if VV <= 500
            Vscale = VV/400;
            EmosSwitr = [   25 0.0028305   ; ...
                            75 0.002841    ; ...
                           150 0.0029133  ]; % Joules
            EdiodeSwitr = [ 25 0.00082    ; ...
                            75 0.00091    ; ...
                           150 0.00088    ]; % Joules

        elseif VV > 500
            Vscale = VV/600;
            EmosSwitr = [   25 0.00391925 ; ...
                            75 0.0040845  ; ...
                           150 0.004402   ]; % Joules
            EdiodeSwitr = [ 25 0.002215   ; ...
                            75 0.00345    ; ...
                           150 0.0067875 ]; % Joules

        end % if statement for Voltage
```

103

```matlab
        PmosSwitr = ff*EmosSwitr(:,2)/2 * ImosScale*Vscale; % WATTS
        PmosSwitr = [EmosSwitr(:,1),PmosSwitr];

        PdiodeSwitr = ff*EdiodeSwitr(:,2)/2 * IdiodeScale*Vscale;
        PdiodeSwitr = [EdiodeSwitr(:,1),PdiodeSwitr];

        %%%%%%%%%%%%%%%%%%%%%%%%%%%%%%%%%%%%%%%%%%%%%%%%%%%%%%%%
        %%% TEMPERATURE-DEPENDENT GENERATION CALCULATIONS %%%
        %%%%%%%%%%%%%%%%%%%%%%%%%%%%%%%%%%%%%%%%%%%%%%%%%%%%%%%%

        [mt,mc,ms,dt,dc,ds] = TempDepGen3Function(VV,ff,Imos,Idiode,T);

        data(k) = struct('f',ff,'V',VV,'Im',Imos,'Id',Idiode,...
            'Pmt',mt,'Pdt',dt,...
            'Pmc',mc,'Pms',ms,'Pdc',dc,'Pds',ds,...
            'description', [dv, ', ', df]);

        figure(1); hold on;
        subplot(length(f),length(V),k); hold on;
        plot(T,mt,'LineWidth',lw);
        plot(T,mc,'--'); plot(T,ms,'-.');
        scatter(PmosCondr(:,1),PmosCondr(:,2),'b');
        scatter(PmosSwitr(:,1),PmosSwitr(:,2),'b');
        title(data(k).description);
        xlabel(xaxislabel)
        ylabel(yaxislabel)
        ylim([0 50])

        figure(2); hold on;
        subplot(length(f),length(V),k); hold on;
        plot(T,dt,'LineWidth',lw);
        plot(T,dc,'--'); plot(T,ds,'-.');
        scatter(PdiodeCondr(:,1),PdiodeCondr(:,2),'b');
        scatter(PdiodeSwitr(:,1),PdiodeSwitr(:,2),'b');
        title(data(k).description);
        xlabel(xaxislabel)
        ylabel(yaxislabel)
        ylim([0 100])

        clear mt mc ms dt dc ds PmosSwitr PdiodeSwitr;

    end % for loop for Voltage

end % for looop for frequency



figure(1)
ha = axes('Position',[0 0 1 1],'Xlim',[0 1],'Ylim',[0 1],...
    'Box','off','Visible','off','Units','normalized','clipping','off');
text(0.5, 1,['\bf MOSFET POWER DISSIPATION, ',di],...
```

```matlab
    'HorizontalAlignment','center','VerticalAlignment', 'top')

figure(2)
ha = axes('Position',[0 0 1 1],'Xlim',[0 1],'Ylim',[0 1],...
    'Box','off','Visible','off','Units','normalized','clipping','off');
text(0.5, 1,['\bf DIODE POWER DISSIPATION, ',di],...
    'HorizontalAlignment','center','VerticalAlignment', 'top')

lw2 = lw*0.65;
figure(3); close;
%figure(3); hold on;
subplot(1,2,1); hold on;
plot(T,data(1).Pmt,'b-.','LineWidth',lw);
plot(T,data(3).Pmt,'r-.','LineWidth',lw);
plot(T,data(2).Pmt,'b','LineWidth',lw);
plot(T,data(4).Pmt,'r','LineWidth',lw);



title('MOSFET Power Dissipation');
xlim([Tamb Trange]);
ylim([25 90]);
xlabel(xaxislabel)
ylabel(yaxislabel)
legend(data(1).description,...
       data(3).description,...
       data(2).description,...
       data(4).description,...
        'Location','Best')

subplot(1,2,2); hold on;
%figure(4); hold on;
plot(T,data(1).Pdt,'b-.','LineWidth',lw);
plot(T,data(3).Pdt,'r-.','LineWidth',lw);
plot(T,data(2).Pdt,'b','LineWidth',lw);
plot(T,data(4).Pdt,'r','LineWidth',lw);

title('Diode Power Dissipation');
xlim([Tamb Trange]);
ylim([25 90]);
xlabel(xaxislabel)
ylabel(yaxislabel)
legend(data(1).description,...
       data(3).description,...
       data(2).description,...
       data(4).description,...
        'Location','Best')
```

TempDepGen3Function.m

```matlab
% This MATLAB code is used to display the heat generation model.

function [Pmt,Pmc,Pms,Pdt,Pdc,Pds] = Temp-
DepGen3Function(Vinput,fsw,Imos,Idiode,T)
% Temperature Dependent Generation for MOSFETS and Diode

%mosfet conduction
a1 = 2E-5;
a2 = 0.0132;
Rmos = a1.*T+a2;
PmosCond = (2*Rmos)*(Imos^2);

%diode conduction
c1 = 3e-7;
c2 = 2e-5;
c3 = 0.0084;
Rdiode = c1.*T.^2 + c2.*T + c3;
PdiodeCond = (2*Rdiode)*(Idiode^2);

d1 = -0.0011;
d2 = 0.909;
Vdiode = d1.*T+d2;
PdiodeV = Vdiode.*Idiode;

% Equation Scaling
ImosScale = Imos/62.5;
IdiodeScale = Idiode/62.5;

if Vinput <= 500
    Vscale = Vinput/400;
    b1 = 7e-7; b2 = 0.0028; % mosfet switching
    e1 = 4e-7; e2 = 0.0008; % diode switching
elseif Vinput > 500
    Vscale = Vinput/600;
    b1 = 4e-6; b2 = 0.0038; %mosfet switching
    e1 = 4e-5; e2 = 0.0011; %diode switching
end

EmosSwit = b1.*T+b2; % Joules
EdiodeSwit = e1.*T+e2; % Joules

PmosSwit = fsw*EmosSwit/2 * ImosScale*Vscale;
PdiodeSwit = fsw*EdiodeSwit/2 * IdiodeScale*Vscale;

% MOSFET TOTAL LOSSES
Pmos = PmosCond + PmosSwit;

% DIODE TOTAL LOSSES
Pdiode = PdiodeCond + PdiodeV + PdiodeSwit;
```

```
Pmt = Pmos';
Pmc = PmosCond';
Pms = PmosSwit';
Pdt = Pdiode';
Pdc = PdiodeCond' + PdiodeV';
Pds = PdiodeSwit';
% end code
```

Geometry_calculations.m

```matlab
% This MATLAB code is used to make decisions regarding geometry calcs.
% The numbers are subject to periodic change and the final numbers shown
% are not necessarily the final numbers used in last rev. of the device.

% geometry calculations

clc; clear all;
%close all;

ID_initial = 3.0;

Re1 = 0.038;
Re2 = 0.038:0.003:(.038 + 5*0.003);

DeltaExitRadius = Re2-Re1;
DeltaExitDiameter = DeltaExitRadius*2; % meters
DeltaExitDiameterE = DeltaExitDiameter*39.3700787; % inches
ExitDiameter = ID_initial + DeltaExitDiameterE; % inches

Ve1 = 76;
Ve2 = Ve1.*(Re1./Re2).^2;
Ve2E = Ve2*0.0568181818; % mph

dP1 = 15; % inches of H2O
dP2 = dP1*(Ve2./Ve1).^2;

id = 3:0.001:ExitDiameter(end); % inches
od = 9.9; % inches
h1 = 2.5;

% Calculate original volume for a point of comparison
V1 = pi/4 * (od^2 - id(1)^2) * h1;

h = zeros(1,length(id));
h = V1./(pi/4.*(od^2-id.^2));

FS = 11; % font size

figure(1)
% subplot(3,1,1)
% plot(ExitDiameter,Ve2E);
% grid on;
% xlabel('Inner Diameter, d (inches)')
% ylabel('V_{exit} (mph)')

subplot(2,1,1)
plot(ExitDiameter,dP2);
grid on;
xlabel('Inner Diameter, d (inches)',...
```

```matlab
    'FontWeight','bold','FontSize',FS)
ylabel('\DeltaP (in. H_2O)',...
    'FontWeight','bold','FontSize',FS)


subplot(2,1,2)
plot(id,h); grid on;
xlabel('Inner Diameter, d (inches)',...
    'FontWeight','bold','FontSize',FS)
ylabel('Height of Capacitor, H (inches)',...
    'FontWeight','bold','FontSize',FS)
title('Volume and OD are held constant',...
    'FontWeight','bold','FontSize',FS)
```

FinDeltaP.m

This MATLAB code is used to analyze the pressure drop through inerter fins.

```matlab
% AXIAL INFLOW AIR-COOLED INVERTER
% AIR FLOW CHARACTERISTICS OVER COOLING FINS
% JON TAWFIK, JUNE 18, 2010

clear; close all; clc;

set(0,'DefaultTextFontsize',10,...
    'DefaultTextFontname','Cambria',...
    'DefaultAxesFontname','Cambria');

figure(1);
moody3; hold on;
        % fill the entire screen with the moody diagram
        hFig = figure(1);
        if nargin < 1
            hFig = gcf;
        end
        drawnow % Required to avoid Java errors
        jFig = get(handle(hFig), 'JavaFrame');
        jFig.setMaximized(true);

Ainverter = 0.0048; %m^2

% MATERIAL PROPERTIES
eps = 0.002e-3; %m surface roughness of aluminum
epsE = 6.7e-6; %ft surface roughness of aluminum (english)

% AIR PROPERTIES AT 350K
rho = 0.9950; % kg/m^3 density
mu = 208.2e-7; % N*s/m^2  dynamic viscosity
nu = mu/rho; % m^2/s   kinematic viscosity
g = 9.81; %m/s^2, gravity

% PARAMETRIC STUDY WITH RESPECT TO INLET VELOCITY
Vstart = 2; % meters per second
Vend = 35; % meters per second
ZeroStart = zeros(1,length(Vstart:1:Vend));

geo = linspace(0.0015,0.005,5); %m, distance between fins
%x1 = 0.01066; %m, fin height
%x2 = 0.00209; %m, fin tip to partition (approximate)
%y2 = 0.0025; %m, fin pitch
%y1 = 0.0015

for y1 = geo
    % GEOMETRIC PARAMETERS
    x1 = 0.01066; %m, fin height
```

```
x2 = 0.00209; %m, fin tip to partition (approximate)
y2 = 0.0025; %m, fin pitch
%y1 = 0.0015
Lfin = 0.025; %m, fin length
Nfins = 30*2; % number of fins


Ain = (x1+x2)*y2; %m^2, Inlet area
Ach = x1*y1 + x2*y2; % m^2; channel area
Per = 2*x1 + 2*y2; % wetted perimeter
Dhydr = 4*Ach/Per; %m, hydraulic diameter, White (6.59), page 376
r = eps/Dhydr; % relative roughness factor

% initialize calculation with zeros everywhere
n = 0; Vch = ZeroStart; ReD = ZeroStart;
m1 = ZeroStart; f1 = ZeroStart; hf1 = ZeroStart; deltaP1 = ZeroStart;
m2 = ZeroStart; f2 = ZeroStart; hf2 = ZeroStart; deltaP2 = ZeroStart;

for Vin = Vstart:1:Vend

    n = n + 1;

    Vch(n) = Vin*(Ain/Ach); % m/s, channel velocity
    ReD(n) = Vch(n)*Dhydr/nu; % Reynolds number based on diameter

    % calculate friction factor based on White eq. 6.48, page 366
    err = 0.1; fold = 0.04; % initialize while loop
    while err > 0.00000001
        m1(n) = m1(n) + 1;
        f1(n) = (-2*log10(r/3.7+2.51/ReD(n)*sqrt(fold)))^(-2);
        err = abs(f1(n) - fold);
        fold = f1(n);
    end

    hf1(n) = f1(n)*Lfin*Vch(n)^2/(2*g*Dhydr); % m, White (6.58) p.376
    deltaP1(n) = rho*g*hf1(n)*0.00401463078662; % dP in.H2O

    % calculate friction factor based on White eq. 6.68, page 378
    clear err fold
    err = 0.1; fold = 0.04; % initialize while loop
    while err > 0.00000001
        m2(n) = m2(n) + 1;
        f2(n) = (2*log10(0.64*ReD(n)*sqrt(fold))-0.8)^(-2);
        err = abs(f2(n) - fold);
        fold = f2(n);
    end

    hf2(n) = f2(n)*Lfin*Vch(n)^2/(2*g*Dhydr); % m, White (6.58) p.376
    deltaP2(n) = rho*g*hf2(n)*0.00401463078662; % dP in.H2O

end; Vin = Vstart:1:Vend;

% PLOT THE RESULTS ON A MOODY DIAGRAM
```

```matlab
    h1 = semilogx(ReD,f1,'g','LineWidth',5);
    h2 = semilogx(ReD,f2,'r','LineWidth',5);
end

legend([h1,h2],'White (6.48)','White (6.68)','Location','SouthWest')


titleFig2 = {['Pressure Loss Due to Fin Roughness'];...
    ['N = ',num2str(Nfins),' total fins']};

Q = Vin*Ainverter*2118.88; % cfm

% PLOT THE PRESSURE DROP RESULTS
figure(2);
%plot(Q,deltaP1.*Nfins,'b','LineWidth',2);
plot(Q,deltaP2*Nfins,'r','LineWidth',2);
xlim([Q(1) 100]);
title(titleFig2,'fontweight','Bold')
xlabel('Inlet Air Flow Rate, cfm')
ylabel('\DeltaP, inches H_2O')
%legend('White (6.48)','White (6.68)','Location','NorthWest')
```

moody3.m

```matlab
function moody3(units,paper,name)
% Moody Diagram (R13)
%   MOODY(UNITS,PAPER,NAME) generates a four axis, publication quality
%   Moody diagram as a PAPER size encapsulated postscript file NAME with
%   UNITS.  Default units are IMPERIAL.  If units are SI, the default
%   paper size is A4.  If units are IMPERIAL, the default paper size is
%   LETTER.  The default file name is MOODY.EPS.
% Examples:
%   MOODY % writes letter size moody.eps with imperial units
%   MOODY SI % writes A4 size moody.eps with SI units
%   MOODY IMPERIAL A4 % writes A4 size moody.eps with imperial units
%   MOODY SI LETTER % writes letter size moody.eps with SI units
%   MOODY SI A4 MOODY.SI.EPS % writes A4 size moody.si.eps with SI units

% Copyright(c)2004-2008
% Tom Davis (tdavis@metzgerwillard.com)
% Last revision: 03/10/2008
% Modified and renamed by Jon Tawfik on July 1, 2010
% Last revision: December 2, 2010

r=[0,1e-6,5e-6,1e-5,2e-5,5e-5,1e-4,2e-4:2e-4:1e-3,...
  1.5e-3,2e-3,3e-3,4e-3:2e-3:1e-2,1.25e-2,1.5e-2,1.75e-2,...
  2e-2:0.5e-2:4.5e-2,5e-2,6e-2,7e-2]; % Relative roughness
R=logspace(3,8,100);                  % Reynolds number
L=[600,2300];                         % Laminar flow
T=[2300,R(R>2300)];                   % Turbulent flow
start=[2.3e2,5.5e6,1.5e6,4.5e5,2.6e5,9e4,4.5e4,2e4,...
  7e3,1.5e4,1.2e4,2.3e2,7e3,2.3e2*ones(1,18)];

figure(1), clf, cf=gcf; ca=gca;
set(cf,'PaperOrientation','landscape',...
  'name','MoodyDiagram','PaperUnits','points');
set(ca,'xscale','log','yscale','log','box','on',...
  'fontsize',12,'DefaultTextFontSize',12);
axis([600,1e8,0.008,0.1]); pbaspect([13.5,9.5,1]); hold on

% Units and paper size
u='imp'; p='Letter';
if nargin
  if strcmpi(units,'si')
    u='si'; p='A4';
  end
  if nargin>1
    if strcmpi(paper,'a4')
      p='A4';
    else
      p='Letter';
    end
  end
end
```

113

```matlab
units=u; paper=p; white=[1 1 1];

% Critical zone patch
patch([2e3,2e3,4e3,4e3],[8e-3,1e-1,1e-1,8e-3],0.96*white)

% Friction factor curves
loglog(L,64./L,'b','linewidth',1)
for i=1:length(r)
  loglog(T(T>=start(i)),colebrook(T(T>=start(i)),r(i)),...
    'b','linewidth',1)
  if r(i)>5e-6
    text(1.1e8,colebrook(1e8,r(i)),num2str(r(i)),'fontsize',10)
  end
end

% Zone labels
set(ca,'DefaultTextVerticalAlignment','top');
loglog(T,(1.14-2*log10(3500./T)).^(-2),'linewidth',0.1,'color','k')
text(1.08e3,0.096,{'Laminar','flow'},...
  'HorizontalAlignment','center','BackgroundColor',white)
text(2.83e3,0.096,{'Critical','zone'},...
  'HorizontalAlignment','center','BackgroundColor',0.96*white)
text(1.3e4,0.096,'Transition zone',...
  'HorizontalAlignment','center','BackgroundColor',white)
text(1.4e6,0.096,['Complete turbulence, rough pipes, {\itR}  ',...
  '> 3500/{\itr},  1/\surd{\itf}  = 1.14 - 2 log {\itr}'],...
  'HorizontalAlignment','center','BackgroundColor',white)
set(ca,'DefaultTextVerticalAlignment','middle',...
  'DefaultTextFontSize',10);
text(2.0e3,9.4e-2,'\rightarrow','HorizontalAlignment','right')
text(4.08e4,9.4e-2,'\rightarrow','HorizontalAlignment','right')
text(4.0e3,9.4e-2,'\leftarrow')
text(4.08e4,9.4e-2,'\leftarrow')

% VD water
VD1=[0.1,0.2:0.2:1,2:2:10,20:20:100,200:200:1000,2000:2000:10000];
ul=char(95*ones(1,94));

% VD air
VD2=[2:2:10,20:20:100,200:200:1000,2000:2000:10000,20000:20000:100000];

if strcmp(units,'si') % SI units
  Runits='({\itV} in m/s, {\itD} in m, \nu in m^{\fontsize{6} 2}/s)';
  runits='(\epsilon in mm, {\itD} in mm)';
  x=1.8e5; y=0.02912; viscosity='\nu (m^2/s) ';
  VD1=[0.06,0.08,VD1]; VD2=[1,VD2]; ul=[ul];
  nuWater=1.003e-6; nuAir=1.511E-5; mult=100; temp='20\circC';
  pressure='(101.325 kPa)'; sep2='{\fontname{MS LineDraw}ÄÄÄÄÄÄÄÄ}';
  vdunits='({\itV} in m/s, {\itD} in cm)';
  epsilon={'\epsilon (mm)',sep2,'0.9-9','0.3-3',...
    '0.18-0.9','0.25','0.15','0.12','0.046','0.0015'};
  acceleration={'{\itg} (m/s^2)',sep2,'9.78033','9.80665','9.83219'};
else                  % Imperial units
```

114

```matlab
  Runits='({\itV} in fps, {\itD} in ft, \nu in ft^{\fontsize{6} 2}/s)';
  runits='(\epsilon in ft, {\itD} in ft)';
  x=1.95e5; y=0.031; viscosity='\nu (ft^2/s) ';
  nuWater=1.217e-5; nuAir=1.583e-4; mult=12; temp='60\circF';
  pressure='(14.70 psia)'; sep2='{\fontname{MS LineDraw}ÄÄÄÄÄÄÄÄÄ}';
  vdunits='({\itV} in fps, {\itD} in inches)';
  epsilon={'\epsilon (ft)',sep2,'0.003-0.03','0.001-0.01',...
    '0.0006-0.003','0.00085','0.0005','0.0004','0.00015','0.000005'};
  acceleration={'{\itg} (ft/s^2)',sep2,'32.0877','32.1740','32.2578'};
end

xlabel(['Reynolds number  {\itR} = {\itVD}/\nu'],'fontsize',10)
ylabel(['Darcy-Weisbach friction factor  {\itf} = '],'fontsize',10)
text(360,0.0413,{'2{\ithDg}','{\fontsize{3}  }',...
  '{ \itLV}^{\fontsize{6}  2}'},'rotation',90)
text(1.9e8,0.028,['Relative roughness  {\itr} = \epsilon/{\itD}'],...
  'rotation',90,'HorizontalAlignment','center')

index=find(T>=start(3)); T1=T(index(1));
f1=colebrook(T1,5e-6);
plot([1e6,T1],[f1,f1],'k')
index=find(T>=start(2)); T2=T(index(1));
f2=colebrook(T2,1e-6);
plot([4e6,T2],[f2,f2],'k')
set(ca,'DefaultTextFontSize',8);
text(1e6,f1,'{\itr}  = 5e-006',...
  'HorizontalAlignment','right','BackgroundColor',white)
text(4e6,f2,'{\itr}  = 1e-006',...
  'HorizontalAlignment','right','BackgroundColor',white)
f3=colebrook(2e5,0);
plot([1.18e5,2e5],[f3,f3],'k'), hold off
text(2.55e4,1.65e-2,{'Smooth pipes, {\itr}  = 0',...
  '1/\surd{\itf}  = 2 log({\itR} \surd{\itf} ) - 0.8',' '},...
  'VerticalAlignment','top','BackgroundColor',white)

% Surd overbars
set(ca,'DefaultTextVerticalAlignment','bottom');

% VD water axis
text(2.41e5,0.126,['{\itVD} for water at ',temp,' ',vdunits],...
  'HorizontalAlignment','center','VerticalAlignment','middle')
for i=1:length(VD1)
  R=VD1(i)/(mult*nuWater);
  if VD1(i)~=80*[0.001,1,10,100]
    text(R,0.120,num2str(VD1(i)),'fontsize',8,...
      'HorizontalAlignment','center','VerticalAlignment','middle')
  end
  text(R,0.114,'|','fontsize',8,'HorizontalAlignment','center')
end
text(VD1(1)/(mult*nuWater),0.11379,ul,'interpreter','none','fontsize',8)
text(VD1(end)/(mult*nuWater),0.11379,ul,'fontsize',8,'interpreter',...
  'none','HorizontalAlignment','right')
```

```matlab
% VD air axis
text(2.41e5,0.110,['{\itVD} for atmospheric air at ',temp],...
  'HorizontalAlignment','center','VerticalAlignment','middle')
for i=1:length(VD2)
  R=VD2(i)/(nuAir*mult);
  if VD2(i)~=80*[1,10,100,1000]
    text(R,0.105,num2str(VD2(i)),'fontsize',6,...
      'HorizontalAlignment','center','VerticalAlignment','middle')
  end
  text(R,0.1,'|','fontsize',6,'HorizontalAlignment','center')
end

% Write eps
if strcmp(paper,'A4') % A4 letter paper size
  set(cf,'PaperSize',[842 595],'PaperPosition',[-20 -52 842 644]);
else                  % US letter paper size
  set(cf,'PaperSize',[792 612],'PaperPosition',[-45 -43 842 644]);
end
print -depsc -r720 MoodyDiagram

% Insert orientation and size comments
fin =fopen('MoodyDiagram.eps','rt');
if nargin<3, name='moody.eps'; end
fout=fopen(name,'wt');
line=fgets(fin);
while ~strncmp(line,'%%EndComments',13)
  fprintf(fout,'%s',line);
  line=fgets(fin);
end
fprintf(fout,'%s\n%s%s\n%s','%%Orientation: Landscape',...
  '%%DocumentPaperSizes: ',paper,line);
while ~feof(fin)
  line=fgets(fin);
  fprintf(fout,'%s',line);
end
fclose all;
delete MoodyDiagram.eps
%-------------------------------------------------------------------
function f=colebrook(R,r)
% Colebrook Equation
%   f = Darcy-Weisbach friction factor
%   R = Reynolds number
%   r = relative roughness

f=zeros(size(R)); f0=0.04;
for i=1:length(R)
  for j=1:5
    f0=(2*log10(r/3.7+2.51/R(i)/sqrt(f0)))^-2;
  end
  f(i)=f0;
end
```

Vita

Jonathan Atef Tawfik was born to Atef & Soheir Tawfik of Cairo, Egypt in 1984. He was raised in Rockford, IL where he graduated from Rockford Lutheran High School. Jon went on his own in 2002 and moved to West Lafayette, IN where he attended Purdue University and obtained his Bachelor of Science degree in Mechanical Engineering in 2007. Upon graduation, he moved to Houston, Texas where he worked in the petrochemical industry for two years. Jon returned to the academic environment in 2009 and completed the requirements to graduate with a Master of Science in Mechanical Engineering from the University of Tennessee, Knoxville in December, 2010. In the following year, Jon will move on once more to Boston, MA to work for General Electric Aviation in Lynn, MA, but more importantly to see about a girl. He is currently planning to be united in marriage to Monica Ibrahim of Walpole, MA in late summer, 2011.